

TUM School of Engineering and Design

# About Computational Fluid Dynamics and the Simulation of Pure Substance Condensation on Horizontal Tubes

Thomas Kleiner

Vollständiger Abdruck der von der TUM School of Engineering and Design der Technischen Universität München zur Erlangung eines  
Doktors der Ingenieurwissenschaften  
genehmigten Dissertation.

Vorsitzende: Prof. Dr. rer. nat. Sonja Berensmeier

Prüfer der Dissertation:

1. Prof. Dr.-Ing. Harald Klein
2. Prof. Dr.-Ing. Kai-Olaf Martin Hinrichsen

Die Dissertation wurde am 27.08.2021 bei der Technischen Universität München eingereicht und durch die TUM School of Engineering and Design am 07.02.2022 angenommen.



*“God made the bulk;  
the surface was invented by the devil“*

-Wolfgang Pauli-



# Acknowledgements

This dissertation was developed during my time at the Institute of Plant and Process Technology of the Technical University of Munich. During this time, as in every memorable journey, I was able to count on the support of people around me.

I thank Prof. Dr.-Ing. Harald Klein for allowing me to join his team and becoming a part of the APT family! Giving me the opportunity to find my own path through the dissertation topic without any previous CFD experience shows how much trust you have placed in me right from the beginning. For me, this trust was the strongest motivation you could give me for trying to excel in my topic. I am happy that I was able to make this given opportunity count and hope that you see the effort that was put in this work as a way of me saying thank you for these amazing six years.

Further, I express my deepest gratitude to Dr.-Ing. Sebastian Rehfeldt for being my mentor throughout this journey. I could always count on a dry remark and your help, whenever I needed to hear either of it. By keeping the atmosphere at the department light, while thriving for excellence in your work, you set a great example and filled my journey with a lot of memorable moments.

Special thanks go to Prof. Dr. Sonja Berensmeier for taking the chairmanship of my examination and to Prof. Dr.-Ing. Kai-Olaf Hinrichsen for taking the time to be my second examiner.

A lot of heart-felt thank yous belong to my colleagues at the department. Help was always easily found, when needed. Additionally, knowing that everyone is going through similar struggles was half the battle as it helped ground one's own expectations. The additional escapes from current problems at hand during coffee breaks or evening gatherings are the moments that will be remembered most from this time. I am also thankful to everyone who joined me during this time by enduring me as their supervisor. I enjoyed supporting you during your studies and I am looking forward to our next encounter!

I thank my parents on whose support I could always count on before, during and surely after this time and my two brothers, to whom I can always turn to, if ever needed.

To my wife Julia: thank you not just for supporting me at all times, but also for being the reason, I want to make an effort each day.

Last but not least, I want to thank my son Christoph, for making me realize that it is time to close this chapter and focus more on him and his future siblings.



Parts of the submitted dissertation have been published in the following articles:

Kleiner, T.; Rehfeldt, S.; Klein, H.: *CFD model and simulation of pure substance condensation on horizontal tubes using the volume of fluid method*. International Journal of Heat and Mass Transfer 138 (2019) 420-431. DOI: [10.1016/j.ijheatmasstransfer.2019.04.054](https://doi.org/10.1016/j.ijheatmasstransfer.2019.04.054).

Kleiner, T.; Eder, A.; Rehfeldt, S.; Klein, H.: *Detailed CFD simulations of pure substance condensation on horizontal annular low finned tubes including a parameter study of the fin slope*. International Journal of Heat and Mass Transfer 163 (2020) 120363. DOI: [10.1016/j.ijheatmasstransfer.2020.120363](https://doi.org/10.1016/j.ijheatmasstransfer.2020.120363).



# Abstract

In response to the anthropogenic climate change, the European Union signed the Green Deal in 2019, in which they agree to reduce greenhouse gas emissions below 55% of the emission level of 1990 by 2030 and aim to reach emission net neutrality by 2050. In order to achieve these objectives, the energy-intensive chemical industry, among others, has to become more eco-friendly. One possible approach is to increase the efficiency of shell-and-tube heat exchangers by utilizing innovative surface-structured tubes for condensation processes. Possible surface structures are annular low fins or pin-fins with dimensions of about 1 mm and below. According to REIF 2016, these tubes have significantly higher outer heat transfer coefficients during condensation of hydrocarbons compared to smooth tubes.

While condensation on smooth tubes is already well described by Nusselt's film theory, there is no universally applicable model for describing condensation on surface-structured tubes due to the increased complexity. Within the work of this dissertation, a simulation approach using computational fluid dynamics (CFD) was developed, which allows for detailed simulations of condensation on surface-structured tubes. A new method was developed and implemented in OpenFOAM.

The developed CFD algorithm divides the simulation domain into static regions of fluid and solid phases, which are in thermal contact with each other. Condensation is simulated using the Volume-of-Fluid method in the fluid regions. This allows for transient simulations of heat transfer and fluid dynamics during condensation on horizontal tubes.

The simulation accuracy of the developed algorithm was validated with the Stefan problem for *n*-pentane and water and by simulating condensation of *n*-pentane on the outside of a horizontal smooth tube. A physically plausible fluid dynamic behavior of the two-phase flow was obtained in the simulations. For the Stefan problem, the condensate film thicknesses determined via simulations stand in excellent agreement with the analytical solution for both fluids. The condensate film thicknesses in the simulations of smooth tubes coaligns with Nusselt's film theory. The heat transfer coefficients determined from the simulations lie within the accuracy of Nusselt's film theory and agree very well with measurements of REIF 2016.

The simulation quality was further investigated on horizontal surface-structured tubes. For this purpose, condensation on a horizontal low-finned GEWA-K30 tube from Wieland was simulated. The simulated heat transfer coefficients also agree very well with the measurements of REIF 2016. The applicability of the CFD algorithm for parameter studies was additionally examined. The fin slope was focused in the parameter study and both the flooding behavior of the condensate and heat transfer were regarded.

The flooding behavior was validated based on the flooding angle using the model of HONDA ET AL. 1983. The results of the highly resolved simulations provide detailed insight into the condensation process on low finned tubes. A maximum heat transfer coefficient is obtained at a moderate incline of the fin. Due to the high resolution of the condensate film in the simulations, it was possible to attribute the optimized heat transfer coefficient to an ideal condensate flow inside the fin spacing.

# Kurzfassung

Als Reaktion auf den anthropogenen Klimawandel hat die Europäische Union 2019 den europäischen Grünen Deal unterzeichnet. Dieser sieht eine Reduzierung der Treibhausgasemission bis 2030 auf unter 55 % des Wertes von 1990 vor und Emissionsneutralität bis 2050. Zum Erreichen dieser Ziele muss unter anderem die energieintensive chemische Industrie klimafreundlicher werden. Ein möglicher Ansatz dafür ist die Effizienzsteigerung von Rohrbündelwärmeübertragern durch Verwendung von innovativen, oberflächenstrukturierten Rohren bei der Kondensation. Mögliche Oberflächenstrukturen bei der Kondensation an horizontalen Rohren sind zum Beispiel niedrige Rippen oder Nadeln. Diese Rohre haben nach REIF 2016 einen deutlich höheren äußeren Wärmeübergangskoeffizienten bei der Kondensation von Kohlenwasserstoffen im Vergleich zu Glattrohren.

Während die Kondensation an Glattrohren bereits ausreichend genau durch die Nußelt'sche Wasserhauttheorie beschrieben wird, gibt es aufgrund der erhöhten Komplexität kein universell einsetzbares Modell zur Beschreibung der Kondensation an oberflächenstrukturierten Rohren. Im Rahmen dieses Promotionsvorhabens wurde hierfür ein Simulationsansatz mittels numerischer Strömungsmechanik (engl.: Computational Fluid Dynamics – CFD) entwickelt, welcher die Kondensation an oberflächenstrukturierten Rohren detailliert berechnet. Dafür wurde zunächst eine Methode zur Beschreibung der Kondensation entwickelt und in OpenFOAM implementiert.

Dieser entwickelte CFD-Algorithmus teilt die Simulationsdomäne in statische Regionen fluider und fester Phasen ein, welche in thermischem Kontakt stehen. Die Kondensation wird unter Verwendung der Volume-of-Fluid-Methode in den fluiden Regionen simuliert. Dies ermöglicht es, den Wärmedurchgang und die Fluidodynamik bei der Kondensation an horizontalen Rohren transient zu simulieren.

Die Simulationengenauigkeit des entwickelten Algorithmus wurde mit Hilfe des Stefan-Problems für die Stoffsysteme *n*-Pentan und Wasser sowie der Kondensation von *n*-Pentan an einem horizontalen Glattrohr validiert. Bei den Simulationen ergibt sich ein physikalisch sinnvolles fluiddynamisches Verhalten der Zweiphasenströmung. Beim Stefan-Problem stimmen bei beiden Stoffsystemen die über die Simulation ermittelten Kondensatfilmdicken exakt mit der analytischen Lösung überein. Bei den Simulationen am Glattrohr stimmen die Kondensatfilmdicken sehr gut mit der Nußelt'schen Wasserhauttheorie überein. Die durch die Simulation ermittelten Wärmeübergangskoeffizienten liegen innerhalb der Genauigkeitsgrenzen der Nußelt'schen Wasserhauttheorie und stimmen sehr gut mit den Messergebnissen von REIF 2016 überein.

Weiterführend wurde die Simulationsgenauigkeit an horizontalen oberflächenstrukturierten Rohren untersucht. Hierfür wurde die Kondensation an einem horizontalen niedrig berippten GEWA-K30 Rohr von Wieland simuliert. Die simulierten Wärmeübergangskoeffizienten stimmen ebenfalls sehr gut mit den Messungen von REIF 2016 überein. Zusätzlich wurde überprüft, wie gut sich der CFD-Algorithmus für eine Parameterstudie eignet. Bei der Parameterstudie wurde die Rippensteigung verändert und sowohl das Flutverhalten des Kondensates sowie der Wärmeübergang betrachtet. Das Flutverhalten wurde anhand des Flutungswinkels mit Hilfe des Modells von HONDA ET AL. 1983 validiert. Die Ergebnisse der hochaufgelösten Simulationen bieten einen tiefen Einblick in den Kondensationsvorgang an niedrig berippten Rohren. Aus der Parameterstudie ergibt sich ein maximaler Wärmeübergangskoeffizient bei mittlerer Rippensteigung. Durch die hohe Auflösung des gebildeten Kondensatfilms in den Simulationen konnte die Maximierung des Wärmeübergangskoeffizienten auf ein optimiertes Kondensatabfließverhalten im Rippental zurückgeführt werden.

# Contents

<b>Nomenclature</b>	<b>XIII</b>
<b>1 Introduction</b>	<b>1</b>
<b>2 Heat Transfer During Condensation</b>	<b>4</b>
2.1 Heat transfer across a tube . . . . .	5
2.1.1 Heat transfer resistance . . . . .	7
2.1.2 Overall heat transfer resistance . . . . .	8
2.2 Heat transfer during condensation on a horizontal smooth tube . . . . .	9
2.2.1 Condensate flow . . . . .	11
2.2.2 Calculation of the outer heat transfer coefficient . . . . .	16
2.3 Surface-structured tubes . . . . .	18
2.3.1 Condensate flow . . . . .	20
2.3.2 Heat transfer models . . . . .	21
<b>3 Computational Fluid Dynamics</b>	<b>25</b>
3.1 Discretization . . . . .	28
3.1.1 Temporal Discretization . . . . .	29
3.1.2 Volume Discretization . . . . .	29
3.1.3 Boundary control volumes . . . . .	35
3.1.4 Temporal progression . . . . .	36
3.1.5 Solution method . . . . .	37
3.2 Two-phase flow . . . . .	43
3.2.1 Modeling approaches . . . . .	43
3.2.2 Volume-of-Fluid method . . . . .	45
3.3 Phase change in the Volume-of-Fluid method . . . . .	56
3.3.1 Heat flux balance . . . . .	57
3.3.2 Schrage model . . . . .	58
3.3.3 Numerical iteration techniques . . . . .	59
<b>4 Simulation Validation</b>	<b>62</b>
4.1 Introduction . . . . .	63
4.2 Mathematical formulation . . . . .	63
4.2.1 Governing Equations . . . . .	63
4.2.2 Phase Change Model . . . . .	65
4.3 Validation with the 1D Stefan problem . . . . .	66
4.4 Simulation of condensation on horizontal tubes . . . . .	69
4.4.1 Run-off behavior . . . . .	69

---

4.4.2	Drip-off behavior . . . . .	76
4.4.3	3D simulation . . . . .	79
4.5	Conclusion . . . . .	83
<b>5</b>	<b>Simulation of Finned Tubes</b>	<b>85</b>
5.1	Introduction . . . . .	86
5.2	Condensation of pentane on a GEWA-K30 tube . . . . .	86
5.2.1	Simulation setup . . . . .	86
5.2.2	Simulation progression and results . . . . .	88
5.3	Variation of the incline of the fin . . . . .	93
5.3.1	Geometric parameters and meshes . . . . .	93
5.3.2	Condensate film along the fin flank . . . . .	95
5.3.3	Flooding behavior . . . . .	98
5.3.4	Heat transfer . . . . .	102
5.4	Conclusion . . . . .	103
<b>6</b>	<b>Summary and Outlook</b>	<b>105</b>
	<b>List of Tables</b>	<b>109</b>
	<b>List of Figures</b>	<b>110</b>
	<b>List of Publications</b>	<b>112</b>
	<b>Bibliography</b>	<b>113</b>

# Nomenclature

## Symbols

$a$	Components of matrix $\underline{\underline{M}}$	
$A$	Area	$\text{m}^2$
$\mathcal{A}$	Diagonal components of matrix $\underline{\underline{M}}$	
$b$	Thickness of fin tip	$\text{m}$
$\mathcal{B}$	Blending function	-
$c_p$	Isobaric heat capacity	$\frac{\text{J}}{\text{kg K}}$
$C$	Constant	-
$\mathbf{D}$	Strain-rate tensor	$\frac{1}{\text{s}}$
$D$	Anti diffusive flux	
$e$	Edge length	$\text{m}$
$f$	Fin flank length	$\text{m}$
$\mathbf{f}_\sigma$	volumetric surface tension force	$\frac{\text{N}}{\text{m}^3}$
$\mathbf{F}$	Force	$\text{N}$
$\mathcal{F}$	Flux	$\frac{\text{m}^3}{\text{s}}$
$\mathcal{F}_\rho$	Mass flux	$\frac{\text{kg}}{\text{s}}$
$\mathcal{F}_\xi$	Flux of arbitrary intensive scalar	
$g, \mathbf{g}$	Gravitational acceleration	$\frac{\text{m}}{\text{s}^2}$
$h$	Specific enthalpy	$\frac{\text{J}}{\text{kg}}$
$\mathcal{H}$	Residual for derivation of pressure equation	$\text{N}$
$\mathbf{I}$	Unit tensor	-
$\underline{\underline{I}}$	Unit Matrix	-
$k$	Overall heat transfer coefficient	$\frac{\text{W}}{\text{m}^2 \text{K}}$
$l_\phi$	Condensate level at flooding angle	$\text{m}$
$L$	Considered length of Tube	$\text{m}$
$m$	Mass	$\text{kg}$
$\dot{m}$	Mass flow rate	$\frac{\text{kg}}{\text{s}}$
$\bar{m}$	Molar mass	$\frac{\text{kg}}{\text{mol}}$
$\underline{\underline{M}}$	Solution matrix of system of linear algebraic equations	

$\mathbf{n}$	Unit normal vector	-
$O, \mathbf{O}$	Explicit residual of linear system of algebraic equations	
$\underline{O}$	Column vector of explicit residual of linear system of algebraic equations	
$\mathcal{O}$	Summarizing function for discretized transport equation	
$p$	Pressure	Pa
$p_{rgh}$	Modified pressure	Pa
$\dot{q}$	Heat flux	$\frac{\text{W}}{\text{m}^2}$
$\dot{Q}, \dot{\mathbf{Q}}$	Heat stream	W
$r$	Radius	m
$r^*$	Relative radius	m
$R$	Thermal resistance	$\frac{\text{K}}{\text{W}}$
$\Delta R$	Radial length of simulation domain	m
$\mathcal{R}$	Universal gas constant	$\frac{\text{J}}{\text{molK}}$
$s$	Fin spacing	m
$S$	Surface area	$\text{m}^2$
$\mathbf{S}_f$	Face normal vector	$\text{m}^2$
$\tilde{\mathbf{S}}_f$	Face vector of over-relaxed approach	$\text{m}^2$
$\Delta \mathbf{S}$	Vector difference	$\text{m}^2$
$\mathcal{S}$	Source term	
$\mathcal{S}_p$	Linear portion of source term	
$\mathcal{S}_q$	Volumetric latent heat release/consumption	$\frac{\text{W}}{\text{m}^3}$
$\mathcal{S}_u$	Non-linear portion of source term	
$\mathcal{S}_V$	Volumetric change in volume due to phase change	$\frac{1}{\text{s}}$
$\mathcal{S}_\tau$	Specific rate of dissipated heat release	$\frac{\text{J}}{\text{m}^3}$
$\mathcal{S}_\gamma$	Specific volumetric phase change rate	$\frac{1}{\text{s}}$
$\tilde{\mathcal{S}}_q$	Unlimited $\mathcal{S}_q$	$\frac{\text{W}}{\text{m}^3}$
$t$	Time	s
$\Delta t$	Time step size	s
$T$	Temperature	K
$\mathbf{U}$	Velocity	$\frac{\text{m}}{\text{s}}$
$\mathbf{U}_S$	Velocity of control volume	$\frac{\text{m}}{\text{s}}$
$\mathbf{U}^*$	Adjusted velocity	$\frac{\text{m}}{\text{s}}$

---

$V$	Volume	$\text{m}^3$
$w$	Step function	
$\mathbf{x}$	Position vector	$\text{m}$
$\Delta x$	Characteristic length of control volume	$\text{m}$
$y$	Fin height	$\text{m}$
$z$	Coordinate axis	$\text{m}$

**Greek symbols**

$\alpha$	Heat transfer coefficient	$\frac{\text{W}}{\text{m}^2 \text{K}}$
$\beta$	Incline angle of the fin	-
$\tau$	Stress tensor	$\text{Pa}$
$\delta$	Condensate film thickness	$\text{m}$
$\bar{\delta}$	Average condensate film thickness	$\text{m}$
$\kappa$	Bulk viscosity	$\text{Pa s}$
$\varphi$	Revolution angle	-
$\Gamma$	Latent heat of evaporation	$\frac{\text{W}}{\text{kg}}$
$\rho$	Density	$\frac{\text{kg}}{\text{m}^3}$
$\sigma, \sigma$	Surface tension	$\frac{\text{N}}{\text{m}}$
$\lambda$	Thermal conductivity	$\frac{\text{W}}{\text{mK}}$
$\lambda_\xi$	Diffusive transfer coefficient of $\xi$	
$\eta$	Dynamic viscosity	$\text{Pa s}$
$\theta$	Contact angle	-
$\chi$	Most unstable wavelength	$\text{m}$
$\Psi$	Stream function	-
$\Phi$	Flooding angle	-
$\xi$	Arbitrary intensive scalar	
$\xi$	Arbitrary intensive quantity	
$\underline{\xi}$	Column vector of arbitrary intensive scalar	
$\varepsilon$	Interpolation value	-
$\gamma$	Volumetric phase fraction	-
$\Omega$	Material properties	
$\kappa$	Weighing factor	-
$\zeta_S$	Accommodation coefficient	-
$\zeta_L$	Mass transfer intensity factor	-

**Dimensionless numbers**

$Bo$	Bond number	-
$Cn$	Condensation number	-
$Co$	Courant number	-
$Fo$	Fourier number	-
$Re_F$	Film Reynolds number	-
$Ro$	Dimensionless tube number	-

**Indices**

1, 2	Counting index
b	Fin base
bulk	Bulk phase
c	Condensate
comp	Interface compression
cw	Cooling water bulk phase
CD	Central differencing
e	Center of boundary face e
f	Center of face f
fl	Fluid bulk phase
flooded	Flooded region
f1	Center of face f1
f2	Center of face f2
i	Inner tube surface
int	Interface
$k$	Overall heat transfer
n	Boundary face position for normal vector to point P
non-flooded	Non-flooded region
N	Computation node of control volume N
N1	Computation node of control volume N1
N2	Computation node of control volume N2
Nu	Nusselt film theory
o	Outer tube surface
$p$	Pressure equation
P	Computation node of control volume P
s	Solid
sat	Saturation condition
t	Fin tip

---

$U$	Momentum equation
UD	Upwind differencing
v	Vapor
wall	Wall
$\alpha$	Convective heat transfer
$\lambda$	Conduction
$\xi$	Value for arbitrary quantity
$\tau$	Dissipation

**Superscripts**

0	Initial value
C	Corrected
Gmax	Global maximum
Gmin	Global minimum
H	High order scheme
$i$	Time step $i$
$j$	Iteration cycle $j$
L	Low order scheme
Lmax	Local maximum
Lmin	Local minimum
max	Maximum
+	Higher bound
−	Lower bound

**Abbreviations**

1D	One dimensional
2D	Two dimensional
3D	Three dimensional
CD	Central differencing
CFD	Computational fluid dynamics
CICSAM	Compressive interface capturing scheme for arbitrary meshes
CSF	Continuum Surface Force
CV	Control volume
FCT	Flux-corrected transport
HRIC	High resolution interface capturing
MULES	Multidimensional universal limiter for explicit solution

PISO	Pressure implicit with splitting of operators
PLIC	Piecewise linear interface calculation
SIMPLE	Semi-implicit method for pressure-linked equations
SLIC	Simple line interface calculation
UD	Upwind differencing
VOF	Volume-of-Fluid

# 1 Introduction

According to LENSSEN ET AL. 2019, the annual global temperature anomalies show an increasing trend since about 1980. The gradual increase is currently approaching an overall rise in temperature of 1 °C, with a local increase up to 5 °C around the north pole, according to the Goddard Institute for Space Studies's surface temperature analysis [GISTEMP TEAM 2021]. This increase is mainly attributed to an accumulation of anthropogenic greenhouse gases in the atmosphere, where the principal gas to consider is CO<sub>2</sub> [IPCC 2013]. The global temperature increase due to anthropogenic greenhouse gases is known as global warming. The effects that global warming may cause are summarized in the 2018 report of the Intergovernmental Panel on Climate Change [IPCC 2018], where the occurrence of possible environmental calamities are categorized according to the overall annual temperature increase. Based on the categorization, the IPCC 2018 report suggests to limit global warming below 1.5 °C and urges to avoid an increase of the annual global temperature anomalies above 2.0 °C. In 2019, the European Union passed the Green Deal [EUROPEAN COMMISSION 2020], in which they aim to reduce their greenhouse gas emission level below 55 % by 2030, compared to the emission level of 1990. They further aim to achieve climate net neutrality by 2050.

In order to achieve climate net neutrality, different approaches for carbon capturing are pursued. Nonetheless, it will not be avoidable to reduce greenhouse gas emission [BÜCHNER 2016]. The European Union set a targeted share of renewable energy to 32 % for 2030. The assessment of Member States' National Energy and Climate Plans even shows that this target may be surpassed by 1.7 % [EUROPEAN COMMISSION 2020]. The expansion of the renewable energy system nonetheless, is only one aspect for reaching the targeted share. According to BÜCHNER 2016, the other aspect is to reduce the overall energy consumption without jeopardizing global competitiveness. Thus, energy efficiency in industry must be increased. The chemical industry is a key industry for this aspect, as the operations require large energy consumption and therefore offer a large energy-saving potential. Hence, chemical industry has to increase efficiency in order to keep up with rising environmental regulations, which requires reducing the overall carbon footprint of chemical plants.

Chemical plants are comprised of individual unit operations, which are combined for an overall process. The reduction of the overall carbon footprint can be achieved by either increasing the efficiency of the unit operations or by increasing the efficiency of their combination. The efficiency of the unit operations and the overall plant are depending on the conditions of the inlet streams, which means that these streams need to be tempered correctly. This is mostly done by the use of heat exchangers. Hence, many

heat exchangers are utilized in chemical plants. Optimizing their efficiency would lead to two possible CO<sub>2</sub> saving strategies. On the one hand, smaller heat exchangers could be used with the same energy transfer rate, saving material and construction costs, as well as reducing the carbon footprint. On the other hand, the increased efficiency could be used for increased heat integration of a process. This could be realized, since a more efficient heat exchanger requires a lower driving temperature difference for the same heat transfer rate. Therefore, streams with lower temperature potential could be included in the heat integration concept of a chemical plant and thereby decrease the energy consumption of the entire plant, which translates into a lower carbon footprint during plant operation.

Heat transfer during condensation or boiling can be much larger compared to single-phase heat transfer, which is why the use of condensers or boilers is often preferred in energy intensive processes. A common form of these condensers are tube bundle condensers, where condensation forms a thin liquid film either inside vertical tubes [RATTNER & GARIMELLA 2014] or outside horizontal tubes [REIF 2016]. Due to the thin liquid film, heat is transferred with high efficiency. According to KLEIN & BÜCHNER 2018, an innovative approach for horizontal tube bundle condensers with increased efficiency is the use of surface-structured tubes, as compared to smooth tubes. Possible surface structures are annular fins [HONDA ET AL. 1991] or pin-fins [ALI 2017], with fin dimensions of about 1 mm and below.

According to REIF ET AL. 2015, single-phase heat transfer models for fins are not applicable to describe the efficiency increase of these tubes during condensation, since the small dimensions cause capillary forces which impact the condensate flow. The tubes are already applied in refrigerant cycles and multiple examinations about their increased efficiency have been carried out for refrigerants [KUMAR ET AL. 1998, BRIGGS & ROSE 1995, HONDA ET AL. 1987]. REIF 2016 investigated whether these tubes are also significantly more efficient during condensation of petrochemicals, as compared to smooth tubes. An efficiency increase of condensers in petrochemical processes would provide a significant contribution to decreasing the overall energy consumption. Despite the potential, chemical plant operators are still reluctant in utilizing such tubes, as there is limited data available for relevant substances. As presented by REIF 2016, models developed for condensation of refrigerants show significant deviations from her measurements.

Film condensation on horizontal smooth tubes is well described by NUSSELT 1916a in his film theory. However, due to the increased complexity caused by the surface structure, no universal model is available so far to describe condensation on surface-structured tubes [KLEINER ET AL. 2020]. This is where computational fluid dynamics (CFD) may become the method of choice, despite KHARANGATE & MUDAWAR 2017 concluding that two-phase simulations with phase change are still limited to simple configurations. CFD is a promising approach for a universal method to predicting heat transfer coefficients during phase change, since the influence of the material properties and geometric parameters does not have to be modeled as they are input variables for the simulation. GEBAUER ET AL. 2013 first used the software Fluent for CFD simulations

---

of condensation on annular low-finned tubes. Despite getting acceptable results, the phase change model used by GEBAUER ET AL. 2013 does not fully address unresolved issues concerning phase change simulations. Their phase change model is therefore hardly considered in literature. Another investigation on condensation on annular low-finned tubes using Fluent was carried out by JI ET AL. 2019. Their condensation model uses an empirical parameter, to calibrate the simulations, using experimental results. Additionally, they use a low spacial resolution and model the condensate flow and heat transfer within the fin structure. Thus, detailed information of the condensation behavior is not accessible. Since the condensate film has a major impact on heat transfer, detailed information about the condensate film, however, is necessary for understanding the condensation process on surface-structured tubes. Both initial approaches to simulate condensation on surface-structured tubes are not evolved to the point that accurate results are assured during predictive use.

The aim of this work is to use CFD for a full description of the condensation process of pure substances on horizontal low-finned tubes. A full description means that the CFD method should unveil the two-phase flow and the temperature distribution during the condensation process. In order to do so, a rigorous CFD method needs to be developed, which uses a phase change model that is independent of heuristic or empirical parameters. Highly resolved CFD simulations on low-finned tubes are then needed, in order to resolve the two phase flow and temperature distribution. This is additionally challenging, since a thin liquid film is expected with comparatively large phase change rates at the interface, which may lead to numerical instabilities.

In this work, a phase change model for interface resolving CFD simulations of pure substances which was implemented in the open-source software OpenFOAM [OPEN-FOAM 2021] is presented. The multi-region framework provided by OpenFOAM was used, which allows for simulations of conjugate heat transfer between solid and fluid regions within the simulation domain. The validation of the implemented algorithm is presented in chapter 4. The accuracy of the algorithm is checked for the Stefan problem and condensation on a horizontal smooth tube [KLEINER ET AL. 2019]. The Stefan problem is a 1D consideration of condensate forming above a subcooled wall with a stationary vapor phase. Condensation on a horizontal smooth tube is considered as a 2D and a 3D system. The simulation results of condensation on a horizontal smooth tube are compared to Nusselt's film theory [NUSSELT 1916a] and measurements of REIF 2016.

Detailed investigations of condensation on low-finned tubes are presented in chapter 5. Condensation at the outside of a GEWA-K30 tube is simulated and compared to measurements of REIF 2016, in order to validate the simulation setup for low-finned tubes. In addition, a parameter study with the incline of the fin as the design parameter was performed, in order to evaluate the effectiveness of the predictive use of CFD for systematic studies on condensation at the outside of surface-structured tubes [KLEINER ET AL. 2020].

## 2 Heat Transfer During Condensation

According to BAER & STEPHAN 2011, heat is defined as the energy that crosses the boundary of a system. When a temperature difference between the system and its surroundings is present, heat is transported via the mechanisms conduction, convection and radiation.

For specification of the transferred heat rate, a heat flux  $\dot{q}$  is often used, which relates the transferred heat stream  $\dot{Q}$  to the area  $A$ , where the heat stream is passing through.

$$\dot{q} = \frac{\dot{Q}}{A} \quad (2.1)$$

Radiation is the transfer of energy by electromagnetic waves. Every matter emits energy due to its thermodynamically positive temperature. This heat, however, is often neglected, since the transferred heat flux  $\dot{q}$  is proportional to the fourth order of the temperature  $\dot{q} \propto T^4$  [BAER & STEPHAN 2011]. Therefore, it commonly becomes relevant at temperatures above a couple of hundred degrees Celsius.

Heat conduction transfers energy between molecules based on a temperature gradient in a material. This mechanism plays the predominant role in solids and is most often superimposed in gases and liquids by convection. The transferred heat flux due to conduction is calculated using Fourier's law. For a 1D case, Fourier's law equals [POLIFKE & KOPITZ 2009]:

$$\dot{q} = -\lambda \frac{\partial T}{\partial z}. \quad (2.2)$$

The heat flux is proportional to the negative temperature gradient in the material, which aligns with the second law of thermodynamics, as it ensures that heat is transferred from regions of higher temperatures to regions of lower temperatures. The proportionality factor in equation (2.2) is the transfer coefficient for conductive heat transfer, also known as the thermal conductivity  $\lambda$ .

Convection describes the macroscopic movement of molecules in a fluid flow. It is mass bound and does not depend on a temperature gradient. Convective heat transfer on the other hand describes the transfer of heat between a fluid and a solid with differing temperatures, which move in relative motion towards each other [POLIFKE & KOPITZ 2009]. In this case, heat is transferred by a combination of conduction and convection, depending on the flow conditions near the solid's surface and the temperature. The fluid flow directly at the surface of the solid is considered stagnant for most flows. Because of the viscosity of the fluid, this leads to a boundary layer surrounding the solid's surface,

in which the fluid flow is strongly relaxed. Close to the solid's surface, heat is therefore mainly transferred by conduction in the direction normal to the solid. The evaluation of the transferred heat can be quite complex as the developed boundary layer depends on the flow conditions. Newton suggested an integral approach, where he defined a heat transfer coefficient  $\alpha$ , which correlates the heat flux with the driving temperature difference [BAER & STEPHAN 2011]:

$$\dot{q} = \alpha (T_{\text{bulk}} - T_{\text{wall}}) . \quad (2.3)$$

According to Newton, the heat stream is proportional to the difference between the temperature of the fluid's bulk phase  $T_{\text{bulk}}$  and the wall temperature  $T_{\text{wall}}$  of the solid. According to BAER & STEPHAN 2011, the heat transfer coefficient mainly depends on the flow conditions in the fluid phase and is similar for similar flow conditions. Different dimensionless correlations are available in literature for the calculation of heat transfer coefficients for different geometries and flow conditions. Thus, the heat transfer coefficient is accessible and the transferred heat stream can often be determined with Newton's approach. Considering equation (2.1), the transferred heat stream equals:

$$\dot{Q} = \alpha A (T_{\text{bulk}} - T_{\text{wall}}) . \quad (2.4)$$

## 2.1 Heat transfer across a tube

For the description of heat transfer across a tube, the case shown in figure 2.1 for a single tube is considered. A tube with the length  $L$ , the inner and outer radius  $r_i$  and  $r_o$ , respectively and the thermal conductivity  $\lambda_s$  is considered. The indices "i" and "o" correspond to the inner and outer tube surface, respectively. Cooling water flows through the inside of the tube with the temperature  $T_{\text{cw}}$ . Additionally, a fluid phase of temperature  $T_{\text{fl}}$  surrounds the tube. The temperature of the fluid phase is considered higher than the temperature of the cooling water. Consequently, heat is transferred from the fluid phase through the tube into the cooling water. At steady state, a constant temperature profile from the fluid bulk phase to the cooling water bulk phase is present.

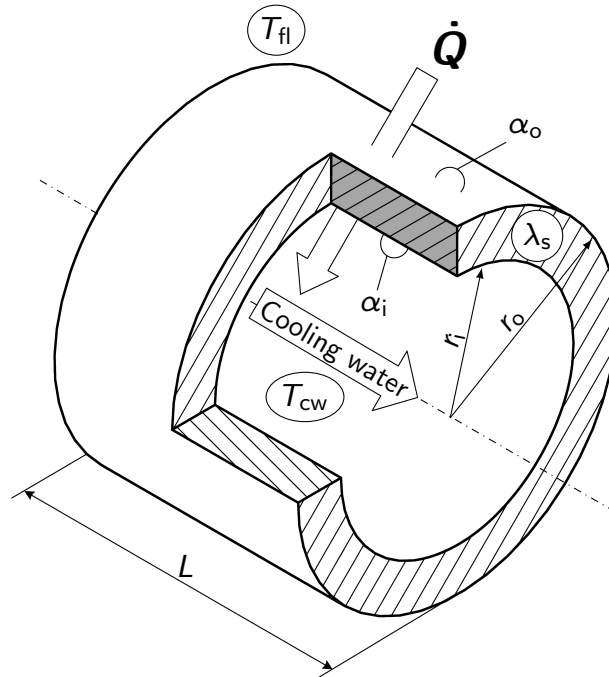


**Figure 2.1:** Example setup for heat transfer across a single tube [REIF 2016].

The discussion about heat transfer across a tube is further on considered for a cross section of the tube at a given axial position. In addition, it is assumed that the flow conditions inside and around the tube, respectively, are identical for all annular positions  $\varphi$ . With these assumptions, the system can be described as a one dimensional case.

A schematic of the temperature profile in radial direction is given in figure 2.2.

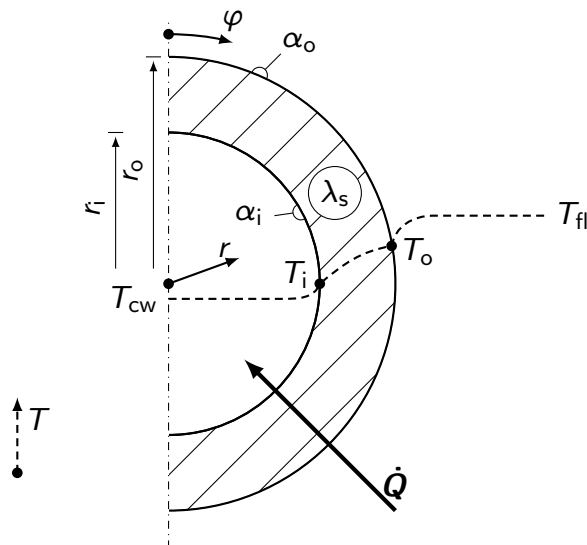


**Figure 2.2:** Temperature profile during heat transfer through a tube in radial direction for steady state [KLEINER 2014].

The heat stream  $\dot{Q}$  is directed towards the center of the tube and reaches from the fluid bulk phase through the tube into the cooling water bulk phase. The heat stream is constant across the radial position in steady state. Hence, it can be calculated based on conduction through the tube or convective heat transfer at the inside or outside of the tube.

### 2.1.1 Heat transfer resistance

A thermal resistance  $R$  is defined analogously to Ohm's law for electricity. The thermal resistance is then equal to the ratio between the driving temperature difference and the heat stream [REIF 2016].

#### Conduction

For the determination of the heat stream through conduction, the temperature profile between the inner and outer wall temperature  $T_i$  and  $T_o$ , respectively, is considered. According to equations (2.1) and (2.2), the heat stream equals:

$$\dot{Q} = -A(r) \lambda \left. \frac{\partial T}{\partial r} \right|_r = -2\pi r L \lambda \left. \frac{\partial T}{\partial r} \right|_r, \quad (2.5)$$

when considering a constant heat transfer coefficient  $\lambda$ . The differential equation is evaluated along the direction of the heat stream  $\dot{Q}$  from  $r_o$  to  $r_i$  by means of separation of variables. After the integration, the heat stream is equal to:

$$\dot{Q} = \frac{2\pi L \lambda}{\ln \frac{r_o}{r_i}} (T_o - T_i). \quad (2.6)$$

The thermal resistance  $R_\lambda$  of conduction through a tube is gained by rearranging equation (2.6).

$$R_\lambda := \frac{(T_o - T_i)}{\dot{Q}} = \frac{\ln \frac{r_o}{r_i}}{2\pi L \lambda} \quad (2.7)$$

#### Convective heat transfer

When rearranging equation (2.4), the following definition of the thermal resistance  $R_\alpha$  for convective heat transfer results:

$$R_\alpha := \frac{(T_{\text{bulk}} - T_{\text{wall}})}{\dot{Q}} = \frac{1}{\alpha A}. \quad (2.8)$$

For a tube geometry, the areas  $A_i$  and  $A_o$  refer to the surface area of the inner and outer tube surface, respectively.

$$A_i = 2\pi r_i L \quad ; \quad A_o = 2\pi r_o L \quad (2.9)$$

Rearranging equation (2.8), the transferred heat stream across the tube can be determined from the thermal resistance of the cooling water boundary layer and the fluid phase boundary layer, respectively.

$$\dot{Q} = \frac{(T_i - T_{cw})}{R_{\alpha_i}} = \alpha_i A_i (T_i - T_{cw}) . \quad (2.10)$$

$$\dot{Q} = \frac{(T_{fl} - T_o)}{R_{\alpha_o}} = \alpha_o A_o (T_{fl} - T_o) . \quad (2.11)$$

### 2.1.2 Overall heat transfer resistance

The heat stream may be determined by either one of equations (2.6), (2.10) or (2.11). However, the temperatures  $T_i$  and  $T_o$  at the inner and outer tube surface, respectively, are generally not accessible. The temperatures  $T_{cw}$  and  $T_{fl}$  of the two bulk phases on the other hand, are easily accessible, since a constant temperature throughout the bulk phase is present.

By considering that the heat transfer coefficients  $\alpha_i$  and  $\alpha_o$  can be determined from correlations and may, therefore, be considered as given, three unknown variables need to be determined. It is, thus, possible to evaluate the heat stream independently from the inner and outer tube surface temperatures by combining equations (2.6), (2.10) and (2.11). The relation for the heat stream  $\dot{Q}$  results in:

$$\dot{Q} = \frac{(T_{fl} - T_{cw})}{R_{\alpha_i} + R_\lambda + R_{\alpha_o}} = \frac{(T_{fl} - T_{cw})}{R_k} , \quad (2.12)$$

with the overall thermal resistance  $R_k$  for the regarded problem. An analogy between electricity and heat transfer can also be drawn for the overall resistance. As the individual heat resistances are connected in series during heat transfer across the tube, the overall thermal resistance ends up being equal to the sum of the individual resistances.

Comparing equation (2.12) with the definition of the thermal resistance for convective heat transfer, given in equation (2.8), an overall heat transfer coefficient  $k$  is evaluated.

$$R_k = \frac{1}{k A} = R_{\alpha_i} + R_\lambda + R_{\alpha_o} = \frac{1}{\alpha_i A_i} + \frac{\ln \frac{r_o}{r_i}}{2\pi L \lambda} + \frac{1}{\alpha_o A_o} \quad (2.13)$$

Depending on the selected reference area  $A$ , the overall heat transfer coefficient differs. For example, if we select the area  $A_o$  of the outer tube surface as reference area, the heat flux  $\dot{q}_o$  through the outer tube surface is calculated using equations (2.14) and (2.15) according to POLIFKE & KOPITZ 2009. The inner and outer heat transfer coefficients  $\alpha_i$  and  $\alpha_o$  are calculated using suitable correlations.

$$\dot{q}_o = \frac{\dot{Q}}{A_o} = k_o (T_{\text{fl}} - T_{\text{cw}}) \quad (2.14)$$

$$k_o = \left[ \frac{r_o}{\alpha_i r_i} + \frac{r_o}{\lambda} \ln \frac{r_o}{r_i} + \frac{1}{\alpha_o} \right]^{-1} \quad (2.15)$$

The heat flux is evaluated with the assumption of a one dimensional case. This heat flux, however, changes for the considered case of figure 2.1 in axial direction, since the temperature  $T_{\text{cw}}$  of the bulk phase of the cooling water changes, as it withdraws energy from the fluid phase along its way. The temperature  $T_{\text{fl}}$  of the bulk phase of the fluid is uniformly mixed and the assumption of a single temperature describing this entire bulk phase still holds true. For the evaluation of the heat stream across the tube, heat transfer coefficients for different axial positions have to be considered. Consequently, two adaptations to equations (2.14) and (2.15) therefore have to be made for the evaluation of the overall heat stream for the setup of figure 2.1. The idea is to calculate an average heat flux  $\dot{q}_o$  across the outer tube surface and use this average heat flux to determine the heat stream. When considering that the heat transfer coefficients are integral values for the description of the flow condition, the heat stream across the tube can be evaluated by using average values of the inner and outer heat transfer coefficients across the entire inner and outer tube surface, respectively. This is automatically done, by means of using correlations based on measurements for their evaluation. In addition, as the temperature of the cooling water changes in axial direction, the driving temperature difference ( $T_{\text{fl}} - T_{\text{cw}}$ ) also changes. For the considered setup, POLIFKE & KOPITZ 2009 derive an average driving temperature difference for the entire tube, which is called the logarithmic mean temperature difference.

## 2.2 Heat transfer during condensation on a horizontal smooth tube

According to KHARANGATE & MUDAWAR 2017, heat transfer during condensation is in general much larger compared to heat transfer in a single-phase without phase change. The term condensation describes the change of the physical state of a vapor into a liquid caused by an energy withdrawal. For condensation to take place, the specific latent heat of evaporation  $\Gamma$  has to be removed from the vapor phase. Under the prerequisite of thermodynamic equilibrium, the condensation of a pure substance occurs at a constant saturation temperature  $T_{\text{sat}}$ , where condensate and vapor are at saturation conditions.

For a closed system of a pure substance, the specific enthalpy  $h$  of the system is given in figure 2.3 in dependence of temperature.

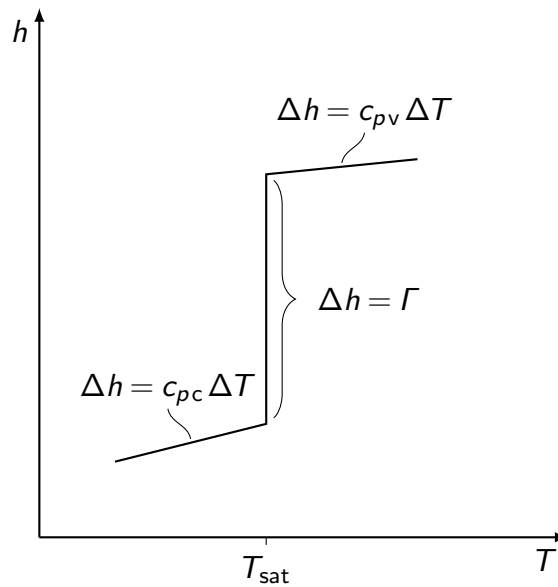


**Figure 2.3:** Specific enthalpy in dependence of temperature.

Below saturation temperature, only condensate is present, whereas above saturation temperature vapor is present. If the system is not at saturation conditions, a change in specific enthalpy  $\Delta h$  occurs because of a change in sensible heat, which is equal to the product of the specific heat capacity  $c_p$  of the fluid and the change in temperature  $T$ . At saturation conditions, both, condensate and vapor, are present simultaneously. Here, a change in specific enthalpy  $\Delta h$  is caused by a change in latent heat and is equal to the specific latent heat of evaporation  $\Gamma$ . For a vapor to be liquefied, the specific latent heat of evaporation  $\Gamma$  has to be removed from the vapor phase, as it is released during condensation. This causes a constant temperature at the phase boundary during phase change, as given in figure 2.3. However, a constant temperature across the interface would prevent heat from being transferred. Therefore, BAER & STEPHAN 2011 state that in reality, a usually neglectable temperature gradient has to be present across the phase boundary during condensation.

When vapor is in contact with a cold surface, heat is transferred from the vapor phase to the surface. This causes a decrease in temperature in the vapor phase close to the surface. If the temperature reaches its saturation temperature for the given pressure, condensate will be formed. Condensate is then subcooled because of the cold surface and more vapor is liquefied at the interface, leading to the formation of additional condensate. Because of the large change in density during condensation, vapor flows continuously to the interface, where it is liquefied. Thus, condensation depends on heat and mass transfer, as new vapor has to be transported to the interface [BAER & STEPHAN 2011]. Three heat transfer resistances, which are aligned in series, have to be considered during condensation for the determination of the resulting heat transfer coefficient  $\alpha_o$  at the outside of the tube. According to BAER & STEPHAN 2011, the three

thermal resistances are caused by the supply of vapor to the interface, the conversion of vapor into condensate and the thermal resistance in the condensate phase, respectively. The thermal resistance caused by the supply of vapor to the interface is in general negligible for pure substance condensation, but can become the prominent resistance during condensation of mixtures [BÜCHNER 2016]. The thermal resistance due to phase change is associated with the molecular kinetics during phase change and causes a temperature drop at the interface of only a few hundredths of a Kelvin [BAER & STEPHAN 2011]. In general, this resistance is neglectable, leaving the thermal resistance of the condensate as the prominent resistance during condensation of pure substances. As a result, the outer heat transfer resistance during condensation of a pure substance on a horizontal tube is mainly influenced by the condensate flow.

### 2.2.1 Condensate flow

For the description of the condensate flow during condensation, two different aspects must be considered. First, the condensate flow on the tube surface is regarded, where focus is laid on the wetting behavior. Afterwards, the different modes of the condensate flowing off from the tube are regarded.

#### Surface wetting

Condensation on a cold surface may occur in two different ways, which are depicted in figure 2.4, depending on the interaction between fluid and surface.

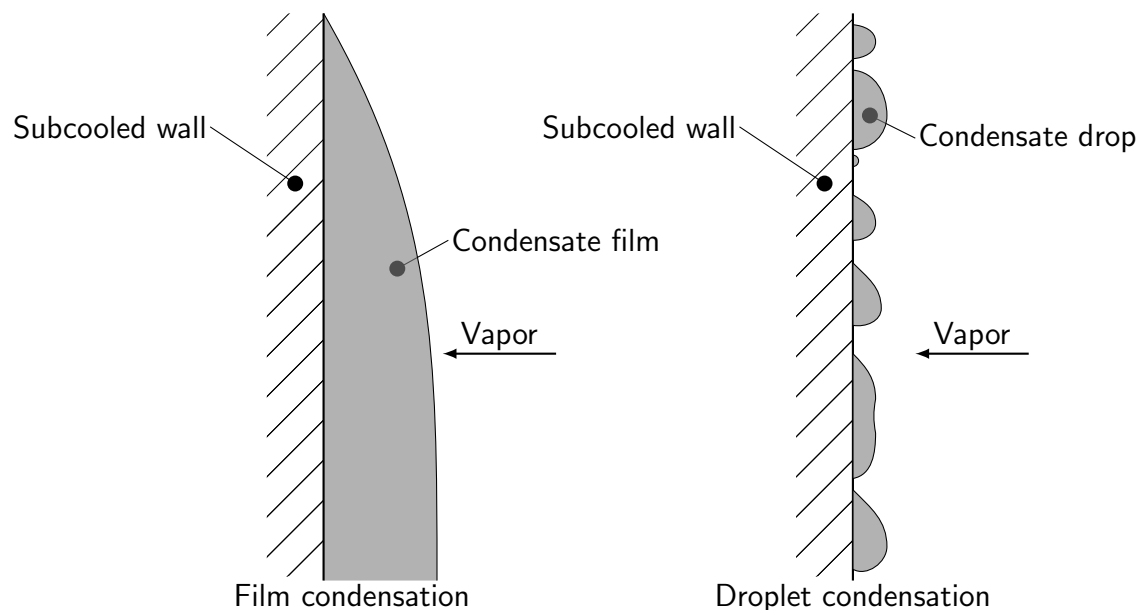


**Figure 2.4:** Formed condensate on a subcooled wall during film and droplet condensation [BERGMAN ET AL. 2011].

According to BERGMAN ET AL. 2011, the most common form of condensation is film condensation, where the condensate forms a continuous film on the surface, which streams in either a laminar or turbulent way. The condensate phase can also form droplets instead of a continuous film. In this case, the process is called droplet condensation. Whether film condensation or droplet condensation occurs is depending on the interaction between the condensate and the wall. If the surface is completely wetted, film condensation occurs. Otherwise, droplet condensation takes place. Film condensation generally occurs on clean, uncontaminated surfaces [BERGMAN ET AL. 2011]. The wetting behavior depends on the relation of the specific energies required to increase the area of an interface between the interfaces solid/liquid, solid/vapor and vapor/liquid. This specific energy manifests in the better known surface tension  $\sigma$  [CZESLIK ET AL. 2010]. The shape of a condensate droplet on a surface is influenced by the forces acting on it. Therefore, the tensions of the three interfaces between the phases solid, condensate and vapor have to be in equilibrium for a static droplet [BAER & STEPHAN 2011]. Figure 2.5 shows a condensate droplet on a solid surface. The aforementioned equilibrium of the surface tension is illustrated at the boundary of the three phases.

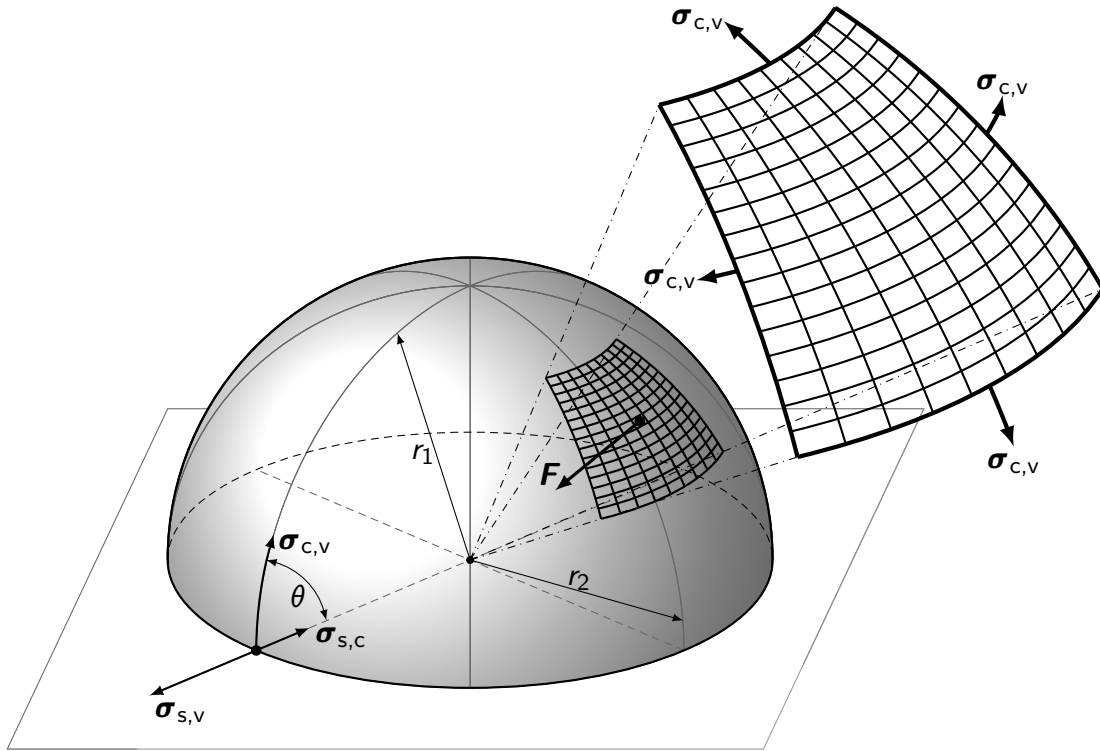


**Figure 2.5:** Surface tension forces acting on the phase boundaries.

For a static drop, forces due to surface tension acting in the boundary of the three phases are at equilibrium and the formed contact angle  $\theta$  can be calculated by equation (2.16), according to YOUNG 1805.

$$\sigma_{s,v} - \sigma_{s,c} = \sigma_{c,v} \cos(\theta) \quad (2.16)$$

Droplets are formed for a finite value of the contact angle. This is the case if  $\sigma_{s,v} - \sigma_{s,c} > \sigma_{c,v}$ , as the force equilibrium of figure 2.5 can not exist otherwise. For a contact angle of  $\theta = 0^\circ$ , complete wetting occurs.

Additionally, considering the enlarged section of the interface in figure 2.5, the surface tensions  $\sigma_{c,v}$  acting in the projected section of the interface add up to zero in the two dimensional space of the interface. However, a resulting force  $\mathbf{F}$  normal to the interface exists, because of the curvature of the interface. In order for a droplet to not collapse, an increased pressure has to be present inside the droplet for force equilibrium. The pressure increase is calculated using the Young-Laplace equation (2.17) [YOUNG 1805, LAPLACE 1805], where the two radii  $r_1$  and  $r_2$  are perpendicular towards each other.

$$\Delta p = \sigma \left( \frac{1}{r_1} - \frac{1}{r_2} \right) \quad (2.17)$$

### Condensate flow off

At the bottom part of a regarded horizontal tube, condensate accumulates during condensation and is withheld by adhesion forces. This leads to a state where a heavier fluid (condensate) rests above a lighter fluid (vapor) which is a pseudo stable state, as any disturbance to the interface will result in a wavelike deformation of the interface. This wavelike deformation is known as the Rayleigh–Taylor instability [RAYLEIGH 1883, TAYLOR 1950] and is depicted in figure 2.6.

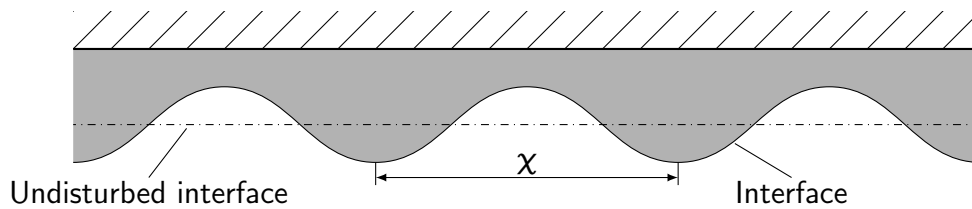


**Figure 2.6:** Interface deformation of the Rayleigh–Taylor instability [PALACIO MONTES 2018].

TAYLOR 1950 and LEWIS 1950 originally proposed the instability of the interface between a liquid resting above a gas phase. They further showed that this disturbance will grow exponentially if the ratio between the amplitude and wavelength of the disturbed interface is below 0.4. According to MILNE-THOMSON 1960, surface tension has a stabilizing effect on the disturbance. Short disturbances will stabilize themselves, whereas long disturbances will lead to an expansion of the interface and a stripping off of the condensate at the bottom of the tube. The wavelength at which the disturbance will grow most rapidly is called the most unstable wavelength  $\chi$  [HONDA ET AL. 1987], which equals:

$$\chi = 2\pi \sqrt{\frac{C \sigma}{g(\rho_c - \rho_v)}}. \quad (2.18)$$

According to YOUNG ET AL. 1980,  $C = 2$  for thin condensate layers and  $C = 3$  for thick condensate layers.

Depending on the flow rate of condensate stripping off, the tube geometry and the spacing below the tube, different flow patterns of the falling condensate result. The different flow patterns are shown in figure 2.7 [MITROVIĆ 1986, HONDA ET AL. 1987]. For a low condensate flow rate, droplets form at the bottom of the tube and drip-off (Droplet mode). With increasing flow rate, the drip-off frequency increases, to the point where enough condensate is supplied, so that no ripping off of the condensate occurs and a condensate column is formed (Column mode). At very high condensate flow rates, a continuous sheet of condensate is formed below the tube (Sheet mode).

According to HONDA ET AL. 1987, the required mass flow rate  $\dot{m}_c$  of the condensate for the transition from droplet to column mode is calculated using equation (2.19).

$$\dot{m}_c \approx 0.122 L \left( \frac{\rho_c}{g} \right)^{1/4} \sigma^{3/4} \quad (2.19)$$

HONDA ET AL. 1987 further showed that the spacing of condensate columns equals the most unstable wave length  $\chi$ . During droplet mode not every drip-off point is active, which is why the average spacing between drip points is higher compared to the column mode. In addition, the average spacing between the droplets decreases with increasing mass flow rate of the condensate and reaches the most unstable wave length  $\chi$  at the transition to column mode.

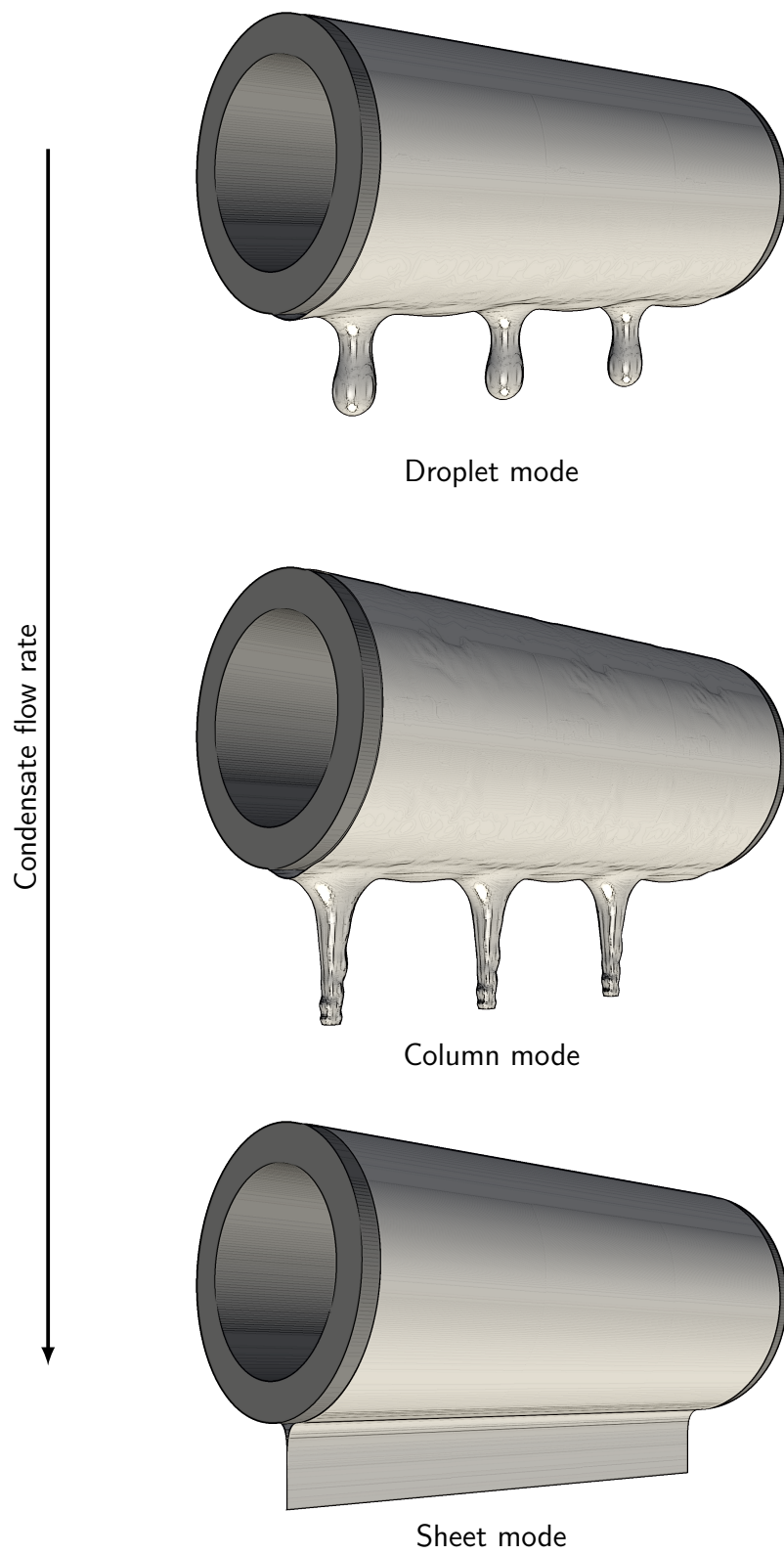


**Figure 2.7:** Different condensate flow patterns during condensate strip-off.

## 2.2.2 Calculation of the outer heat transfer coefficient

Within this work, only film condensation of pure substances is considered. The outer heat transfer of pure substance condensation on a horizontal smooth tube is described by Nusselt's film theory [NUSSELT 1916a]. The formed condensate film along the tube's circumference during free convection according to NUSSELT 1916a is illustrated in figure 2.8.

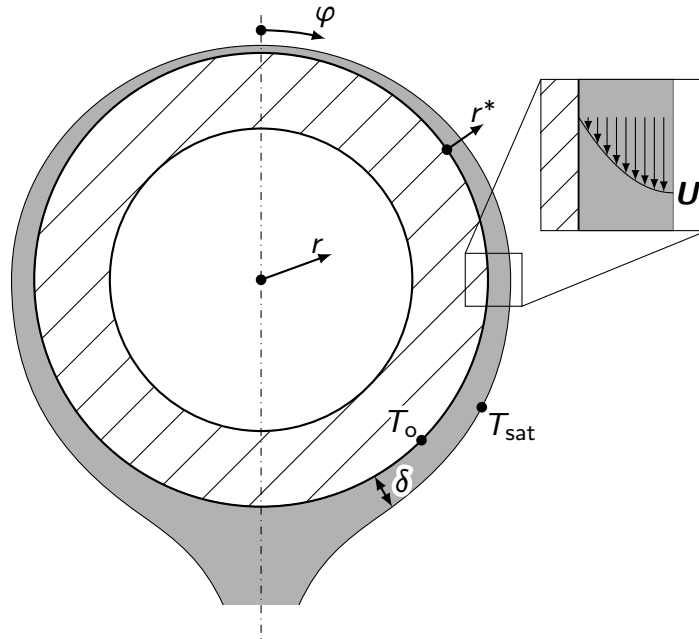


**Figure 2.8:** Condensate film according to Nusselt's film theory [NUSSELT 1916a].

Condensate runs off along the tube surface in annular direction. Since new condensate is formed along the way, the condensate's film thickness increases. Nusselt derived a relation for the outer heat transfer coefficient during pure substance condensation on a horizontal smooth tube using the following assumptions and boundary conditions [NUSSELT 1916b, NUSSELT 1916a].

### Assumptions

- Constant material properties are assumed.
- Steady state is reached.
- Shear stress at the phase interface is neglected.
- Surface tension is neglected.
- Changes in kinetic energy of the condensate are neglected.
- A thin condensate film is present, leading to the following simplifications:
  - The inertia of the condensate is neglected.
  - The curvature of the phase interface is neglected.

- The condensate velocity is parallel to the tube wall.
- A linear temperature profile normal to the tube wall can be considered.

### Boundary Conditions

- A constant temperature  $T_o$  across the outer tube surface is assumed.  
 $T(r^* = 0) = T_o$
- The phase interface temperature equals saturation temperature.  
 $T(r^* = \delta) = T_{\text{sat}}$
- Non-slip at the outer tube surface is considered.  
 $U(r^* = 0) = 0$
- Shear stress is neglectable at the phase interface.  
 $\left. \frac{\partial U}{\partial r^*} \right|_{r^*=\delta} = 0$

Based on these assumptions and boundary conditions, NUSSELT 1916a derives the following relation between the film thickness  $\delta$  and the revolution angle  $\varphi$ .

$$\delta(\varphi) = \Psi(\varphi) \left[ 3 \frac{\eta_c r_o \lambda_c (T_{\text{sat}} - T_o)}{\Gamma \varrho_c (\varrho_c - \varrho_v) g} \right]^{1/4} \quad (2.20)$$

The stream function  $\Psi(\varphi)$  is given in equation (2.21), where  $C$  corresponds to an integration constant.

$$\Psi(\varphi) = \left[ \frac{4}{3 (\sin \varphi)^{4/3}} \int (\sin \varphi)^{1/3} d\varphi + \frac{C}{(\sin \varphi)^{4/3}} \right]^{1/4} \quad (2.21)$$

If no condensate is dripping onto the top of the tube at  $\varphi = 0$ , then  $\Psi$  has to have a finite number. Hence, the integration constant has to be equal to  $C = 0$ . The integral in equation (2.21) does not have an analytical solution but can be solved numerically.

Because of a thin condensate film, heat is only transferred in radial direction due to conduction. The local heat transfer coefficient may be evaluated with the following relation.

$$\alpha(\varphi) = \frac{\lambda_c}{\delta(\varphi)} = \frac{1}{\Psi(\varphi)} \left[ \frac{1}{3} \frac{\Gamma \varrho_c (\varrho_c - \varrho_v) \lambda_c^3 g}{\eta_c r_o (T_{\text{sat}} - T_o)} \right]^{1/4} \quad (2.22)$$

The heat transfer coefficient  $\alpha_{\text{Nu}}$  of the outer surface of a tube according to Nusselt's film theory is gained by solving the following equation.

$$\alpha_{\text{Nu}} = \frac{1}{\pi} \int_0^\pi \alpha(\varphi) d\varphi \quad (2.23)$$

After integrating equation (2.23), the outer heat transfer coefficient  $\alpha_{\text{Nu}}$  equals:

$$\alpha_{\text{Nu}} = 0.728 \left[ \frac{1}{2} \frac{\Gamma \rho_c (\rho_c - \rho_v) g \lambda_c^3}{\eta_c r_o (T_{\text{sat}} - T_o)} \right]^{1/4}. \quad (2.24)$$

A schematic temperature profile for pure substance condensation on a horizontal smooth tube according to Nusselt's film theory is given in figure 2.9.

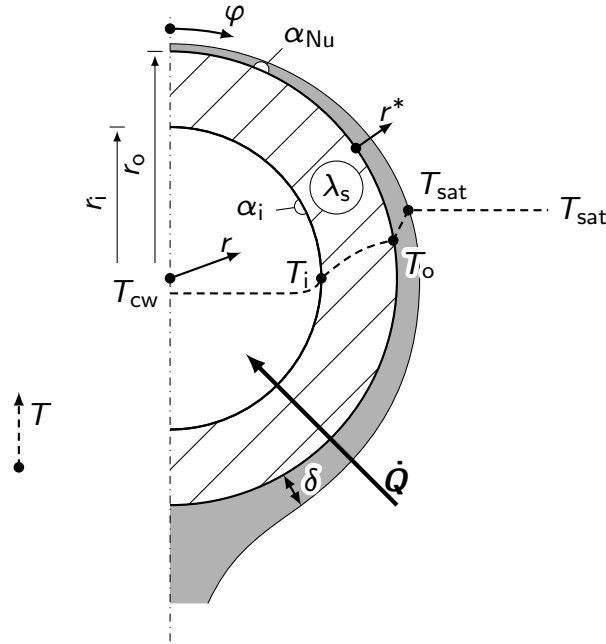


**Figure 2.9:** Temperature profile in radial direction during condensation on the outside of a tube for steady state [KLEINER 2014].

## 2.3 Surface-structured tubes

Heat transfer is enhanced during condensation, as compared to single-phase heat transfer. According to POLIFKE & KOPITZ 2009, it is possible to increase the efficiency of tube bundle condensers by using surface-structured tubes instead of smooth tubes. Basic surface structures for the outside of horizontal tubes are annular fins, which are also utilized for increased single-phase heat transfer. However, while the fin dimensions for single-phase heat transfer may vary in a wide range, annular fins for improved efficiency during condensation have fin dimensions around 1 mm and below.

An isometric view, with a cutout section, of an annular low-finned tube with vertical fins is given in figure 2.10.

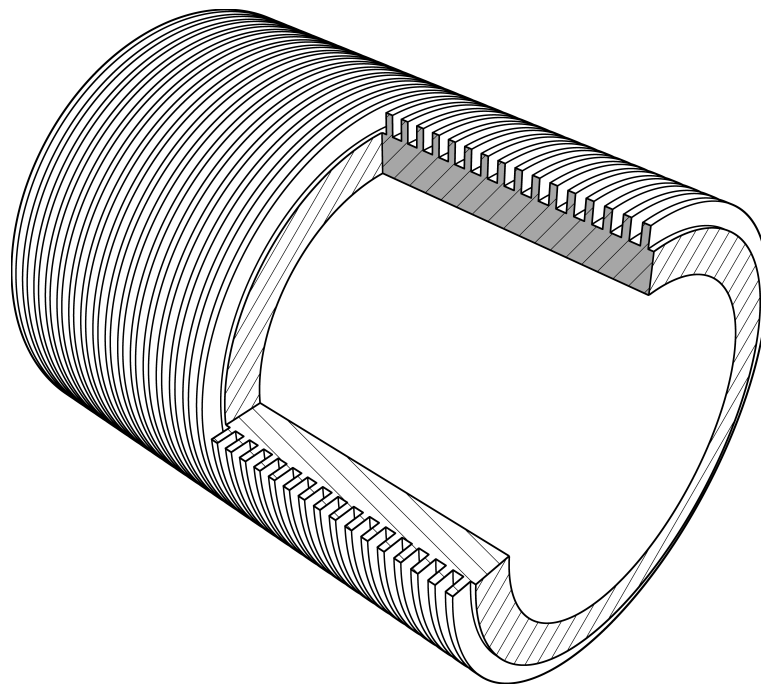


**Figure 2.10:** Isometric view of an annular low-finned tube [REIF 2016].

Figure 2.11 shows a schematic of the cross section of the fins with relevant geometric parameters. Since only annular low-finned tubes are considered within this work, these tubes will further on be referred to as finned tubes.

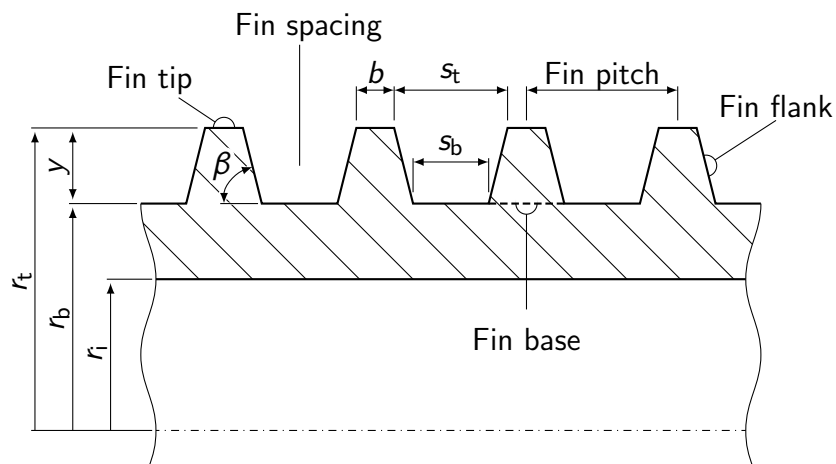


**Figure 2.11:** Cross section of the fin structure of annular low-finned tubes.

As illustrated in figure 2.11, relevant geometric parameters of the fins are the thickness  $b$  at the fin tip, the fin spacing  $s_b$  at the fin base, the fin spacing  $s_t$  at the fin tip, the fin height  $y$  and the incline angle  $\beta$  of the fin. While the inner radius  $r_i$  can be analogously defined to the one of a smooth tube, two outer radii have to be differentiated because of the fins. For the considered finned tubes, the outer radius  $r_t$  corresponds to the radius

reaching to the fin tips, whereas the fin base radius  $r_b$  refers to the radius reaching to the fin base.

Reif et al. [REIF ET AL. 2019] showed that the heat transfer coefficient during condensation of hydrocarbons can be increased by a factor of 5 to 8 when utilizing a finned tube compared to a smooth tube. The surface area on the other hand is only increased by a factor of about 2.7 due to the fin structure. Consequently, the fins not only increase the exchange area for heat transfer, they also influence the condensate flow during condensation in a way, which increases heat transfer.

### 2.3.1 Condensate flow

The formed condensate along the finned tubes during condensation is illustrated in figure 2.12.

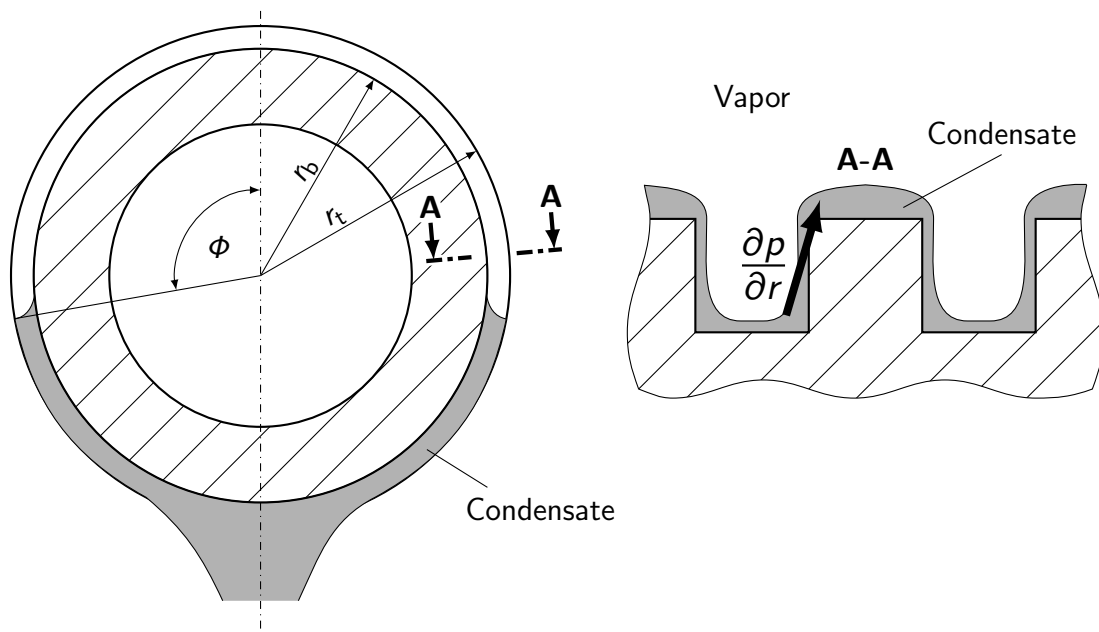


**Figure 2.12:** Formed condensate film during condensation on the outside of annular low-finned tubes [KLEINER 2014].

The fins cause the interface of the formed condensate to curve around them. According to the Young-Laplace equation (2.17), this leads to a pressure increase at the fin tip and a pressure decrease between the fins at the fin base, resulting in a pressure gradient as illustrated in figure 2.12 on the right hand side. HONDA ET AL. 1983 state that because of the small dimensions of the fins, the pressure gradient evokes forces, which are far stronger than gravitational forces, leading to a surface tension driven condensate flow. Since the fins function as capillaries, the forces caused by their structure are further on referred to as capillary forces.

The capillary forces are oriented in opposite direction to the pressure gradient and cause the condensate to flow from the fin tip into the fin spacing to the fin base. This

leads to a very thin condensate film along the fin flank in the upper region of the tube, where gravitational forces and capillary forces are oriented in the same direction. In the bottom region of the tube, however, capillary forces and gravitation forces are oriented in opposite directions, retaining the condensate in between the fins and, thus, flooding the fin spacing. This flooding behavior was first investigated by KATZ ET AL. 1974. TABOREK 1974 first reported that the retention effect can be significant for fluids with large ratios between the material properties surface tension and density. This assumption coaligns with models describing the flooding behavior, i. e. equation (2.25) of HONDA ET AL. 1983.

As the condensate film acts as a thermal resistance, the non-flooded region is considered the active region of the tube and therefore, the flooded region decreases the effective surface area for heat transfer [HONDA ET AL. 1983]. During her studies on a GEWA-K30 tube from Wieland, REIF 2016 found that condensation of water will flood the entire tube spacing and shows decreased heat transfer compared to a smooth tube due to its large ratio between surface tension and density. In general, it is assumed that the flooding behavior has a major impact on heat transfer.

The portion of the flooded region of the tube is quantified by the flooding angle  $\Phi$ , illustrated in figure 2.12. The flooding angle is defined according to HONDA ET AL. 1983 as the angle between the lines connecting the center of the tube with the top of the tube and the point where the entire fin spacing is filled with condensate, respectively. HONDA ET AL. 1983 found the analytical solution, given in equation (2.25), for estimating the flooding angle by solving a force equilibrium of the condensate.

$$\Phi = \arccos \left( \frac{2 \sigma \cos \left( \frac{\pi}{2} - \beta \right)}{\rho_c g s_t r_t} - 1 \right) \quad (2.25)$$

### 2.3.2 Heat transfer models

Before presenting different heat transfer models, it is important to discuss the different options when evaluating an outer heat transfer coefficient for finned tubes. Since the dimensions of the fin geometry are very small, there are different options for the definition of the outer surface area of the tube, which will function as the reference area for the outer heat transfer coefficient. According to REIF 2016, the possible reference areas are the actual outer surface of the finned tube and the lateral surface of a smooth tube with either the radius  $r_t$  or  $r_b$ . In addition to the different possible surface areas, the consideration of heat conduction through the tube can also vary. Either conduction is considered from the inner tube surface to the fin base or to the fin tip. It would also be possible to consider conduction through the fins by using the fin efficiency. It is crucial that the definition of the outer heat transfer coefficient is stated as clearly as possible and that the described differences are considered when comparing different data sets or models.

As previously mentioned, during pure substance condensation, the thermal resistance at the outside of the tube is mainly influenced by conduction through the condensate film. Hence, the non-flooded region of the tube will show significantly higher heat transfer coefficients compared to the flooded region of the tube. Therefore, it is important that the considerations about the flooding angle are included in a universal model for the heat transfer coefficient. A brief overview of relevant heat transfer models follows based on the summary of BÜCHNER 2016.

The first model for heat transfer of finned tubes was developed by BEATTY & KATZ 1948. However, they assume that gravity dominates the condensate flow along the fins and therefore, did not consider a flooded region of the tube. First models assuming a surface tension driven flow of the condensate along the fin surface were developed by RUDY & WEBB 1983a and HONDA & NOZU 1987. RUDY & WEBB 1983a considered flooding of the bottom region of the tube, defined a flooding angle and neglected heat transfer in the flooded region. A similar approach was published by HONDA & NOZU 1987, who used numerical analysis for the thin film along the fin for a fixed annular position in the non-flooded region and split the fin's structure into different regions. For each region, a dimensionless heat stream is evaluated separately. Afterwards, an overall heat transfer coefficient is calculated by combining these heat streams. They further evaluated the non-flooded and flooded region separately and combined them to an average heat transfer coefficient. Despite this profound approach of modeling heat transfer, the results show deviations to measurements of up to  $\pm 80\%$ .

ROSE 1994 developed a model which was fitted to measurements of HONDA ET AL. 1983 and WEBB ET AL. 1985. The model is able to evaluate the heat transfer coefficient for multiple data sets with a deviation below  $\pm 20\%$ . His model was further improved by BRIGGS & ROSE 1994. Their model splits the transferred heat stream into three separate heat streams: one for the flooded region, one for the fin and one for the base of the fin spacing. In the flooded region, heat is only transferred across the fin tip. The fin spacing is considered adiabatic. The heat stream for the fin and the base of the fin spacing are only considered for the non-flooded region. The heat stream of the fin considers the transferred heat across the fin tip and the fin flank, while the heat stream at the base of the fin spacing only considers the heat stream across the lateral surface of the fin spacing with radius  $r_b$ .

A different approach was pursued by KUMAR ET AL. 1998. They used a set of dimensionless numbers to calculate the condensation number  $Cn$  given in equation (2.26).

$$Cn = \frac{\alpha_o}{\lambda_c} \left( \frac{\eta_c^2}{\rho_c^2 g} \right)^{1/3} \quad (2.26)$$

KUMAR ET AL. 2002 use three dimensionless numbers for the function of the condensation number, the film Reynolds number  $Re_F$ , the Weber number and an additional dimensionless number, which considers the dimensions of the fins. KUMAR ET AL. 2002 state that they use the Weber number suggested by RUDY & WEBB 1983b. However,

their resulting dimensionless number considers the ratio between the surface tension force and the gravitational force, while the Weber number considers the ratio between inertia and surface tension forces. Hence, their Weber number should rather be called the Eötvös number or Bond number.

### Heat transfer model of Reif et al.

REIF ET AL. 2019 also used a set of dimensionless numbers for the condensation number  $Cn$  in their heat transfer model. The used dimensionless numbers are the film Reynolds number  $Re_F$ , the Bond number  $Bo$ , a dimensionless number  $Ro$  considering tube properties and the ratio between the fin thickness  $b$  and the fin spacing  $s$ . Since REIF ET AL. 2019 only evaluated vertical fins, the fin spacing at the tip and base of the fin has to be equal:  $s_t \stackrel{!}{=} s_b = s$ . The following equation for the condensation number was found:

$$Cn = C Re_F^{-1/3} Bo^{1.98} Ro^{0.17} \left(\frac{b}{s}\right)^{2.26} \quad (2.27)$$

The film Reynolds number  $Re_F$  considers the mass flow rate of the condensate and is given in equation (2.28). As the flooding angle is depending on the ratio between gravitational forces and capillary forces, its influence upon the heat transfer coefficient is considered by the bond number  $Bo$ , given in equation (2.29). The influence of the fin width  $b$  is considered with the ratio  $b/s$ . The dimensionless number  $Ro$ , given in equation (2.30), includes the material properties of the tube and the fin height.

$$Re_F = \frac{2 \dot{m}}{\eta L} = \frac{2 \dot{Q}}{\eta L \Gamma}. \quad (2.28)$$

$$Bo = \frac{2 r_t (\rho_c - \rho_v) g s}{\sigma} \quad (2.29)$$

$$Ro = \frac{\left(\frac{\lambda_s}{\rho_s c_{ps}}\right)^2}{g y^3} \quad (2.30)$$

The dimensionless number  $Ro$  mainly needs to be included because of the previously discussed issues when defining heat transfer coefficients for low-finned tubes. The outer heat transfer coefficient of REIF ET AL. 2019 for example refers to the outer lateral surface of a smooth tube with radius  $r_t$  according to BÜCHNER ET AL. 2015. In addition, they consider conduction through the tube from the inner tube surface to the fin base. Due to these considerations, the efficiency of the fin structure influences their measured heat transfer coefficients. Hence, the tube properties influence the measured heat transfer coefficient and need to be considered within the model.

When comparing heat transfer coefficients from different models with each other, it is crucial that the evaluated heat transfer coefficients of each model are adjusted to the same definitions for heat conduction through the tube and the reference surface area. Despite doing so, REIF 2016 showed that there is still a wide discrepancy between the calculated heat transfer coefficients of different available models.

# 3 Computational Fluid Dynamics

According to TANNEHILL ET AL. 1997, high speed computing greatly influences the way principles from fluid dynamics and heat and mass transfer are applied in engineering. 30 years ago, CFD was limited to simple flow configurations with 2D cases, whereas today, CFD is used in many engineering applications with complex flows.

TANNEHILL ET AL. 1997 state that solving engineering problems can be accomplished by either of three different methods: by experiment, by an analytical solution or by a numeric approach. CFD is a numeric approach to solving the Navier–Stokes equations for a flow problem, where the regarded domain is discretized. Depending on the problem at hand, different discretization methods are available. The finite volume discretization is generally used for CFD problems, where the domain is subdivided into finite sub volumes.

The finite volume discretization is described in section 3.1. First the underlying mathematical description of fluid flow and heat transfer in a single-phase is discussed. The adaption to a two-phase flow is presented in section 3.2.

The mathematical description along with the resulting transport equations is well documented in literature. The theory behind this CFD approach is presented for a laminar single-phase transport and is oriented at the dissertations of JASAK 1996, MARSCHALL 2011 and HABLA 2014.

According to MARSCHALL 2011, the approach in CFD is to balance generally conserved quantities such as mass, momentum and in this work, enthalpy. An incompressible Newtonian fluid with temperature independent properties are assumed. A spatially and temporally fixed control volume (CV) with its volume  $V$  of arbitrary shape and size is considered, as shown in figure 3.1.

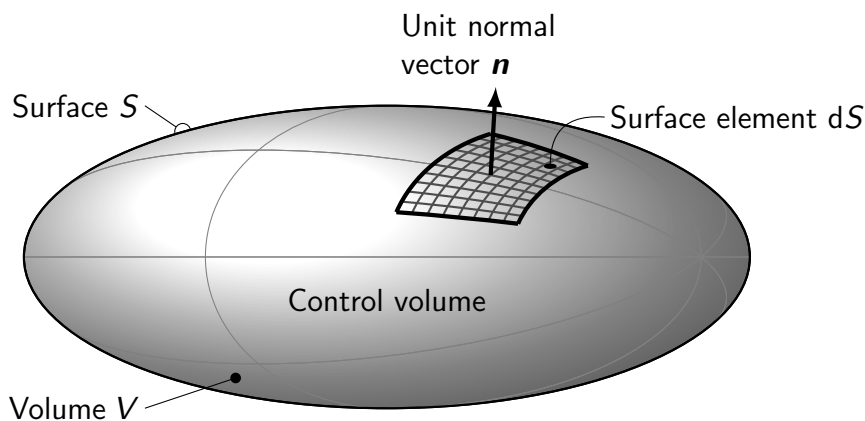


**Figure 3.1:** Arbitrary control volume [MARSCHALL 2011].

The surface  $S$  of the considered CV with volume  $V$  can be described as the integral across infinitesimal surface elements. The unit normal vector  $\mathbf{n}$  of a surface element  $dS$  directed outwards from the CV is also shown in figure 3.1. The fluid inside the CV has the density  $\rho$  and a velocity  $\mathbf{U}$ , crossing the surface element  $dS$ .

Considering an arbitrary intensive quantity  $\xi$  of the flow, which can be a scalar, vector or tensor, and is the intensive equivalent of an extensive quantity, e. g. a mass specific enthalpy, its change within the CV can be calculated using balance equations, similar to balancing extensive quantities. The rate of change of  $\xi$  is given in equation (3.1) and is equal to the sum of the convective and conductive transfer of the arbitrary quantity across the control surface and source or sink terms of the arbitrary quantity within the CV.

$$\begin{aligned} \frac{d}{dt} \int_V \rho \xi \, dV &= - \oint_S \mathbf{n} \cdot (\rho \xi \mathbf{U}) \, dS && \text{Convection} \\ &- \oint_S \mathbf{n} \cdot (-\lambda_\xi \nabla \xi) \, dS && \text{Conduction} \\ &+ \int_V \mathcal{S}_\xi \, dV && \text{Source/Sink} \end{aligned} \quad (3.1)$$

The transfer coefficient for diffusive transfer  $\lambda_\xi$  of the arbitrary intensive quantity is a fluid property, whereas the volumetric source or sink term  $\mathcal{S}_\xi$  depends on the regarded flow. The source or sink term is further on only referred to as source term. The intensive quantity  $\xi$  is multiplied with  $\rho$  since it is considered mass specific. The left hand side of equation 3.1 may be switched to a volume integral of the temporal derivative by using the Leibniz-Reynolds transport theorem given in equation (3.2). The surface integrations on the right hand side of equation 3.1 can be transformed to a volume integral using the Gauss theorem for the divergence and gradient operator, given in equations (3.3) and (3.4), respectively, for the extensive quantity  $\rho \xi$ . Both theorems are valid for any CV with volume  $V$ .

$$\frac{d}{dt} \int_V \rho \xi \, dV = \int_V \frac{\partial}{\partial t} (\rho \xi) \, dV + \oint_S \mathbf{n} \cdot \mathbf{U}_S (\rho \xi) \, dS \quad (3.2)$$

$$\oint_S \mathbf{n} \cdot (\rho \xi) \, dS = \int_V \nabla \cdot (\rho \xi) \, dV \quad (3.3)$$

$$\oint_S \mathbf{n} (\rho \xi) \, dS = \int_V \nabla (\rho \xi) \, dV \quad (3.4)$$

The displacement velocity  $\mathbf{U}_S$  of the control surface of the considered spatially and temporally fixed CV equals  $\mathbf{U}_S = 0$ . Hence, the last term on the right hand side of equation (3.2) is omitted.

The Gauss theorem may be used on the convection and the conduction term in equation (3.1). The following relation is gained, when using both theorems, equations (3.2) and (3.3), on the generic transport equation (3.1), respectively.

$$\int_V \left[ \frac{\partial}{\partial t}(\varrho \boldsymbol{\xi}) + \nabla \cdot (\varrho \boldsymbol{\xi} \mathbf{U}) - \nabla \cdot (\lambda_\xi \nabla \boldsymbol{\xi}) - \mathcal{S}_\xi \right] dV = 0. \quad (3.5)$$

Since equation (3.5) is valid for any arbitrary volume  $V$ , its integrand is also equal to zero. This leads to the generally known form of the generic transport equation for the arbitrary quantity  $\boldsymbol{\xi}$ .

$$\frac{\partial}{\partial t}(\varrho \boldsymbol{\xi}) + \nabla \cdot (\varrho \boldsymbol{\xi} \mathbf{U}) - \nabla \cdot (\lambda_\xi \nabla \boldsymbol{\xi}) - \mathcal{S}_\xi = 0 \quad (3.6)$$

The conservation equations for mass, momentum and enthalpy have the same basic structure as equation (3.1). Generally, the only differences are the conserved quantity  $\boldsymbol{\xi}$ , the coefficient for diffusive transfer  $\lambda_\xi$  and the volumetric source term  $\mathcal{S}_\xi$ .

**Mass** The conservation equation for mass equals:

$$\frac{\partial}{\partial t}(\varrho) + \nabla \cdot (\varrho \mathbf{U}) = 0. \quad (3.7)$$

Since an incompressible fluid with temperature independent properties is considered, the density  $\varrho$  is considered constant in time and space and can be eliminated from equation (3.7). Thus, the conservation equation reduces to:

$$\nabla \cdot (\mathbf{U}) = 0. \quad (3.8)$$

**Momentum** The momentum conservation according to FERZIGER & PERIĆ 2002 is given in equation (3.9).

$$\frac{\partial}{\partial t}(\varrho \mathbf{U}) + \nabla \cdot (\varrho \mathbf{U} \mathbf{U}) - \nabla \cdot \boldsymbol{\tau} = \varrho \mathbf{g} - \nabla p \quad (3.9)$$

The diffusive transfer of momentum is considered by the stress tensor  $\boldsymbol{\tau}$ . The given momentum conservation equation considers the gravitational acceleration  $\mathbf{g}$  and pressure gradients  $\nabla p$  in the domain as source terms on the right hand side of equation (3.9). For Newtonian fluids, the stress tensor is given by HOLZMANN 2017:

$$\boldsymbol{\tau} = 2\eta \mathbf{D} + \left[ -\frac{2}{3}\eta + \varkappa \right] \nabla \cdot (\mathbf{U} \mathbf{I}), \quad (3.10)$$

where  $\eta$  is the dynamic viscosity,  $\mathbf{D}$  the strain-rate tensor [HOLZMANN 2017],  $\varkappa$  is described as the bulk viscosity [BIRD ET AL. 2007], which may be ignored for dense fluids and  $\mathbf{I}$  is the unit tensor. The strain-rate tensor  $\mathbf{D}$  equals:

$$\mathbf{D} = \frac{1}{2} (\nabla \mathbf{U} + [\nabla \mathbf{U}]^T) . \quad (3.11)$$

The second term on the right hand side of equation (3.10) considers expansion and compression of the fluid [HOLZMANN 2017] and can be neglected for incompressible fluids. For an incompressible Newtonian fluid, the momentum conservation then reads:

$$\frac{\partial}{\partial t}(\varrho \mathbf{U}) + \nabla \cdot (\varrho \mathbf{U} \mathbf{U}) - \nabla \cdot [\eta (\nabla \mathbf{U} + [\nabla \mathbf{U}]^T)] = \varrho \mathbf{g} - \nabla p \quad (3.12)$$

**Enthalpy** The enthalpy balance for single-phase flow is given in equation (3.13) [TANNEHILL ET AL. 1997].

$$\frac{\partial}{\partial t}(\varrho h) + \nabla \cdot (\varrho \mathbf{U} h) - \nabla \cdot (\lambda \nabla T) = \frac{\partial}{\partial t}(p) + \nabla \cdot (\mathbf{U} p) + \mathcal{S}_\tau \quad (3.13)$$

The thermal conductivity is given by  $\lambda$ ,  $h$  corresponds to the mass specific enthalpy and  $\mathcal{S}_\tau$  refers to the dissipation function.

Using the continuity equation (3.7), the density  $\varrho$  may be extracted from the temporal and spatial derivatives for compressible and incompressible flow [TANNEHILL ET AL. 1997].

$$\varrho \frac{\partial}{\partial t}(h) + \varrho \nabla \cdot (\mathbf{U} h) - \nabla \cdot (\lambda \nabla T) = \frac{\partial}{\partial t}(p) + \nabla \cdot (\mathbf{U} p) + \mathcal{S}_\tau \quad (3.14)$$

For low viscous incompressible mediocre flow, the temporal change in pressure and the dissipation function may be neglected according to KUNKELMANN & STEPHAN 2009, as their contribution to enthalpy change is overshadowed by convection and conduction so that the enthalpy balance becomes:

$$\varrho \frac{\partial}{\partial t}(h) + \varrho \nabla \cdot (\mathbf{U} h) - \nabla \cdot (\lambda \nabla T) = 0. \quad (3.15)$$

### 3.1 Discretization

The mathematical description of fluid flow or heat transfer uses continuous fields to describe the flow field or temperature field, respectively. When approximating the continuous fields numerically, time, space and the transport equations have to be discretized. The three discretization steps are described in the following subsections.

### 3.1.1 Temporal Discretization

The temporal change of flow quantities has to be considered for transient simulations. This gradual change is approximated numerically by specifying a time interval or time step size  $\Delta t$  and computing quantity changes during this time interval. When the time interval approaches zero, the numeric solution has to approach the exact solution. Simulations may either be carried out with a constant time interval or an adaptive time interval (adaptive time-stepping). A linear temporal approximation is considered, the value of an arbitrary scalar quantity  $\xi$  can be calculated using a first order Taylor series expansion:

$$\xi(t + \Delta t) = \xi(t) + \Delta t \left. \frac{\partial \xi}{\partial t} \right|_t. \quad (3.16)$$

The linear quantity change in time leads to the error scaling in second order with the time step size. The temporal discretization is therefore said to be a second order approximation.

### 3.1.2 Volume Discretization

In order to resolve the flow quantities within space, the regarded domain is discretized into a finite number of spatial sub-entities or CVs, which make up this domain [MARIĆ ET AL. 2014, FERZIGER & PERIĆ 2002]. The conservation equations are then solved for each CV, while considering the interaction with their neighboring CVs. This leads to a numerical approximation of the actual solution of the partial differential conservation equations. As stated by MARSCHALL 2011, for consistency, the accuracy of the numerical approximation should increase with increasing number of CVs and eventually meet the exact solution as the number of CVs used for the discretization approaches infinity. The transition from a continuous flow domain to a discretized flow domain is illustrated in figure 3.2.

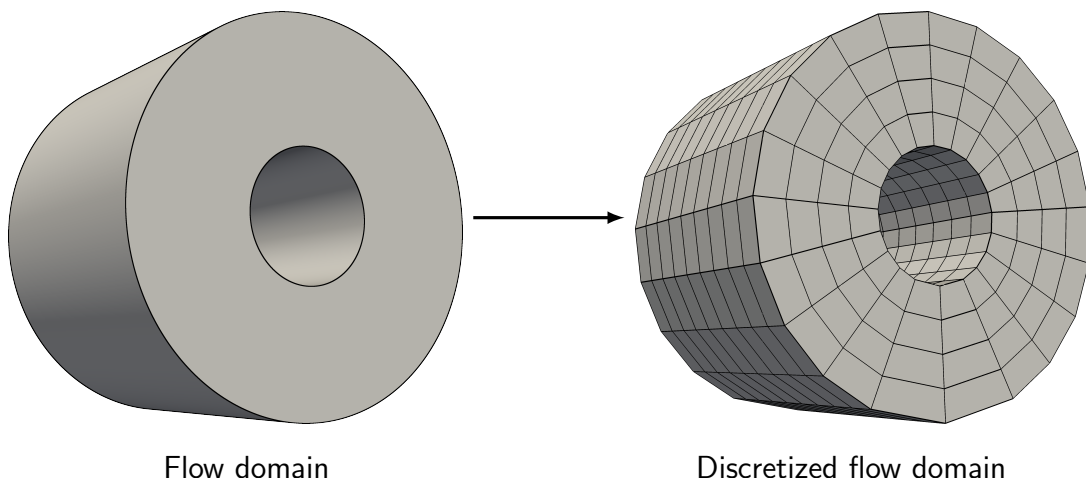


**Figure 3.2:** Transition from a continuous to a discretized flow domain.

As can be seen in figure 3.2, the discretized domain only gives an approximation of the actual flow domain. With increasing resolution of the discretization, the deviation between the actual flow domain and the discretized flow domain decreases. The boundaries of the CVs of the discretized flow domain form a mesh or grid like structure, which is why the discretized domain is also referred to as the simulation mesh or grid.

For the description of the finite volume discretization, a single CV of the discretized flow domain in figure 3.2 is focused. The computational node is assigned to the CV's volumetric center P, where mean values of the CV volume are stored. Figure 3.3 shows a CV, of volume  $V_P$  and computational node P. Additionally, the neighboring CV is shown, with the computational node N. The CV faces are always defined outwards for each CV. Hence, the shared face f between both CVs in figure 3.3 with the face vector  $\mathbf{S}_f$  is defined for P. The area  $S_f$  of face f is equal to the magnitude of the face normal vector  $\mathbf{S}_f$ .

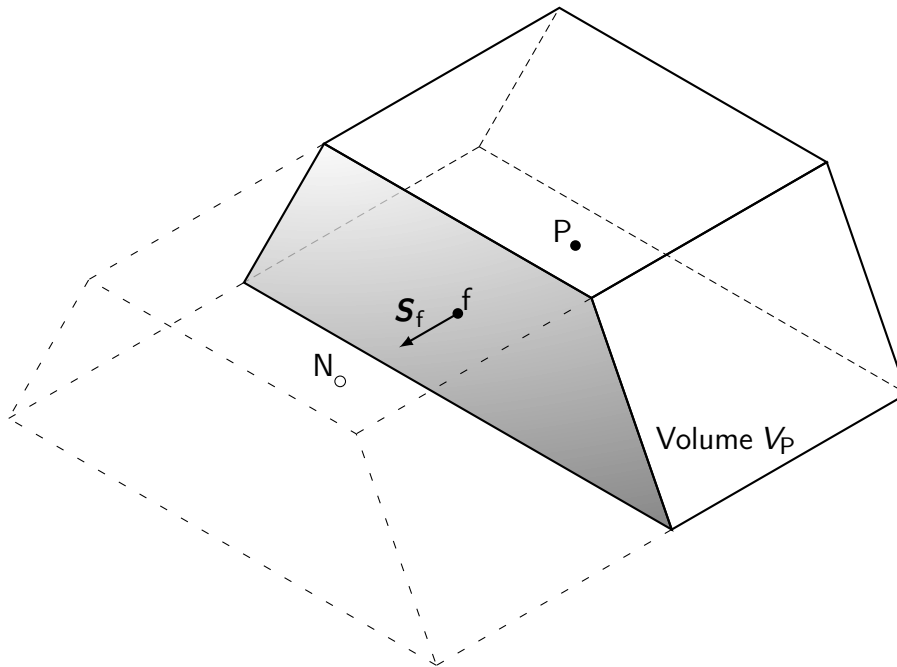


**Figure 3.3:** Depiction of a considered control volume.

Solving the transport equation (3.6) for an arbitrary scalar  $\xi$  includes the diffusive transfer of  $\xi$ , for which a second order derivative in space is required. In order to keep the accuracy during the approximation, a second or higher order for the volume discretization is required. This is achieved by presuming a linear change of  $\xi$  within the CV. The linear approximation is gained using the first order Taylor Series expansion. This expansion is given for an arbitrary scalar  $\xi$  and an arbitrary vector  $\boldsymbol{\xi}$ .

$$\xi(\mathbf{x}) = \xi_P + (\mathbf{x} - \mathbf{x}_P) \cdot \nabla \xi|_P \quad (3.17)$$

$$\boldsymbol{\xi}(\mathbf{x}) = \boldsymbol{\xi}_P + (\mathbf{x} - \mathbf{x}_P) \cdot \nabla \boldsymbol{\xi}|_P \quad (3.18)$$

Variables with the index P refer to the quantity of the computational node and the vector  $\mathbf{x}$  corresponds to the position vector pointing to an arbitrary position in the considered CV.

This assumption of a linear change of the arbitrary scalar  $\xi$  leads to the following relation for the discretized volume and surface integrals of  $\xi$  [MARSCHALL 2011]. Equation (3.21) is given in addition for an arbitrary vector  $\boldsymbol{\xi}$  according to JASAK 1996. The scalar  $\xi_f$  in equations (3.20) and (3.21) refers to the surface average value of face f.

$$\begin{aligned} \int_{V_P} \xi \, dV &= \int_{V_P} [\xi_P + (\mathbf{x} - \mathbf{x}_P) \cdot \nabla \xi|_P] \, dV \\ &= \xi_P \int_{V_P} dV + \nabla \xi|_P \cdot \int_{V_P} (\mathbf{x} - \mathbf{x}_P) \, dV = \xi_P V_P \end{aligned} \quad (3.19)$$

$$\begin{aligned} \oint_S \mathbf{n} \xi \, dS &= \sum_f \int_{S_f} \mathbf{n} \xi(\mathbf{x}) \, dS \\ &= \sum_f \int_{S_f} \mathbf{n} [\xi_f + (\mathbf{x} - \mathbf{x}_f) \cdot \nabla \xi|_f] \, dS = \sum_f \mathbf{S}_f \xi_f \end{aligned} \quad (3.20)$$

$$\begin{aligned} \oint_S \mathbf{n} \cdot \boldsymbol{\xi} \, dS &= \sum_f \int_{S_f} \mathbf{n} \cdot \boldsymbol{\xi}(\mathbf{x}) \, dS \\ &= \sum_f \int_{S_f} \mathbf{n} \cdot [\boldsymbol{\xi}_f + (\mathbf{x} - \mathbf{x}_f) \cdot \nabla \boldsymbol{\xi}|_f] \, dS = \sum_f \mathbf{S}_f \cdot \boldsymbol{\xi}_f \end{aligned} \quad (3.21)$$

### Convection

In the finite volume method, the volume integral of the convection term is first converted to a surface integral using the Gauss theorem given in equation (3.3). Afterwards, the surface integral is approximated numerically.

$$\begin{aligned} \int_{V_P} \nabla \cdot (\varrho \xi \mathbf{U}) \, dV &= \oint_S \mathbf{n} \cdot (\varrho \xi \mathbf{U}) \, dS \\ &= \sum_f \mathbf{S}_f \cdot (\varrho \xi \mathbf{U})|_f \approx \sum_f \mathbf{S}_f \cdot (\varrho \mathbf{U})|_f \xi_f \end{aligned} \quad (3.22)$$

The inner product  $\mathbf{S}_f \cdot (\varrho \mathbf{U})|_f$  corresponds to the mass flux  $\mathcal{F}_\varrho|_f$  of face f. The face values are approximated from the computation nodes using suitable differencing schemes. The schemes are described for the scalar quantity  $\xi_f$ .

Common differencing schemes are the upwind differencing (UD) and the central differencing (CD) scheme. Blended schemes are further available, which is a superposition of the upwind scheme and the differencing scheme.

- Upwind differencing scheme

The upwind differencing scheme is first order accurate in space and time, where the value of a computation node is used for the face value of the face lying in upstream flow direction of the computation node.

$$\xi_f = \begin{cases} \xi_P & \text{for } \mathcal{F}_e|_f \geq 0 \\ \xi_N & \text{for } \mathcal{F}_e|_f < 0 \end{cases} \quad (3.23)$$

The Courant number  $Co$  is used to consider the Courant–Friedrichs–Lewy condition and is defined as:

$$Co := \mathbf{U} \frac{\Delta t}{\Delta x}, \quad (3.24)$$

where  $\Delta x$  represents the characteristic length of a CV.

The upwind differencing scheme is stable for Courant numbers  $Co \leq 1$  and therefore, is considered conditionally stable. However, numerical diffusion is introduced to the solution, which lowers the accuracy as sharp gradients cannot be handled in the computational domain.

- Central differencing scheme

For the evaluation of the face value, the central differencing scheme uses a spatial linear interpolation between the computation nodes adjacent to the considered face. As a linear change of the quantities within the CV is regarded, the scheme is considered to be of second order and no discretization accuracy is lost when using this scheme. The face value is calculated according to equation (3.25).

$$\xi_f = \varepsilon \xi_P + (1 - \varepsilon) \xi_N \quad (3.25)$$

The interpolation value  $\varepsilon$  is defined as:

$$\varepsilon := \frac{|\mathbf{x}_f - \mathbf{x}_N|}{|\mathbf{x}_N - \mathbf{x}_P|} = \frac{\overline{fN}}{\overline{PN}}. \quad (3.26)$$

The central differencing scheme is unbounded and may lead to oscillations in the solution for convection dominated cases.

- Blended schemes

The idea behind blended schemes is to find a suitable function for blending the UD and CD scheme with the aim of combining the advantages of these two schemes, thus, having a stable simulation with a high simulation accuracy. The face value is calculated according to equation (3.27), where  $\mathcal{B}$  is a blending function, which is bound between  $0 \leq \mathcal{B} \leq 1$  and enables to switch between the UD and CD scheme.

$$\xi_f = \mathcal{B} \xi_{f \text{ UD}} + (1 - \mathcal{B}) \xi_{f \text{ CD}} \quad (3.27)$$

### Conduction

The conduction term is also first transformed from a volume integral to a surface integral using the Gauss theorem in equation (3.3). Afterwards, the surface integral is approximated:

$$\begin{aligned} \int_{V_P} \nabla \cdot (\lambda_\xi \nabla \xi) \, dV &= \oint_S \mathbf{n} \cdot (\lambda_\xi \nabla \xi) \, dS \\ &= \sum_f \mathbf{S}_f \cdot (\lambda_\xi \nabla \xi)|_f \approx \sum_f \lambda_{\xi f} \mathbf{S}_f \cdot \nabla \xi|_f. \end{aligned} \quad (3.28)$$

According to equation (3.28), the conduction coefficient  $\lambda_{\xi f}$  and the surface normal gradient  $\mathbf{S}_f \cdot \nabla \xi|_f$  of  $\xi$  to the face  $f$  have to be approximated. The face value of the conduction coefficient is approximated using one of the aforementioned differencing schemes. The face value of the normal gradient has to be evaluated differently. For orthogonal CVs ( $\mathbf{S}_f \parallel \mathbf{x}_N - \mathbf{x}_P$ ), the face normal gradient of  $\xi$  is given by:

$$\mathbf{S}_f \cdot \nabla \xi|_f = |\mathbf{S}_f| \frac{\xi_N - \xi_P}{|\mathbf{x}_N - \mathbf{x}_P|}. \quad (3.29)$$

The gradient in equation (3.29) is approximated in direction of the axis between the computation nodes. For an orthogonal CV, the direction of this axis aligns with the direction of the normal vector of the surface. For non-orthogonal CVs, the direction of the gradient approximation has to be corrected, in order for the gradient direction and the surface normal vector to align. The over-relaxed approach of the gradient correction for a CV is depicted in figure 3.4 according to JASAK 1996.

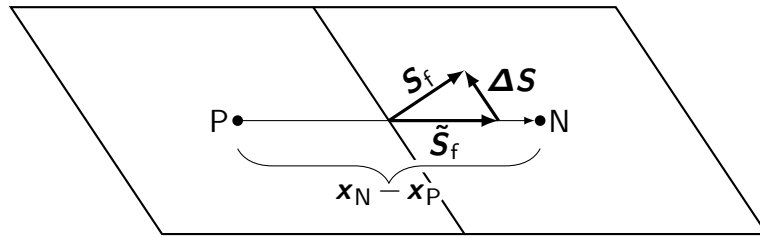


**Figure 3.4:** Non-Orthogonality correction [JASAK 1996].

The aim of the gradient correction is to calculate the portion of the surface vector  $\mathbf{S}_f$  parallel to the axis between the computation nodes  $\overline{PN}$  using the highly accurate equation (3.29). If  $\tilde{\mathbf{S}}_f$  is considered to be parallel to  $\overline{PN}$ , then a vector difference  $\Delta \mathbf{S}$  can be defined so that:

$$\mathbf{S}_f = \tilde{\mathbf{S}}_f + \Delta \mathbf{S}. \quad (3.30)$$

The surface normal gradient is then calculated by:

$$\mathbf{S}_f \cdot \nabla \xi|_f = (\tilde{\mathbf{S}}_f + \Delta \mathbf{S}) \cdot \nabla \xi|_f = \tilde{\mathbf{S}}_f \cdot \nabla \xi|_f + \Delta \mathbf{S} \cdot \nabla \xi|_f. \quad (3.31)$$

The first term on the right hand side of equation (3.31) can be evaluated using the highly accurate equation (3.29), as the vector aligns with the axis between the nodes. For the second term on the right hand side,  $\nabla\xi|_f$  may be approximated using linear interpolation of  $\nabla\xi$  of the computation nodes. The surface normal gradient thus reads:

$$\mathbf{S}_f \cdot \nabla\xi|_f = |\tilde{\mathbf{S}}_f| \frac{\xi_N - \xi_P}{|\mathbf{x}_N - \mathbf{x}_P|} + \Delta\mathbf{S} \cdot (\varepsilon \nabla\xi|_P + (1 - \varepsilon) \nabla\xi|_N). \quad (3.32)$$

The less accurate gradient evaluation is limited to the  $\Delta\mathbf{S}$  component of the surface normal vector  $\mathbf{S}_f$  instead of being used for the entire vector. According to JASAK 1996, there are different possible definitions for the vector  $\tilde{\mathbf{S}}_f$ . The vector difference  $\Delta\mathbf{S}$  is evaluated from equation (3.30). The definition of  $\tilde{\mathbf{S}}_f$  using the over-relaxed approach is given in equation (3.33). This is considered the most robust definition, as the importance of the highly accurate first term on the right hand side of equation (3.32) increases with increasing non-orthogonality [MARSCHALL 2011, JASAK 1996].

$$\tilde{\mathbf{S}}_f = \frac{(\mathbf{x}_N - \mathbf{x}_P)}{(\mathbf{x}_N - \mathbf{x}_P) \cdot \mathbf{S}_f} |\mathbf{S}_f|^2. \quad (3.33)$$

The diffusion term is bounded for orthogonal CVs. Introducing a non-orthogonal correction might lead to unboundedness, which would become larger, the higher the non-orthogonality of the CVs.

### Source term

All terms that are not temporal or describe the transport across the CV's surfaces are considered as source or sink terms, further on only referred to as source terms, regardless of whether it has a positive or negative influence on the temporal propagation of the considered quantity. The source term  $\mathcal{S}_\xi(\xi)$  may be a function of time, space and the scalar quantity  $\xi$ . According to JASAK 1996, the source term should be linearized, if possible, prior to discretization for increased stability and boundedness. In addition, it should be treated as implicitly as possible, for increased stability. A possible decomposition of  $\mathcal{S}_\xi$  for linearization is given below:

$$\mathcal{S}_\xi(\xi) = \mathcal{S}_u + \mathcal{S}_p \xi, \quad \text{where} \quad \mathcal{S}_p = \frac{\partial}{\partial \xi} [\mathcal{S}_\xi(\xi)]. \quad (3.34)$$

The term  $\mathcal{S}_u$  includes the non linear part of the source term  $\mathcal{S}_\xi$ . The source term is then discretized according to equation (3.19).

$$\int_{V_P} \mathcal{S}_\xi(\xi) \, dV = \mathcal{S}_u V_P + \mathcal{S}_p V_P \xi_P \quad (3.35)$$

### 3.1.3 Boundary control volumes

Control volumes which are located at the edge of the simulation domain need special treatment, as some of their faces are not shared with neighboring CVs and thus, can not be evaluated as mentioned in section 3.1.2. A possible boundary CV is shown in figure 3.5, where the face  $e$  is located at the edge of the simulation domain.

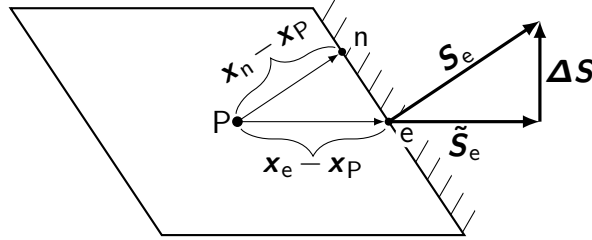


**Figure 3.5:** Definitions for boundary CV treatment.

The center of the boundary face is given by point  $e$ . The vector connecting the points  $P$  and  $n$  is normal to the boundary face  $e$ . Hence,  $(\mathbf{x}_n - \mathbf{x}_P) \parallel \mathbf{S}_e$ . The vector pointing from  $P$  to  $n$  is defined as:

$$\mathbf{x}_n - \mathbf{x}_P := \frac{\mathbf{S}_e (\mathbf{x}_e - \mathbf{x}_P) \cdot \mathbf{S}_e}{|\mathbf{S}_e| |\mathbf{S}_e|}. \quad (3.36)$$

For boundary faces  $e$ , so called boundary conditions need to be defined. These boundary conditions are formulated from the two different base types, the Dirichlet and the von Neumann boundary condition. Depending on the required properties of the boundary, the Dirichlet or von Neumann boundary condition may suffice. Otherwise a combination of these boundary conditions may be formulated.

#### Dirichlet boundary condition

For the Dirichlet boundary condition, the value  $\xi_e$  of the boundary face  $e$  is provided. The convection and conduction terms of the generic transport equation (3.1) for a boundary CV are then discretized as follows:

$$\int_{V_P} \nabla \cdot (\rho \xi \mathbf{U}) \, dV \approx \sum_f \mathcal{F}_\ell|_f \xi_f + \sum_e \mathcal{F}_\ell|_e \xi_e, \quad (3.37)$$

$$\int_{V_P} \nabla \cdot (\lambda_\xi \nabla \xi) \, dV \approx \sum_f \lambda_{\xi f} \mathbf{S}_f \cdot \nabla \xi|_f + \sum_e \lambda_{\xi e} \mathbf{S}_e \cdot \nabla \xi|_e. \quad (3.38)$$

The surface normal gradient of the boundary face is evaluated using equation (3.39). The non-orthogonality correction is given in the second term on the right hand side of equation (3.39) and is illustrated in figure 3.5.

$$\mathbf{S}_e \cdot \nabla \xi|_e = \left| \tilde{\mathbf{S}}_e \right| \frac{\xi_e - \xi_P}{|\mathbf{x}_n - \mathbf{x}_P|} + \Delta \mathbf{S} \cdot \nabla \xi|_P \quad (3.39)$$

For orthogonal CVs, the second term on the right hand side equals zero. The term  $\tilde{\mathbf{S}}_f$  is evaluated depending on the chosen non-orthogonality treatment, according to section 3.1.2. A possible definition is given in equation (3.34). It has to be noted that compared to central CVs, the non-orthogonal correction of boundary CVs uses the gradient  $\nabla\xi|_P$  evaluated at the computation node P as it can not be interpolated from a neighboring CV.

### von Neumann boundary condition

For a von Neumann boundary condition, the normal gradient  $\mathbf{S}_e \cdot \nabla\xi|_e$  is provided. The conduction term can therefore be directly discretized. For the convection term, the boundary face value  $\xi_e$  is extrapolated from the node value of the CV and the provided normal gradient. Then, the convection term is discretized using equation (3.37).

$$\xi_e = \xi_P + |\mathbf{x}_n - \mathbf{x}_P| \cdot \nabla\xi|_e \quad (3.40)$$

### 3.1.4 Temporal progression

For the temporal discretization of the generic transport equation (3.1), the Leibniz-Reynolds transport theorem, given in equation (3.2), is first used, in order to place the temporal derivative outside the volume integration. If a static CV is assumed, the following relation results for its semi-discretized form.

$$\begin{aligned} \int_t^{t+\Delta t} \left[ \int_{V_P} \frac{\partial}{\partial t} (\varrho \xi) \, dV \right] dt &= \int_t^{t+\Delta t} \frac{\partial}{\partial t} \left[ \int_{V_P} \varrho \xi \, dV \right] dt \\ &= \int_t^{t+\Delta t} \frac{\partial}{\partial t} (\varrho_P \xi_P) V_P \, dt \end{aligned} \quad (3.41)$$

The generic transport equation (3.1) in its semi-discretized form equals:

$$\begin{aligned} &\int_t^{t+\Delta t} \frac{\partial}{\partial t} (\varrho_P \xi_P) V_P \, dt = \\ &= \int_t^{t+\Delta t} \left[ - \sum_f \mathcal{F}_{\varrho|_f} \xi_f + \sum_f \lambda_{\xi f} \mathbf{S}_f \cdot \nabla\xi|_f + \mathcal{S}_u V_P + \mathcal{S}_p V_P \xi_P \right] dt. \end{aligned} \quad (3.42)$$

The derivation of discretized forms on the right hand side of equation (3.42) of the convection term, the conduction term and the source term, respectively, were described in section 3.1.2. On the left hand side of equation (3.42), the change in time of the arbitrary quantity  $\xi$  is calculated. A rearrangement of the temporal Taylor series expansion, given in equation (3.16), is used for the discretization of the derivative.

$$\int_t^{t+\Delta t} \frac{\partial}{\partial t} (\varrho_P \xi_P) V_P \, dt = \int_t^{t+\Delta t} \frac{\varrho_P^i \xi_P^i - \varrho_P^{i-1} \xi_P^{i-1}}{\Delta t} V_P \, dt \quad (3.43)$$

The time step is indicated by the superscript  $i$ . Because of the discretization of the temporal derivative in equation (3.43), the time integral consists of temporally fixed values, which stay constant within the integration across  $\Delta t$ .

On the right hand side of equation (3.42), all possible influences that inflict a change of the arbitrary quantity  $\xi$  are considered. For convenience, the terms in the integral on the right hand side of equation (3.43) are summarized as the function  $\mathcal{O}(t)$ .

$$\mathcal{O}(t) := \int_t^{t+\Delta t} \left[ - \sum_{\text{f}} \mathcal{F}_{\varrho}|_{\text{f}} \xi_{\text{f}} + \sum_{\text{f}} \lambda_{\xi\text{f}} \mathbf{S}_{\text{f}} \cdot \nabla \xi|_{\text{f}} + \mathcal{S}_{\text{u}} V_{\text{P}} + \mathcal{S}_{\text{p}} V_{\text{P}} \xi_{\text{P}} \right] dt \quad (3.44)$$

In the finite volume discretization method, it became customary to neglect changes of  $\mathcal{O}(t)$ , while integrating across  $\Delta t$ . Therefore, the function  $\mathcal{O}(t)$  is evaluated for a specific time step  $\mathcal{O}(t^i)$ . This simplification along with the discretization of the derivative leads to equations (3.43) and (3.44) integrating across fixed values. Thus, both sides of the semi-discretized transport equation (3.42) end up being multiplied with the time step size  $\Delta t$ , which may be eliminated.

Depending on the used temporal discretization method, the chosen time step for  $\mathcal{O}(t)$  differs. Typical temporal discretization methods are the Euler method, the Crank–Nicholson method or the backward differencing method. Within this work, an implicit version of the Euler discretization method is used, known as the Euler implicit method. Further information about the other temporal discretization methods is given in the dissertation of MARSCHALL 2011. The Euler implicit method is first order accurate. For the Euler implicit discretization method, the function  $\mathcal{O}(t)$  is evaluated for the new time step  $i$ .

$$\frac{\varrho_{\text{P}}^i \xi_{\text{P}}^i - \varrho_{\text{P}}^{i-1} \xi_{\text{P}}^{i-1}}{\Delta t} V_{\text{P}} = \mathcal{O}(t^i) \quad (3.45)$$

This yields to solving a system of linear algebraic equations, which is explained in section 3.1.5. However, due to the implicit setup of the equations, the system is coupled strongly and larger time step sizes are possible to compute. Furthermore, this method guarantees boundedness of the solution if the non-orthogonality is treated explicitly.

### 3.1.5 Solution method

The discretization of the transfer equation (3.1) for an arbitrary scalar  $\xi$  was shown for a single CV so far. For this CV, an algebraic relation, given in equation (3.45), was derived for the temporal change of the arbitrary quantity  $\xi$ , which depends on the values of the considered CV and the neighboring CVs. This algebraic relation is rearranged and summarized to the following form:

$$a_{\text{P}} \xi_{\text{P}} + \sum_{\text{N}} a_{\text{N}} \xi_{\text{N}} = O_{\text{P}}. \quad (3.46)$$

The values of  $a_P$ ,  $a_N$  and  $O_P$  differ depending on the nature of the regarded physical problem, the chosen differencing schemes and the chosen temporal discretization method. For example, if the central differencing scheme of equation (3.25) is considered for determining face values, the derived discretized equation (3.45) would lead to the following values of  $a_P$ ,  $a_N$  and  $O_P$  for an orthogonal CV which is not located at the boundary of the discretized domain:

$$a_P = \frac{\varrho_P^i}{\Delta t} V_P + \sum_f \mathbf{S}_f \cdot (\varrho \mathbf{U})|_f \varepsilon + \sum_f \lambda_{\xi f} \frac{|\mathbf{S}_f|}{|\mathbf{x}_N - \mathbf{x}_P|} \varepsilon - \mathcal{S}_P V_P, \quad (3.47)$$

$$a_N = \mathbf{S}_f \cdot (\varrho \mathbf{U})|_f (1 - \varepsilon) + \lambda_{\xi f} \frac{|\mathbf{S}_f|}{|\mathbf{x}_N - \mathbf{x}_P|} (1 - \varepsilon), \quad (3.48)$$

$$O_P = \frac{\varrho_P^{i-1} \xi_P^{i-1}}{\Delta t} V_P + \mathcal{S}_u V_P. \quad (3.49)$$

For the evaluation of  $a_N$ , the face index  $f$  indicates the face shared between the regarded CV with index  $P$  and its corresponding neighbor CV  $N$ . The interpolation value  $\varepsilon$  arises from the selected CD scheme for the evaluation of face values. The discretized source term of equation (3.35) is split between equations (3.47) and (3.49) due to the implicit treatment of the temporal progression.

For CVs located at the boundary of a flow domain, the discretized terms of the boundary conditions end up in  $a_P$  and  $O_P$ , similar to the discretized source term  $\mathcal{S}_\xi$ .

The following relation is gained when solving equation (3.46) for  $\xi_P^i$  implicitly:

$$a_P \xi_P^i + \sum_N a_N \xi_N^i = O_P, \quad (3.50)$$

where  $\xi_P^i$  depends on the new values  $\xi_N^i$  of the neighboring CVs. Equation (3.50) is formulated for each CV in a discretized flow domain. Hence, when solving a discretized flow domain implicitly, a system of linear algebraic equations is formed, with the number of equations being equal to the number of CVs used to discretize the flow domain. These equations may be summarized in the following form:

$$\underline{\mathcal{M}} \underline{\xi} = \underline{O}, \quad (3.51)$$

where  $\underline{\mathcal{M}}$  is a square matrix with a rank equal to the number of CVs. The coefficients  $a_P$  and  $a_N$  are diagonal and off-diagonal entries in the matrix  $\underline{\mathcal{M}}$ , respectively. Most coefficients of  $\underline{\mathcal{M}}$  are equal to zero. The underline of the other two terms in equation (3.51),  $\underline{\xi}$  and  $\underline{O}$ , represent column vectors, which hold the dependent variable and the source term for each CV, respectively.

The system of linear algebraic equations is solved using an appropriate matrix solver provided by the `OPENFOAM 2021` source code. The iterative method with the symmetric Gauss–Seidel smoother was mainly used within this work. In addition, the preconditioned conjugate gradient method was used in combination with a geometric

agglomerated algebraic multi-mesh preconditioner. The methodology of different relevant matrix solvers are thoroughly described by FERZIGER & PERIĆ 2002.

The convergence of the system increases, the larger the diagonal dominance of the matrix. A matrix is considered diagonally dominant, if the magnitude of the diagonal coefficient is larger than the sum of magnitudes of the off-diagonal coefficients for each row. This means that for each CV, the following relation needs to hold true [MARSCHALL 2011]:

$$|a_P| > \sum_N |a_N| .$$

Hence, an increase in the values of  $a_P$  leads to better convergence of the system of equations. The temporal discretization contributes to  $a_P$  in a way that a decrease in the time step leads to an increase in  $a_P$ , which results in better convergence. In addition, JASAK 1996 proposes that the implicit treatment of the linearized portion of the source term should be treated explicitly for positive  $\mathcal{S}_P$  contributions and implicitly for negative  $\mathcal{S}_P$  contributions, in order to increase the diagonal dominance of the matrix and thereby increase the convergence of the system, as positive  $\mathcal{S}_P$  contributions would decrease the magnitude of  $a_P$ .

### Flow problem

An incompressible laminar flow problem of a Newtonian fluid is described by equations (3.8) and (3.12). Thus, four equations are available for the evaluation of the pressure  $p$  and the three components of the velocity vector  $\mathbf{U}$ . However, none of the equations solve for pressure. The continuity equation (3.8) should rather be considered a constriction of the velocity field instead of an additional equation in its current form. In order to solve this conundrum, the continuity equation is transformed to a pressure solving equation. In order to do so, the system of linear algebraic equations for the momentum equation (3.12) is first written, without including the pressure gradient  $\Delta p$  in the source term.

$$a_P \mathbf{U}_P^i + \sum_N a_N \mathbf{U}_N^i = \mathbf{O}_P - \nabla p \quad (3.52)$$

Afterwards,  $\mathcal{A}$  and  $\mathcal{H}$  are defined:

$$\mathcal{A} := a_P \quad , \quad \mathcal{H} := \mathbf{O}_P - \sum_N a_N \mathbf{U}_N . \quad (3.53)$$

The value  $\mathcal{A}$  is the diagonal of to the matrix  $\underline{\mathcal{M}}$ , whereas  $\mathcal{H}$  can be thought of as a residual for the derivation of a pressure equation. With these definitions, equation (3.52) can be rewritten as:

$$\mathcal{A} \mathbf{U}_P - \mathcal{H} = -\nabla p . \quad (3.54)$$

It is important to note that the discretized form of the momentum equation has merely been rearranged, so far. Since  $\mathcal{A}$  and  $\mathcal{H}$  are predefined for every CV, the specification of  $\mathbf{U}_P$  for P is not needed and a general relation for  $\mathbf{U}$  is stated:

$$\mathbf{U} = \frac{\mathcal{H}}{\mathcal{A}} - \frac{\nabla p}{\mathcal{A}}. \quad (3.55)$$

Using the gained relation for  $\mathbf{U}$ , the continuity equation (3.8) is transformed into a pressure equation.

$$\nabla \cdot \left( \frac{1}{\mathcal{A}} \nabla p \right) = \nabla \cdot \left( \frac{\mathcal{H}}{\mathcal{A}} \right) \quad (3.56)$$

The pressure equation (3.56) is used in combination with the momentum equation (3.12) for solving an incompressible flow problem. The restriction of the velocity field, given in the continuity equation (3.8), was thus transformed into an equation which can be used for solving a flow problem. Pressure and velocity should ideally be solved simultaneously in a single system of linear algebraic equations. This however is not yet achieved. Two systems of linear algebraic equations are therefore solved separately and the coupling between velocity and pressure is handled separately. The two algorithms for pressure-velocity coupling implemented in OPENFOAM 2021 are the Pressure Implicit with Splitting of Operators algorithm (PISO) and the Semi-Implicit Method for Pressure-Linked Equations algorithm (SIMPLE) introduced by ISSA 1986 and PATANKAR 1980, respectively. The following equations (pU1) to (pU4) are solved within both pressure-velocity coupling algorithms. First, a system of linear algebraic equations is formed based on the momentum balance of equation (3.52).

$$\underline{\underline{\mathcal{M}_U}} \mathbf{U} = \underline{\underline{\mathcal{O}_U}} - \underline{\underline{\nabla p}} \quad (\text{pU1})$$

The system of linear algebraic equations is then solved for the velocity  $\mathbf{U}$ . Additionally, the diagonal of the velocity square matrix  $\underline{\underline{\mathcal{M}_U}}$  is needed for the evaluation of  $\mathcal{A}$ , when solving the pressure equation (3.56). The matrix  $\underline{\underline{\mathcal{A}}}$  containing the diagonal coefficients  $\mathcal{A}$  is extracted using the unit matrix  $\underline{\underline{\mathcal{I}}}$ . Afterwards, the vector  $\mathcal{H}$  containing the residuals is also extracted from the square matrix  $\underline{\underline{\mathcal{M}}}$ . The following definitions of  $\underline{\underline{\mathcal{A}}}$  and  $\mathcal{H}$  for a system of linear algebraic equations align with the definitions of  $\mathcal{A}$  and  $\mathcal{H}$  for an arbitrary CV of equation (3.53).

$$\underline{\underline{\mathcal{A}}} := \underline{\underline{\mathcal{M}_U}} \underline{\underline{\mathcal{I}}} \quad ; \quad \mathcal{H} := \underline{\underline{\mathcal{O}_U}} - \left( \underline{\underline{\mathcal{M}_U}} \mathbf{U} - \underline{\underline{\mathcal{A}}} \mathbf{U} \right) \quad (\text{pU2})$$

With the values of  $\underline{\underline{\mathcal{A}}}$  and  $\mathcal{H}$ , the system of linear algebraic equations (pU3) of the pressure equation (3.56) is formulated and solved for an updated pressure  $p$ .

$$\underline{\underline{\mathcal{M}_p}} p = \underline{\underline{\mathcal{O}_p}} \quad (\text{pU3})$$

A solution for pressure and velocity is now available. However, the solution of the velocity depends on the solution of the pressure from the previous iteration step,

rather than the updated pressure. Thus, the solutions of pressure and velocity do not co-align with each other so far, meaning that the solution does not satisfy the continuity equation. Therefore, the velocity is determined explicitly using the pressure  $p$ ,  $\underline{\underline{A}}$  and  $\underline{\underline{H}}$  by equation (pU4). This assures that the solution of  $p$  and  $\underline{\underline{U}}$  satisfy the continuity equation.

$$\underline{\underline{U}} = \underline{\underline{A}}^{-1} \underline{\underline{H}} - \underline{\underline{A}}^{-1} \nabla p \tag{pU4}$$

The velocity is updated with the use of an updated pressure gradient. However,  $\underline{\underline{A}}$  and  $\underline{\underline{H}}$  are still evaluated from the matrix  $\underline{\underline{M}}$  with the old pressure solution. Hence, an iteration procedure is needed, which updates these values until a specified tolerance is reached. The difference between the PISO [ISSA 1986] and SIMPLE [PATANKAR 1980] algorithms lies within the procedure of updating  $\underline{\underline{A}}$  and  $\underline{\underline{H}}$ . The two different algorithms are illustrated in figure 3.6.



## 3.2 Two-phase flow

This work focuses on the simulation of pure substance condensation. Subsequently, two-phase flow merely refers to gas-liquid flow within this work. The scale of two-phase flow may vary in a very large spatial and temporal range even within a single simulation. Different CFD methods were developed, which focus on the simulation of different length scale phenomena.

### 3.2.1 Modeling approaches

The CFD methods for two-phase flow may be categorized by the level of spatial resolution. Their categorization is given in table 3.1, which gives a brief overview of the different available CFD methods for two-phase flow, according to the dissertation of ACHER 2015.

**Table 3.1:** General modeling approaches for two-phase flows [ACHER 2015].

Model	Equations	Resolution	Applicability
Interface resolving	Interface tracking: Solve conservation equations for each phase; Interface capturing: Solve conservation equations for a mixture phase	High	Small systems; single droplet
Euler–Lagrange	Solve an equation of motion for disperse phase; Volume averaged Navier–Stokes equation for continua	Medium	Lab-scale systems
Euler–Euler	Averaged conservation equations for a mixture phase	Low	Industrial scale systems

Interface resolving methods aim to resolve every necessary aspect of the simulation. Euler methods aim to resolve macroscopic movements of the two-phase flow, while modeling sub-scale phenomena. Thus, every numeric approach is specifically tailored for the regarded hydrodynamic characteristics. A brief overview of the three simulation approaches for two-phase flow is given below according to ACHER 2015.

#### Interface resolving methods

Interface resolving methods can further be subdivided into interface tracking and interface capturing methods. Both methods resolve the shape and dynamic behavior of the interface. Hence, the approaches need the highest mesh resolution compared to

the other methods and are commonly used for segregated flows or detailed studies of a small domain of dispersed flows. Both approaches directly solve the Navier–Stokes equations using the respective properties of each phase. The difference between the methods is the treatment of the interface.

Interface tracking methods are either based on a moving mesh approach or an Eulerian base mesh with a Lagrangian interface description. For the moving mesh approach, the mesh aligns with the interface. CVs can be directly assigned to either phase and the phase boundary is defined by a set of CV surfaces. Therefore, the mesh needs to be rebuilt within every simulation step, which is computationally expensive. The other option is that the flow is described on an Eulerian mesh, while an additional dynamic surface mesh or particles are used for tracking the interface. These approaches are called front-tracking methods [KHARANGATE & MUDAWAR 2017, TORNBORG 2000]. The front-tracking method developed by UNVERDI & TRYGGVASON 1992 employs the Volume-of-Fluid (VOF) method for the two-phase flow, but utilizes an additional finer marker mesh for the interface.

Interface capturing methods use an Eulerian approach for the description of the two-phase flow. Popular approaches are the VOF method or the Level-Set method, introduced by HIRT & NICHOLS 1981 and SUSSMAN ET AL. 1994, respectively. Both methods calculate the properties of a mixture phase, for which the Navier–Stokes equations are solved. Furthermore, an additional function is defined in both methods, to indicate the two phases. The VOF method uses the volumetric phase fraction  $\gamma$  as its indication function. The interface is located where the phase fraction  $\gamma = 0.5$ . The distance to the interface is defined as the indicator function in the Level-Set method. This function has positive values in one phase and negative values in the other phase. The interphase is located where the indicator function reaches a value of zero.

Interface resolving methods may be used for rigorous formulations of heat and mass transfer across the interface. Hence, these methods may be used for detailed studies on heat and mass transfer coefficients. A detailed review article about the different available interface resolving methods was published by KHARANGATE & MUDAWAR 2017. The VOF method is applied in this work and is described in detail in section 3.2.2.

### **Euler–Lagrange method**

The Euler–Lagrange method is only suitable for dispersed two-phase flows. The overall flow of the continuous phase is described with an Eulerian approach, while the movement of the dispersed phase is described with a Lagrangian approach, using individual particles. The crucial part of this approach is the coupling of the interphase. Multiple models have been developed, dealing with an adequate representation of particle shape and size distributions. Nonetheless, computational costs prevent an adequate description of two-phase flow in industrial-scale apparatuses.

Coupling between the two phases may also vary, depending on the problem at hand. One-way coupling does not consider the influence of the disperse phase on the continuous

phase, meaning that the continuous phase is treated as a single-phase flow and the disperse phase is advected using the velocity of the continuous phase. Two-way coupling includes the influence of the disperse phase on the continuous phase. The presence and motion of the disperse phase is therefore considered when solving the Navier–Stokes equations for the continuous phase. For a completely accurate description of the two-phase flow, four-way coupling would be necessary, which is computationally expensive. Four-way coupling also considers the interaction between the particles of the disperse phase. The volume fraction of the disperse phase might be used as a rough indicator for the needed extend of coupling of the Euler–Lagrange method. The higher the disperse volume fraction, the more detailed the coupling has to be. One-way coupling might be used up to a volume fraction of  $10^{-6}$ , for higher volume fractions, two-way coupling should be used. Four way coupling would be needed for volume fractions of about  $10^{-3}$  and higher [ACHER 2015].

### Euler–Euler method

The Euler–Euler method considers both phases as miscible continua, without an interface between them. The simulation provides local proportions of the phase volume fraction. The interactions between the two phases, i.e. drag forces, are not resolved, but are rather considered by models and assumptions. With this model approach, it is possible to simulate multi-phase flow of industrial scale applications as the spatial resolution may be set larger, since only macroscopic movements of the two phases need to be resolved [ACHER 2015].

A set of governing equations is solved for each phase. These governing equations can be derived by different averaging techniques, i.e. conditional volume averaging [MARSCHALL 2011]. According to ACHER 2015, flow phenomena which are not resolved are considered by respective models. Momentum, heat and mass transfer rely on appropriate model formulations, which may be analytical, numerical or empirical. Hence, a rigorous determination of heat and mass transfer coefficients is not possible with this method.

### 3.2.2 Volume-of-Fluid method

The VOF method was first proposed by HIRT & NICHOLS 1981. MARSCHALL 2011 shows that it is also possible to derive the VOF method using conditional volume averaging, which is generally used for Euler–Euler methods. The key assumption of this derivation is that the relative velocity between the vapor and condensate phase within a CV equals zero. This is the case for well resolved interfaces and is the reason, why the VOF method requires a high mesh resolution.

The original formulation of HIRT & NICHOLS 1981 of the VOF method is shown in this work. The description of the VOF method in this thesis considers a condensate phase and a vapor phase, which are at equilibrium conditions, so that no transfer across

the interphase is considered at first. In order to keep track of the phases during the description of two-phase flow the index  $c$  indicates the condensate phase and  $v$  the vapor phase. Variables without an index refer to the variable of the mixture phase of a CV.

The volumetric phase fraction  $\gamma$  is introduced in the VOF method for two-phase handling.

$$\gamma = \frac{V_c}{V} \quad \gamma \in [0, 1] \quad (3.57)$$

In this thesis, the phase fraction  $\gamma$  is defined from the condensate phase and is calculated from the fraction between the volume  $V_c$  occupied by the condensate phase in a CV and the volume  $V$  of the CV itself. The values of  $\gamma$  are, therefore, bound between 0 and 1. CVs which are completely filled with condensate have a value of  $\gamma = 1$  and CVs which are completely filled with vapor have a value of  $\gamma = 0$ . CVs containing the interface have values between  $0 < \gamma < 1$ . Because of the boundedness of the interface, the VOF method is inherently conservative [KHARANGATE & MUDAWAR 2017].

The phase indication of the VOF method is given in figure 3.7, which shows a condensate droplet on a static 2D mesh. The actual droplet size and phase boundary is given on the left side and the VOF phase indication is given on the right side.

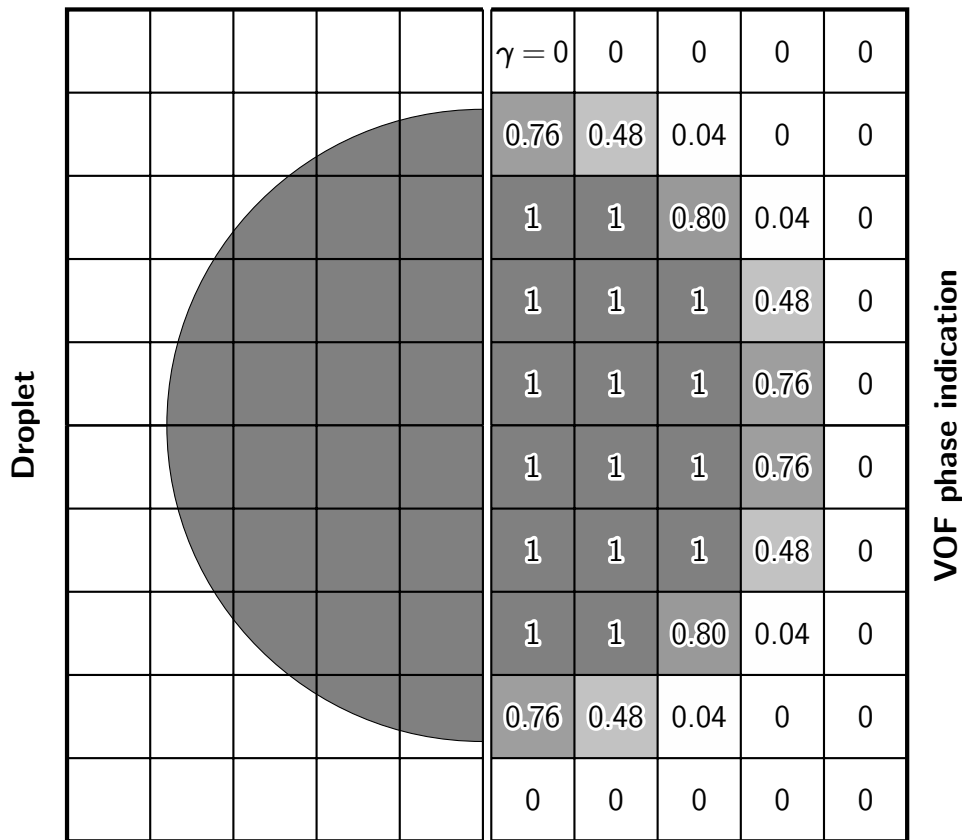


**Figure 3.7:** Phase indication of the VOF method.

In the VOF method, the material properties  $\Omega$  of each CV are calculated for the mixture phase of a CV using a phase average. A volume average is used for the dynamic viscosity  $\eta$ , density  $\varrho$ , specific heat capacity  $c_p$  at constant pressure and thermal conductivity  $\lambda$ :

$$\Omega = \gamma \Omega_c + (1 - \gamma) \Omega_v \quad \Omega \in [\eta, \varrho, c_p, \lambda]. \quad (3.58)$$

RATTNER & GARIMELLA 2014 use a mass average heat capacity  $c_p$ , which is also quite common.

The surface tension  $\sigma$  and the specific latent heat of evaporation  $\Gamma$  are considered constant throughout the simulation domain. The transport equations are calculated for the mixture phase of a CV with the introduced material properties  $\Omega$ . For an incompressible two-phase flow, the continuity equation (3.8) is used.

$$\nabla \cdot (\mathbf{U}) = 0$$

A single momentum equation is solved for the mixture phase [RATTNER & GARIMELLA 2018]. The momentum equation (3.12) is transformed using the modified pressure

$$p_{rgh} = p - \varrho \mathbf{g} \cdot \mathbf{x}, \quad (3.59)$$

according to BERBEROVIĆ 2009, for calculating the pressure gradient. Here,  $\mathbf{g}$  is the gravitational acceleration and  $\mathbf{x}$  the position vector pointing at the CV's center. With the use of the modified pressure  $p_{rgh}$ , the pressure gradient and the gravity terms are expressed by the first two terms on the right hand side of the momentum equation [MÁRQUEZ 2013] for two-phase flow.

$$\frac{\partial}{\partial t} (\varrho \mathbf{U}) + \nabla \cdot (\varrho \mathbf{U} \mathbf{U}) - \nabla \cdot [\eta (\nabla \mathbf{U} + [\nabla \mathbf{U}]^T)] = -\nabla p_{rgh} - \mathbf{g} \cdot \mathbf{x} \nabla \varrho + \mathbf{f}_\sigma \quad (3.60)$$

Additionally, surface tension forces are considered by the source term  $\mathbf{f}_\sigma$ , which can be evaluated using the Continuum Surface Force (CSF) model of BRACKBILL ET AL. 1992:

$$\mathbf{f}_\sigma = \sigma \nabla \cdot \left( \frac{\nabla \gamma}{|\nabla \gamma|} \right) \nabla \gamma. \quad (3.61)$$

According to KHARANGATE & MUDAWAR 2017, another promising approach for considering surface tension is the Continuum Surface Stress model of LAFAURIE ET AL. 1994.

The volumetric phase fraction  $\gamma$  also needs to be advected. Therefore, an additional transport equation is solved. Different approaches for the translation of the phase fraction are available in combination with the VOF method. These approaches can be categorized as methods that either use phase reconstruction or do not use phase reconstruction, respectively.

### Transport of the volume fraction with phase reconstruction

Phase reconstruction approaches consider a sharp interface of zero thickness. For the advection of the volumetric phase fraction, a step function  $w(\boldsymbol{x})$  for the phase differentiation is used.

$$w(\boldsymbol{x}) = \begin{cases} 1 & \text{for condensate} \\ 0 & \text{for vapor} \end{cases} \quad (3.62)$$

This step function  $w(\boldsymbol{x})$  is introduced in order to distinguish between the methods with and without phase reconstruction. For methods with phase reconstruction, the interphase is translated directly. This is done by advecting the step function  $w(\boldsymbol{x})$ , which is considered to be locally resolved [KHARANGATE & MUDAWAR 2017].

$$\frac{\partial}{\partial t}(w) + \boldsymbol{U} \nabla \cdot (w) = 0 \quad (3.63)$$

The step function  $w(\boldsymbol{x})$  is translated into the volumetric phase fraction according to KHARANGATE & MUDAWAR 2017:

$$\gamma = \frac{1}{V_P} \int_{V_P} w(\boldsymbol{x}) \, dV. \quad (3.64)$$

In order to be able to directly advect the interphase, it has to be reconstructed from the  $\gamma$  field. Popular schemes for phase reconstruction are the simple line interface calculation (SLIC) and the piecewise linear interface calculation (PLIC), introduced by NOH & WOODWARD 1976 and YOUNG 1982, respectively. The resulting reconstructed phases of the two schemes are depicted in figure 3.8, where a droplet is split into four different quarters, in which the interface is given for different methods. The results of the two phase reconstruction schemes are shown in the bottom quarters of the droplet. The condensate phase is depicted in gray and the vapor phase in white. Hence, for the SLIC and PLIC methods, the region where the step function  $w = 1$  is depicted in gray and  $w = 0$  in white.

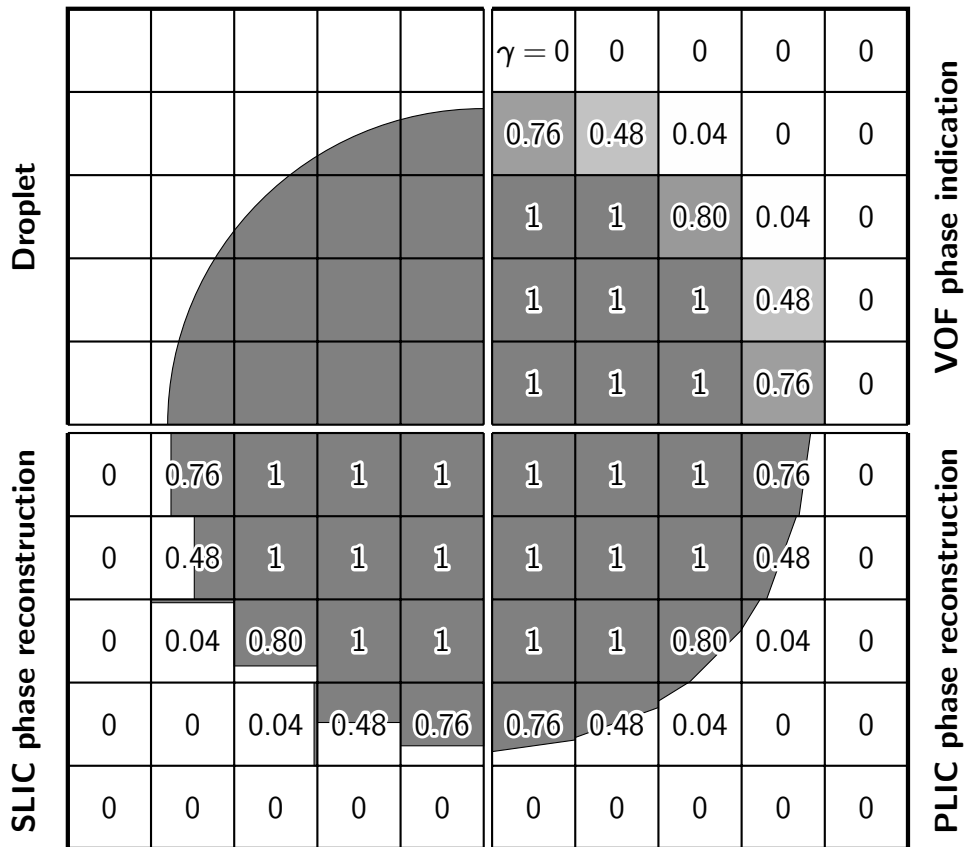


**Figure 3.8:** Phase indication of the VOF method with and without phase reconstruction.

The SLIC scheme reconstructs the phase interface along an axis of the coordinate system. The location of the interface is set according to the volume fraction of the CV. The PLIC scheme reconstructs the phase interface with a plane. The orientation of the normal vector of the plane is gained by querying the phase fractions of the neighboring CVs. After having evaluated the orientation of the plane, it is placed inside the CV according to the phase fraction of the CV [KHARANGATE & MUDAWAR 2017]. The main issue of the PLIC interface reconstruction is the discontinuities of the reconstructed phase interface. Adaptions of the PLIC scheme have been suggested, which aim to solving this issue by parting from the planar formulation of the reconstructed phase interface in a CV [GINZBURG & WITTUM 2001, PRICE 2000].

ROENBY ET AL. 2016 published an algorithm for the advection of the volume fraction using the phase reconstruction scheme called isoAdvect, which is available as an OpenFOAM extension and shows promising results.

### Transport of the volume fraction without phase reconstruction

The exact location of the phase interphase is not known when using a VOF approach. Instead, the interphase is smeared across several CVs. Its location may be approximated to where the interpolated value of the phase fraction equals  $\gamma = 0.5$  or by reconstructing

the phases. This VOF approach directly advects the volumetric phase fraction  $\gamma$  according to the following equation:

$$\frac{\partial}{\partial t} (\gamma) + \nabla \cdot (\gamma \mathbf{U}) = 0. \quad (3.65)$$

The main issue that arises for the direct advection is that on the one hand numerical diffusion of the phase fraction field is induced when using a low order convection scheme for the flux, due to the interpolation of CV face values, when solving equation (3.65). On the other hand, a high order scheme would lead to oscillations at the interface, since these schemes do not ensure boundedness. This issue becomes particularly relevant in the VOF method since large gradients are present in the phase fraction field across the interface. Therefore, appropriate convection schemes have to be used. Popular schemes are the Compressive Interface Capturing Scheme for Arbitrary Meshes (CICSAM) or the High Resolution Interface Capturing (HRIC) scheme, introduced by UBBINK & ISSA 1999 and MUZAFERIJA ET AL. 1998, respectively.

WELLER 2002 suggests that the phase fraction is transported with an adjusted velocity field  $\mathbf{U}^*$ , which includes a compression term that is only applied at the interface, counteracting numerical diffusion and thereby ensuring a steep gradient of the phase fraction field across the interface.

$$\frac{\partial}{\partial t} (\gamma) + \nabla \cdot (\gamma \mathbf{U}^*) = 0 \quad (3.66)$$

OpenFOAM uses the Multidimensional Universal Limiter for Explicit Solution (MULES) algorithm, for solving equation (3.65), which is the OpenFOAM implementation of the flux-corrected transport (FCT) theory by BORIS & BOOK 1973 and is thoroughly described in the dissertation of MÁRQUEZ 2013. The MULES algorithm replaced the VOF simulation approach using the CICSAM scheme in OPENFOAM 2021 source code because of a better performance. The algorithm includes an interface compression term with a limitation on the face fluxes, to achieve a higher order solution with a sharp interface and minimized oscillations in the solution.

### Principle of MULES algorithm

The MULES algorithm is summarized according to the description of MÁRQUEZ 2013. The advection of an arbitrary quantity  $\xi$  is first considered.

$$\frac{\partial}{\partial t} (\xi) + \nabla \cdot (\xi \mathbf{U}) = 0$$

The discretized problem is considered with an explicit temporal scheme, where  $\mathcal{F}_\xi = \mathbf{S}_f \cdot (\xi \mathbf{U})|_f$  represents the flux of the volumetric phase fraction.

$$\frac{\xi^i - \xi^{i-1}}{\Delta t} V_P + \sum_f \mathcal{F}_\xi^{i-1}|_f = 0 \quad (3.67)$$

For simplicity, a 1D flux transport through rectangular CVs is further considered, as given in figure 3.9, for the description of the MULES algorithm. The faces highlighted in gray are the faces through which a flux  $\mathcal{F}_\xi$  is transported.

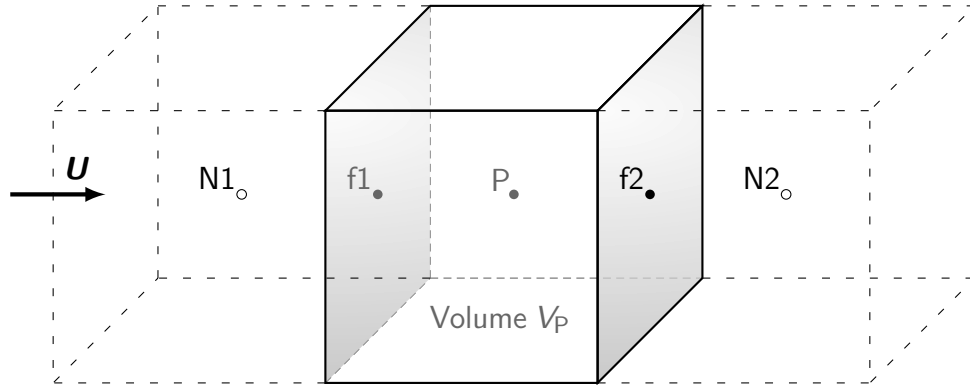


**Figure 3.9:** Considered 1D case for the description of the MULES algorithm.

The volumetric phase fraction for the time step  $i$  may be calculated by:

$$\xi^i = \xi^{i-1} + \frac{\Delta t}{V_P} \left( \mathcal{F}_\xi^{i-1} \Big|_{f1} - \mathcal{F}_\xi^{i-1} \Big|_{f2} \right). \quad (3.68)$$

The aim is to find appropriate fluxes  $\mathcal{F}_\xi^{i-1}$  to ensure a bounded solution with a sharp interface and minimized oscillations. The indication of the old time step  $i - 1$  is further on neglected for the evaluated fluxes:  $\mathcal{F}_\xi^{i-1} \rightarrow \mathcal{F}_\xi$ .

The fluxes may be computed using different convection schemes. High order schemes may lead to unbounded solutions, while low order schemes lead to numerical diffusion. The MULES algorithm finds a corrected flux  $\mathcal{F}^C$  which is still bounded and minimizes numerical diffusion. For this, the face fluxes  $\mathcal{F}_\xi^L$  and  $\mathcal{F}_\xi^H$  are evaluated using a low and a high order scheme, respectively. Afterwards, the anti-diffusive flux  $\mathcal{D}$  is evaluated.

$$\mathcal{D} := \mathcal{F}_\xi^H - \mathcal{F}_\xi^L \quad (3.69)$$

The anti-diffusive flux quantifies the difference between the convection schemes due to discretization, including the difference in numerical diffusion. The corrected flux  $\mathcal{F}_\xi^C$  is calculated by:

$$\mathcal{F}_\xi^C := \mathcal{F}_\xi^L + \kappa \mathcal{D} \quad \kappa \in [0, 1]. \quad (3.70)$$

The variable  $\kappa$  is called the weighing factor and can be thought of as an interpolation variable between the flux of a higher and lower order scheme. Thus, depending on the set value of  $\kappa$ , the order of the convection scheme may be changed. With increasing  $\kappa$ , the order of the convection scheme increases. In the MULES algorithm, the corrected

flux is used for the convection term of the volumetric phase fraction, while the weighing factor is determined for each CV face.

$$\xi^i = \xi^{i-1} + \frac{\Delta t}{V_P} \left( \mathcal{F}_\xi^C \Big|_{f1} - \mathcal{F}_\xi^C \Big|_{f2} \right) \quad (3.71)$$

The evaluation of the weighing factor  $\kappa_f$  of each CV face is similar to the approach of ZALESK 1979. The only two differences between the method of ZALESK 1979 and the MULES algorithm are that it is possible to define a global maximum and minimum value of  $\xi$  in the MULES algorithm and that an iterative evaluation of the weighing factors is used. The weighing factors are determined solely using the values of the old time step  $i - 1$ . The indication of said time step is further omitted in the description of the evaluation of the weighing factors.

The following 1D case is considered for the evaluation of the weighing factors  $\kappa_f$  of the faces.

The local extrema for the old time step  $i - 1$  are found. This is done by using the  $\min()$  and  $\max()$  functions, which give the minimum and maximum value of the arguments provided in the parentheses.

$$\min(\xi_1, \xi_2) = \begin{cases} \xi_1 & \text{for } \xi_1 < \xi_2 \\ \xi_2 & \text{for } \xi_2 < \xi_1 \end{cases} \quad (3.72)$$

$$\max(\xi_1, \xi_2) = \begin{cases} \xi_1 & \text{for } \xi_1 > \xi_2 \\ \xi_2 & \text{for } \xi_2 > \xi_1 \end{cases} \quad (3.73)$$

The local extrema  $\xi_P^{L\min}$  and  $\xi_P^{L\max}$  of P and its neighbors N for the considered case are evaluated by:

$$\xi_P^{L\min} = \min(\xi_P, \{\xi_N\}) = \min(\xi_P, \xi_{N1}, \xi_{N2}) , \quad (3.74)$$

$$\xi_P^{L\max} = \max(\xi_P, \{\xi_N\}) = \max(\xi_P, \xi_{N1}, \xi_{N2}) . \quad (3.75)$$

Afterwards, the local extrema are limited by the globally defined extrema in order to find the extrema  $\xi_P^{\min}$  and  $\xi_P^{\max}$  for P:

$$\xi_P^{\min} = \min(\xi_P^{G\max}, \xi_P^{L\max}) , \quad (3.76)$$

$$\xi_P^{\max} = \max(\xi_P^{G\min}, \xi_P^{L\min}) . \quad (3.77)$$

The aim is to limit the fluxes of P, in order to avoid new extrema. This is done by tuning the weighing factors  $\kappa_f$  of each face. It is essential to achieve boundedness in positive and negative direction of the CV's value. Face weighing factors  $\kappa_f$  for the corrected fluxes are calculated iteratively by solving equations (3.78) to (3.80) for three iteration cycles  $k$  [MÁRQUEZ 2013]. First, two weighing factors for each CV are calculated from the face weighing factors  $\kappa_f^{k-1}$  of the old iteration step. The boundedness between  $\xi_P^{\max}$  and  $\xi_P^{\min}$  is checked separately, which is indicated with the superscripts “+“ and “-“,

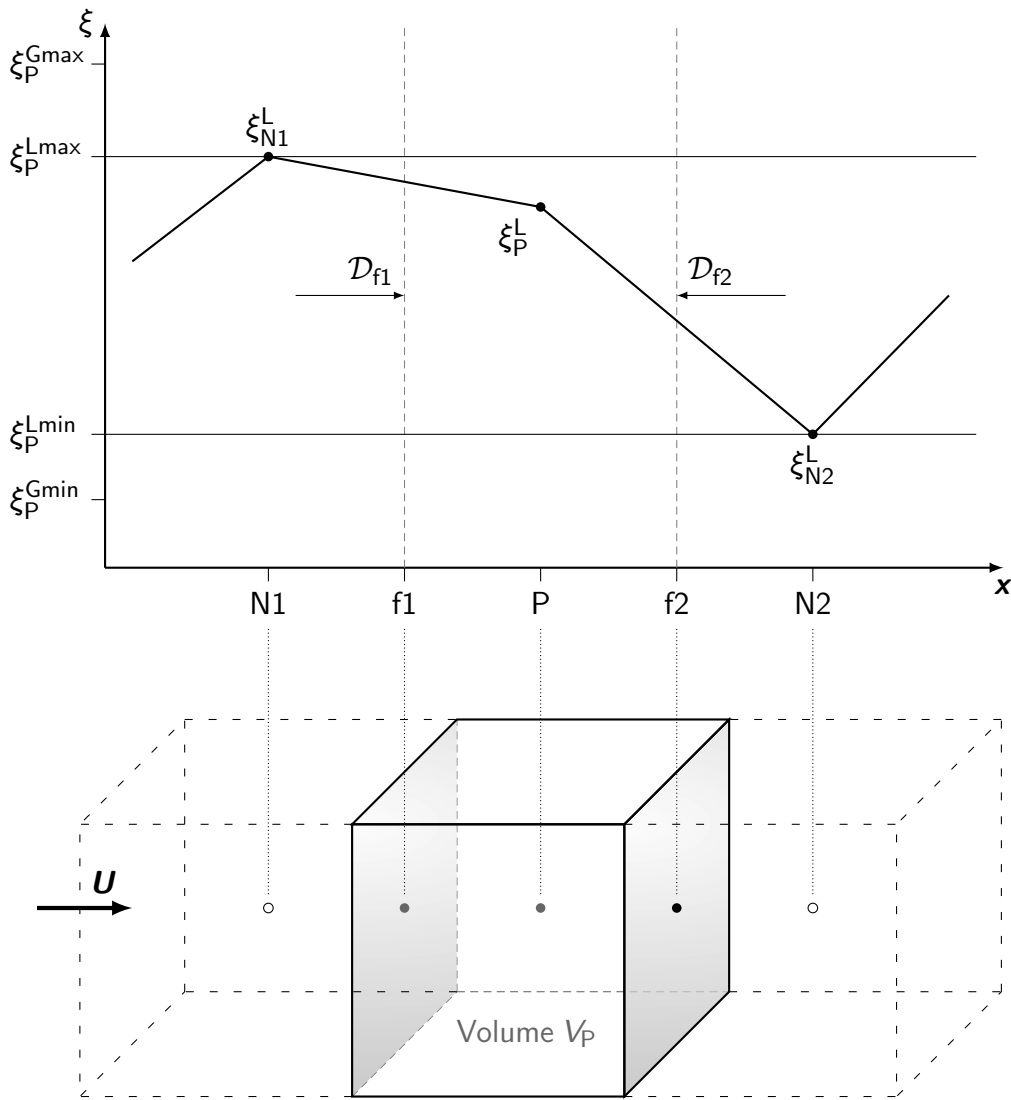


**Figure 3.10:** Schematic for the determination of the weighing factors in the MULES algorithm.

respectively. The anti-diffusive inflow and outflow are indicated with  $\mathcal{D}_f^-$  and  $\mathcal{D}_f^+$ , respectively.

$$\kappa_P^-|^k = \max \left[ \min \left( \frac{(\xi_P - \xi_P^{\min}) \frac{V}{\Delta t} - \sum_f (\mathcal{F}_\xi^L|_f + \kappa_f^{k-1} \mathcal{D}_f^+)}{\sum_f \mathcal{D}_f^-}, 1 \right), 0 \right] \quad (3.78)$$

$$\kappa_P^+|^k = \max \left[ \min \left( \frac{(\xi_P^{\max} - \xi_P) \frac{V}{\Delta t} - \sum_f (\mathcal{F}_\xi^L|_f + \kappa_f^{k-1} \mathcal{D}_f^-)}{\sum_f \mathcal{D}_f^+}, 1 \right), 0 \right] \quad (3.79)$$

Afterwards, the CV weighing factors are designed to the faces according to equation (3.80), depending on the contribution of the anti-diffusive flux  $\mathcal{D}_f$  to P. For

example, if  $\mathcal{D}_f$  is a positive contribution to P, then it is simultaneously a negative contribution to N. Therefore, it must be bounded by the maximum possible value  $\xi_P^{\max}$  of P and the minimum possible value  $\xi_N^{\min}$  of N. The CV weighing factors are assigned accordingly, meaning that the smaller value between  $\kappa_P^+$  and  $\kappa_N^-$  is chosen for a positive contribution of  $\mathcal{D}_f$  to P.

$$\kappa_f^k = \begin{cases} \min\left(\kappa_P^+|^k, \kappa_N^-|^k\right) & \text{for } \mathcal{D}_f \geq 0 \\ \min\left(\kappa_P^-|^k, \kappa_N^+|^k\right) & \text{for } \mathcal{D}_f < 0 \end{cases} \quad (3.80)$$

The corrected fluxes  $\mathcal{F}_\xi^C$  are determined and equation (3.71) is solved after the iteration of the face weighing factors.

### MULES algorithm in the VOF method of OpenFOAM

The VOF method of OpenFOAM uses equation (3.66) for the advection of the phase fraction. The exact formulation is given below [MÁRQUEZ 2013]:

$$\frac{\partial}{\partial t}(\gamma) + \nabla \cdot (\gamma \mathbf{U}) + \nabla \cdot (\gamma [1 - \gamma] \mathbf{U}_{\text{comp}}) = 0, \quad (3.81)$$

where the velocity  $\mathbf{U}_{\text{comp}}$  corresponds to an interface compression velocity, which is constricted to the interface by multiplying  $\gamma(1 - \gamma)$ .

Equation (3.81) looks very similar to a single-field transport equation for the phase fraction for two-phase flow derived using conditional volume averaging [MARSCHALL 2011, MÁRQUEZ 2013]. These two equations, however, differ greatly, since the equation derived from conditional volume averaging uses the relative velocity between the two phases, which is assumed to be equal to zero for the VOF method and consequently narrows down to equation (3.65). The interface compression velocity  $\mathbf{U}_{\text{comp}}$  on the other hand is an artificial velocity used for counteracting numerical diffusion. Thus, equation (3.81) may be thought of as an approach for solving equation (3.65) for sharp interfaces.

The discretized form of equation (3.81) for an explicit temporal scheme is implemented:

$$\frac{\gamma^i - \gamma^{i-1}}{\Delta t} V_P = \sum_f \mathbf{S}_f \cdot (\gamma^{i-1} \mathbf{U})|_f + \sum_f \mathbf{S}_f \cdot (\gamma^{i-1} [1 - \gamma^{i-1}] \mathbf{U}_{\text{comp}})|_f = 0. \quad (3.82)$$

This equation may also be written in terms of fluxes:

$$\frac{\gamma^i - \gamma^{i-1}}{\Delta t} V_P = \sum_f \gamma_f^{i-1} \mathcal{F}|_f + \sum_f (\gamma^{i-1} [1 - \gamma^{i-1}])|_f \mathcal{F}_{\text{comp}}|_f = 0, \quad (3.83)$$

where  $\mathcal{F}|_f = \mathbf{S}_f \cdot \mathbf{U}_f$  and  $\mathcal{F}_{\text{comp}}|_f = \mathbf{S}_f \cdot \mathbf{U}_{\text{comp}}|_f$ .

The face value of the phase fraction  $\gamma_f$  is determined using a blended scheme, as described in section 3.1.2, where the blending factor  $\mathcal{B}$  equals:

$$\mathcal{B} = \max\left[(1 - 4\gamma_P [1 - \gamma_P])^2, (1 - 4\gamma_N [1 - \gamma_N])^2\right]. \quad (3.84)$$

The flux  $\mathcal{F}_{\text{comp}}|_f$  of the compression velocity is calculated by:

$$\mathcal{F}_{\text{comp}}|_f = C_{\text{comp}} \frac{\mathcal{F}|_f}{|\mathbf{S}_f|} \left( \frac{\nabla\gamma}{|\nabla\gamma| + 10^{-8} V^{-1/3}} \cdot \mathbf{S}_f \right). \quad (3.85)$$

The magnitude of the interface compression velocity can be adjusted by the user defined variable  $C_{\text{comp}}$ . The direction of the interface is determined from the term inside the parentheses on the right hand side of equation (3.85). This term is also known as the face unit normal flux. The term  $10^{-8} V^{-1/3}$  is a numerical stabilization for low gradients of the phase fraction. The discretization scheme used for interface compression has no major impact on the simulation results. Nonetheless, OpenFOAM provides the *interfaceCompression* scheme, which has been specifically designed for this term.

The discretization scheme of the general convection term of equation (3.82) on the other hand is rather crucial. A slightly modified version of the MULES algorithm is used for this term. The local minima and maxima are neglected and only the globally defined extrema are used for the flux-corrected transport. This simplification is used, since the phase fraction is bound between 0 and 1 and generally does not generate new extrema [MÁRQUEZ 2013].

### 3.3 Phase change in the Volume-of-Fluid method

Parts of this section have been published in a similar way in:

Kleiner, T.; Rehfeldt, S.; Klein, H.: *CFD model and simulation of pure substance condensation on horizontal tubes using the volume of fluid method*. International Journal of Heat and Mass Transfer 138 (2019) 420-431. DOI: [10.1016/j.ijheatmasstransfer.2019.04.054](https://doi.org/10.1016/j.ijheatmasstransfer.2019.04.054).

The implemented phase change methods slightly differ depending on the used two-phase model approach used. As this work focuses on the VOF method without phase reconstruction, simulation of phase change will solemnly be described for this method. The presented models, however, may also be transferred to other two-phase modeling approaches. In general, phase change methods bring additional complications to the simulation of two-phase flow, since the interface topology tends to be less stable and mass, momentum and heat transfer across the interface has to be accounted for correctly [KHARANGATE & MUDAWAR 2017].

The exact form of the transport equations, which are solved for phase change simulations, slightly differ in literature. A set of possible transport equations is given below:

$$\frac{\partial}{\partial t}(\varrho) + \nabla \cdot (\varrho \mathbf{U}) = 0 \quad \text{or} \quad \nabla \cdot (\mathbf{U}) = \mathcal{S}_V, \quad (3.86)$$

$$\frac{\partial}{\partial t}(\varrho \mathbf{U}) + \nabla \cdot (\varrho \mathbf{U} \mathbf{U}) - \nabla \cdot [\eta (\nabla \mathbf{U} + [\nabla \mathbf{U}]^T)] = -\nabla p_{rgh} - \mathbf{g} \cdot \mathbf{x} \nabla \varrho + \mathbf{f}_\sigma, \quad (3.87)$$

$$\frac{\partial}{\partial t}(\gamma) + \nabla \cdot (\gamma \mathbf{U}) = \mathcal{S}_\gamma. \quad (3.88)$$

The source term  $\mathcal{S}_V$  in equation (3.86) accounts for the change in specific volume during phase change, while the source term  $\mathcal{S}_\gamma$  in equation (3.88) accounts for the change in condensate phase due to phase change. The source term  $\mathcal{S}_V$  is not always considered during simulations [FANG ET AL. 2010]. These source terms  $\mathcal{S}_V$  and  $\mathcal{S}_\gamma$  are shown later in the manuscript in equations (3.91) and (3.90), respectively. No additional source term is needed in the momentum equation (3.87), when having a single-field formulation [KHARANGATE & MUDAWAR 2017].

Additionally, an energy or enthalpy balance needs to be solved. Different possible forms of the enthalpy balance are given at the beginning of chapter 3. The enthalpy balance in equation (3.15) is used, while the density  $\varrho$  is often not extracted from the temporal

and convection term, since in two-phase flow, the volume-averaged density of the two fluids changes across the interface and in time, caused by phase change.

$$\frac{\partial}{\partial t}(\varrho h) + \nabla \cdot (\varrho \mathbf{U} h) - \nabla \cdot (\lambda \nabla T) = \mathcal{S}_q \quad (3.89)$$

The source term  $\mathcal{S}_q$  considers heat loss/release due to the latent heat of evaporation. All necessary source terms  $\mathcal{S}_V$ ,  $\mathcal{S}_\gamma$  and  $\mathcal{S}_q$  depend on the rate of phase change and stand in the following relations towards each other:

$$\mathcal{S}_\gamma = \frac{\mathcal{S}_q}{\Gamma} \frac{1}{\varrho_c}, \quad (3.90)$$

$$\mathcal{S}_V = \frac{\mathcal{S}_q}{\Gamma} \left( \frac{1}{\varrho_c} - \frac{1}{\varrho_v} \right). \quad (3.91)$$

Heat transfer simulations with phase change have a highly coupled behavior between the transport equations. In order for the system to be solved, an additional relation for one of the source terms has to be provided. This is where phase change methods are introduced.

The phase change methods generally use the relation between the source terms. The approach of SON & DHIR 1998 slightly differs, as they directly set the interface temperature to saturation conditions when solving the energy equation, to ensure the correct energy transport across the interface and include the rate of phase change as source terms.

Different approaches to calculate the rate of phase change in two-phase simulations are found in literature. Said rate is calculated from a heat flux balance across the interface (heat flux balance) [SZIJÁRTÓ 2015, GANAPATHY ET AL. 2013] or it is accounted for according to SZIJÁRTÓ ET AL. 2017 by comparing CV temperatures to the respective saturation temperature and including a source term to ensure saturation conditions at the interface (numerical iteration techniques). The Schrage model [SCHRAGE 1953] considers the kinetic theory of gases and is converted into a numerical iteration technique.

### 3.3.1 Heat flux balance

Heat flux balance approaches consider the Rankine-Hugoniot jump condition across the interface [KHARANGATE & MUDAWAR 2017] and determine a mass flux  $\dot{m}_{\text{int}}$  due to phase change.

$$\mathbf{n}_{\text{int}} \cdot (\lambda_c \nabla T_c - \lambda_v \nabla T_v) = \dot{m}_{\text{int}} \Gamma. \quad (3.92)$$

When phase reconstruction is used in combination with this method, it is possible to use a two field formulation and determine separate saturation temperatures for each phase at the interface. The model, however, neglects the slight temperature drop at

the interface caused by molecular kinetics during phase change. The mass flux due to phase change can be transferred to  $\mathcal{S}_\gamma$  by:

$$\mathcal{S}_\gamma = \frac{\dot{m}_{\text{int}}}{\rho_c} |\nabla\gamma|, \quad (3.93)$$

where the integral of  $|\nabla\gamma|$  across a CV is equal to the interfacial area within the CV. A simplified version of equation (3.92) was presented by NICHITA & THOME 2010, who use a single-field formulation for the jump condition.

$$\mathcal{S}_\gamma = \frac{\lambda (\nabla T \cdot \nabla \gamma)}{\Gamma} \quad (3.94)$$

This formulation may be used for a single-field formulation and uses the thermal conductivity  $\lambda$  of the mixture phase for the evaluation of  $\mathcal{S}_\gamma$ , which is a simplification, inducing an error. Additionally, the gradient of the phase fraction is only present at the interface and therefore, the model requires an interface for phase change to occur.

### 3.3.2 Schrage model

SCHRAGE 1953 considers the kinetic theory of gases and uses the Herz-Knudsen equation for the derivation of a mass transfer model. The vapor and condensate phase are at equilibrium conditions at the interface. However, the model allows for a jump in temperature and pressure across the interface. The mass flux  $\dot{m}_{\text{int}}$  across the interface is calculated by:

$$\dot{m}_{\text{int}} = \frac{2\zeta_S}{2 - \zeta_S} \sqrt{\frac{\bar{m}}{2\pi\mathcal{R}}} \left[ \frac{p_v}{\sqrt{T_{v \text{ sat}}}} - \frac{p_c}{\sqrt{T_{c \text{ sat}}}} \right]. \quad (3.95)$$

Here,  $\zeta_S$  represents the accommodation coefficient,  $\bar{m}$  the molar mass and  $\mathcal{R}$  the universal gas constant. The accommodation coefficient  $\zeta_S$  gives the relation between the molecules, which change their state during phase change and the molecules impinging the interface. Hence, the accommodation coefficient is bound between  $0 \leq \zeta_S \leq 1$  and ideal phase change leads to  $\zeta_S = 1$ . In equation (3.95), it is assumed that the value of the accommodation coefficient  $\zeta_S$  is the same for evaporation and condensation. The value of  $\zeta_S$  is unknown and should differ depending on the conditions at the interface. Many investigations are given in literature, which recommend values or value ranges of  $\zeta_S$  for specific flow conditions [KHARANGATE & MUDAWAR 2017]. This is still an unresolved issue, which means that  $\zeta_S$  is still an empiric quantity, which should differ within the simulation domain depending on local flow conditions at the interface during phase change.

TANASAWA 1991 uses the simplification that the mass flux is linearly dependent on the temperature jump between the vapor phase and the interface. With this assumption, the mass flux  $\dot{m}_{\text{int}}$  becomes proportional to the difference between the CV temperature

and saturation temperature. This leads to a single-field formulation of the phase change model:

$$\dot{m}_{\text{int}} = \frac{2\zeta_S}{2 - \zeta_S} \sqrt{\frac{\bar{m}}{2\pi\mathcal{R}}} \left[ \frac{\rho_v \Gamma (T - T_{\text{sat}})}{T_{\text{sat}}^{3/2}} \right]. \quad (3.96)$$

The mass flux due to phase change is again transferred to  $\mathcal{S}_\gamma$  by equation (3.93). Therefore, the applicability of the Schrage model [SCHRAGE 1953] also depends on an existing interface.

### 3.3.3 Numerical iteration techniques

Numerical iteration techniques aim at achieving saturation conditions at the interface by setting  $\mathcal{S}_q$  proportional to the temperature deviation from saturation conditions at the interface. Hence, kinetic energy contributions at the interface are not accounted for.

#### Lee model

A simpler model approach is given by LEE 1980, which is widely used in simulations. DE SCHEPPER ET AL. 2009 have shown that it is essentially a derivative form of the Schrage model. The model directly determines  $\mathcal{S}_q$  by:

$$\mathcal{S}_\gamma = \begin{cases} \zeta_L (1 - \gamma) \rho_v \frac{T - T_{\text{sat}}}{T_{\text{sat}}} & \text{for } T \leq T_{\text{sat}} \\ \zeta_L \gamma \rho_c \frac{T - T_{\text{sat}}}{T_{\text{sat}}} & \text{for } T > T_{\text{sat}}. \end{cases} \quad (3.97)$$

Here,  $\zeta_L$  is an empirical coefficient called the mass transfer intensity factor. The main disadvantage of the Lee model is that said coefficient is not limited to a maximum value. Multiple publications show that a good calibration of the Schrage model and the Lee model may lead to good results [HARDT & WONDRA 2008, KHARANGATE ET AL. 2015, WANG ET AL. 2007, SAMKHANIANI & ANSARI 2016]. A trade-off between simulation stability and accuracy is present when using the aforementioned models. If the model coefficient is too low, the interface temperature deviates from saturation conditions, and if the model coefficient is too large, the simulation stability decreases. SHEN ET AL. 2017 propose a method that allows for better simulation stability with high calibration coefficients by modifying the vapor's thermal conductivity in the two-phase region. This eases the calibration process, since divergence for high model coefficients is slightly counteracted.

The phase field model, introduced by BADILLO 2012, is an approach without a model calibration, where the arbitrary coefficient is calculated from the liquid properties and a characteristic length of the interface. Nonetheless, even if a good calibration is ensured,  $\zeta_L$  should still vary within the simulation domain, depending on the local flow

conditions and mesh resolution. The advantage of the Lee model is that it does not require a preexisting interface and thus, can account for phase change calculations in a bulk phase.

### Model of Rattner and Garimela

The idea behind the model of RATTNER & GARIMELLA 2014 is to determine the amount of enthalpy which is withdrawn from an interface CV. This enthalpy is then used to calculate the rate of phase change. The interface is considered to be at saturation conditions. The enthalpy withdrawn from an interface CV equals:

$$\Delta h = c_p (T - T_{\text{sat}}) . \quad (3.98)$$

A deviation of the interfacial temperature from saturation conditions would lead to evaporation or condensation, which would result in withdrawn or released latent heat of phase change, respectively, and the interfacial temperature would reach saturation conditions again.

This released latent heat of phase change is considered by the term  $\tilde{\mathcal{S}}_q$ , which is calculated by equation (3.99). This term is described as a heating rate, which forces the interface to saturation temperature at every time step. RATTNER & GARIMELLA 2014 also identify CVs, which contain the interface and limit the released latent heat to these CVs.

$$\tilde{\mathcal{S}}_q = \begin{cases} \frac{\rho c_p (T - T_{\text{sat}})}{\Delta t} & \text{if CV} \in \text{Interface CV} \\ 0 & \text{if CV} \notin \text{Interface CV} \end{cases} \quad (3.99)$$

The term  $\tilde{\mathcal{S}}_q$  is further limited, gaining the source term  $\mathcal{S}_q$  of the energy balance. The evaluation of  $\mathcal{S}_q$  is given in equation (3.100).

$$\mathcal{S}_q = \begin{cases} \min \left( \tilde{\mathcal{S}}_q, \frac{\gamma \rho_c \Gamma}{\Delta t}, \frac{\Gamma}{\Delta t} \left( \frac{1}{\rho_v} - \frac{1}{\rho_c} \right)^{-1} \right) & \text{for boiling} \\ \max \left( \tilde{\mathcal{S}}_q, -\frac{(1 - \gamma) \rho_v \Gamma}{\Delta t}, -\frac{\Gamma}{\Delta t} \left( \frac{1}{\rho_v} - \frac{1}{\rho_c} \right)^{-1} \right) & \text{for condensation} \end{cases} \quad (3.100)$$

Two limiting criteria are considered. First, the phase change rate must be limited by the mass within a CV which is available for phase change. The available volumetric mass is given by  $\gamma \rho_c$  and  $(1 - \gamma) \rho_v$  for boiling and condensation, respectively. It is the maximum amount of mass that can be transformed within the time step. This leads to a maximum amount of latent heat release or consumption due to phase change, which is given by the second argument in the min() or max() function of equation (3.100), respectively. The third argument of these functions is used for the second limitation,

with which the issue of numerical stability is considered. The change in specific volume due to phase change is considered and the phase change rate is limited to a maximum Courant number of  $Co \leq 1$ . RATTNER & GARIMELLA 2014 also use the Fourier number to limit the time step in their simulations. The Fourier number equals:

$$Fo := \frac{\lambda}{\rho c_p} \frac{\Delta t}{\Delta x^2}. \quad (3.101)$$

One advantage of the model of RATTNER & GARIMELLA 2014 is that it does not rely on an empirical parameter and should, therefore, be able to resolve local phase change rates accurately. The disadvantage is that it also requires an interface for phase change to occur.

## 4 Simulation Validation

This chapter has been published in a similar way in:

Kleiner, T.; Rehfeldt, S.; Klein, H.: *CFD model and simulation of pure substance condensation on horizontal tubes using the volume of fluid method*. International Journal of Heat and Mass Transfer 138 (2019) 420-431. DOI: [10.1016/j.ijheatmasstransfer.2019.04.054](https://doi.org/10.1016/j.ijheatmasstransfer.2019.04.054).

**Abstract** surface-structured tubes show a significant increase in efficiency of condensers, which can decrease the power consumption and CO<sub>2</sub> emission of chemical plants. However, no generalized condensation model for surface-structured tubes is developed so far, due to their complex structure. In future works, computational fluid dynamics is used for the investigation of surface-structured tubes. Therefore, in this study, a pure substance condensation model without heuristic or empirical parameters is introduced, by means of a new iteration scheme. The validation of the newly developed model is shown using the Stefan problem and different simulation approaches for pure substance condensation on a horizontal smooth tube, which are compared to Nusselt's film theory and measurements. The developed model shows a very good simulation stability, even for high temperature gradients. The simulation results of the Stefan problem stand in excellent agreement with the analytic solution. The horizontal smooth tube simulation results give slightly lower heat transfer coefficients compared to Nusselt's film theory, but are in very good agreement to experimental data.

## 4.1 Introduction

In this chapter, a phase change model KLEINER ET AL. 2019 for condensation/boiling is presented similar to the enthalpy method introduced by VOLLER ET AL. 1987, which was already successfully applied for melting by FADEN ET AL. 2018. The rate of phase change is evaluated using an iteration approach, evaluating the withdrawn heat flux from the interface and applying said heat flux as a source term at the interface cells. Due to this iteration approach, the developed algorithm allows handling of large temperature gradients during simulations. The phase change model is included in the multi-region framework of OpenFOAM. This enables CFD simulations of thermally coupled solid and fluid regions, in which a two-phase flow with phase change is solved in the fluid region. The OpenFOAM code *tpcMultiRegionFoam* is available on GitHub [KLEINER 2019]. The new phase change model is first validated using the 1D Stefan problem. The algorithm is then tested by different simulation approaches of pure substance condensation on a single horizontal smooth tube. The simulation results of the different simulation approaches are compared to Nusselt's film theory [NUSSELT 1916a]. Moreover, overall heat transfer coefficients are gained from the simulations and are further compared to condensation measurements of REIF 2016.

## 4.2 Mathematical formulation

The CFD model in this work is developed in OpenFOAM and the finite volume method-based implementation of the conservation laws is used. The solver itself is implemented in the multi-region framework of OpenFOAM, enabling calculations of conjugate heat transfer between solid and fluid mesh regions in the simulation domain.

### 4.2.1 Governing Equations

The following energy transport equation (4.1) is solved in solid regions of the simulation domain:

$$\frac{\partial}{\partial t} (\rho_s c_{ps} T) = \nabla \cdot (\lambda_s \nabla T) . \quad (4.1)$$

An incompressible two-phase flow with phase change is simulated within the fluid regions. In order to keep track of the phases during the mathematical formulation the index *c* will indicate the condensate phase and *v* the vapor phase. Variables without an index will refer to the phase mixture variable of a cell.

The two-phase flow simulation is based on the interFoam algorithm provided by OPENFOAM 2021, which solves an incompressible isothermal two-phase flow using the VOF method. The VOF implementation in OpenFOAM with phase change is described in sections 3.2.2 and 3.3. A brief description of the mathematical model used in this work is given below. The equations that are used from the beforementioned sections

are referenced accordingly and presented again in this section for a bundled description of the mathematical model of this work.

The VOF method introduces the volumetric phase fraction  $\gamma$  in equation (3.57) for the two-phase handling.

$$\gamma = \frac{V_c}{V} \quad \gamma \in [0, 1]$$

The material properties  $\Omega$  of each cell are calculated for the mixture phase of a cell according to equation (3.58).

$$\Omega = \gamma \Omega_c + (1 - \gamma) \Omega_v \quad \Omega \in [\eta, \rho, c_p, \lambda] .$$

The surface tension  $\sigma$  and the specific latent heat of evaporation  $\Gamma$  are considered to be constant throughout the fluid simulation domain.

The transport equations are calculated for the mixture phase of a cell with the discussed material properties  $\Omega$ . The phase transport equation is extended by the source term  $\mathcal{S}_\gamma$ , to account for phase change [RATTNER & GARIMELLA 2018]. Interface compression is considered and so the phase fraction is transported with the adjusted velocity field  $\mathbf{U}^*$  [WELLER 2002]. Hence, equation (3.86) using  $\mathbf{U}^*$  is solved. The exact formulation is given below:

$$\frac{\partial}{\partial t} (\gamma) + \nabla \cdot (\gamma \mathbf{U}) + \nabla \cdot (\gamma [1 - \gamma] \mathbf{U}_{\text{comp}}) = \mathcal{S}_\gamma .$$

In the implemented MULES algorithm, the shift of  $\gamma_p^I$  due to  $\mathcal{S}_\gamma$  is considered.

Analogously to RATTNER & GARIMELLA 2014, the continuity equation for incompressible flow given in equation (3.86) is used.

$$\nabla \cdot (\mathbf{U}) = \mathcal{S}_V$$

Following the interFoam implementation, the single field momentum equation (3.60) is solved for the mixture phase [RATTNER & GARIMELLA 2018].

$$\frac{\partial}{\partial t} (\rho \mathbf{U}) + \nabla \cdot (\rho \mathbf{U} \mathbf{U}) - \nabla \cdot [\eta (\nabla \mathbf{U} + [\nabla \mathbf{U}]^T)] = -\nabla p_{\text{rgh}} - \mathbf{g} \cdot \mathbf{x} \nabla \rho + \mathbf{f}_\sigma$$

Surface tension forces are considered by the source term  $\mathbf{f}_\sigma$  which is evaluated using the Continuum Surface Force (CSF) model by BRACKBILL ET AL. 1992, given in equation (3.61).

$$\mathbf{f}_\sigma = \sigma \nabla \cdot \left( \frac{\nabla \gamma}{|\nabla \gamma|} \right) \nabla \gamma$$

The pressure-velocity coupling is implemented using the PIMPLE algorithm provided by OpenFOAM. In this work, the PIMPLE algorithm is set to have a single PISO calculation during one time step iteration.

Equation (3.89) is used for the energy balance, which is similar to the work of ADHIKARI & RATTNER 2018. The energy balance is solved for temperature, which is why the following form of the energy balance is implemented.

$$\frac{\partial}{\partial t} (\rho c_p T) + \nabla \cdot (\rho \mathbf{U} c_p T) - \nabla \cdot (\lambda \nabla T) = \mathcal{S}_q \quad (4.2)$$

### 4.2.2 Phase Change Model

Most phase change models calculate the rate of phase change as a function of temperature without an additional iteration during one time step iteration [LEE 1980, RATTNER & GARIMELLA 2014]. However, the rate of phase change affects the source term  $\mathcal{S}_q$  in the energy balance and, thus, directly influences the temperature field itself. This coupled behavior leads to numerical instabilities when being iterated over multiple time steps, especially during transient simulations. An additional iteration cycle is introduced, in which the source term  $\mathcal{S}_q$  and the energy balance in equation (4.2) are iterated during one time step instead of being solved once. The rate of phase change is calculated from  $\mathcal{S}_q$  after the iteration. The iteration has a stabilizing effect, enabling a stable simulation at larger time steps and thereby accurate transient simulations.

The iteration given in figure 4.1 does not have a convergence criteria, instead a maximum number of iterations  $j_{\max}$  is used. The idea behind the proposed iteration scheme of figure 4.1 is to evaluate the heat flux, which will either be withdrawn from a surface cell (condensation,  $T^j < T_{\text{sat}}$ ) or added to a surface cell (evaporation,  $T^j > T_{\text{sat}}$ ) during the time step of the simulation. Since the temperature at the interface equals saturation temperature, the heat flux can be evaluated by using the temperature difference ( $T_{\text{sat}} - T$ ). By resolving the energy balance and adjusting its source term, it can be assured that  $\mathcal{S}_q$  is constrained at the interface, counteracting sub cooling of the gas phase or super heating of the liquid phase.

Another method to bound the source terms to the interface is to multiply them with a delta function that equals one at the interface and zero everywhere else [RATTNER & GARIMELLA 2014, RIEKS & KENIG 2018]. This method, however, relies on smaller time steps for accurate results, since the source terms are cut off rather than being shifted to the interface.

The multiplication of  $(1 - \gamma)$  for condensation and  $\gamma$  for evaporation takes into account that both phases are present in interface cells. Thus, for example, for condensation it is considered that the liquid phase of an interface cell can reach temperatures below saturation temperature. Therefore, the term  $(1 - \gamma)$  is multiplied with  $\mathcal{S}_q$  so that only the energy stream withdrawn from the gaseous phase is considered for condensation. Hence, the counteracting source term  $\mathcal{S}_q$  only prevents the gaseous phase

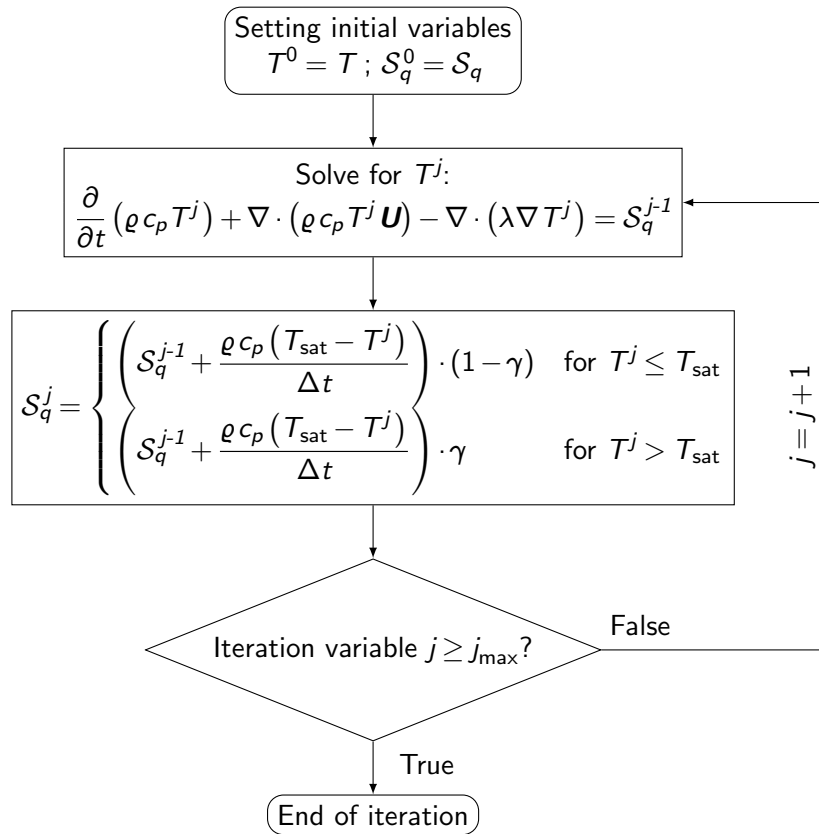


**Figure 4.1:** Iteration scheme for the evaluation of the energy balance source term  $S_q$ .

from a temperature decrease below saturation temperature. To increase stability of the simulation, a relaxation of  $S_q$  can be added to the iteration scheme.

After the iteration of the energy balance is complete, the volumetric rate of phase change is calculated by equation (3.90).

$$S_\gamma = \frac{S_q}{\Delta h} \frac{1}{\rho_c}$$

The term  $S_q/\Delta h$  corresponds to the mass transfer rate during phase change. This rate is also used to calculate  $S_V$  according to equation (3.91).

$$S_V = \frac{S_q}{\Delta h} \left( \frac{1}{\rho_c} - \frac{1}{\rho_v} \right)$$

### 4.3 Validation with the 1D Stefan problem

The 1D Stefan problem is a common validation case for phase change simulations [RATNER & GARIMELLA 2014, WELCH & WILSON 2000, RIEKS & KENIG 2018]. A horizontal wall is considered which is in contact with an infinitely spread vapor phase at saturation conditions. The wall itself has a constant temperature below the saturation

temperature of the above vapor phase. A condensate film will form on top of said wall. Assuming that no convection takes place and, therefore, only considering diffusive heat transfer, the film thickness  $\delta$  of the condensate is calculated as a function of time  $t$  using equation (4.3) [RATTNER & GARIMELLA 2014].

$$\delta(t) = \left[ 2t \left( \frac{\lambda_c}{\rho_c c_{pc}} \right) \left( \frac{1}{2} + \frac{\Gamma}{c_{pc} (T_{\text{sat}} - T_{\text{wall}})} \right)^{-1} \right]^{1/2} \quad (4.3)$$

The simulation domain for the Stefan problem is given in figure 4.2 for a mesh resolution of 50 cells in vertical direction. Since a constant wall temperature is considered for the Stefan problem, the simulation domain only covers the fluid region. The 1D simulation domain is 1 mm in height and has a uniform grading in vertical direction with the upper most cell being three times the height of the lowest cell. At the bottom of the simulation domain (solid line), a constant wall temperature is set to 10 K below saturation temperature  $T_{\text{sat}}$  of the simulated fluid. Furthermore, a no-slip condition is used for the flow and the phase indicator function  $\gamma$  is set to one. The temperature at the top boundary (dashed line) is set to saturation temperature, for the flow boundary condition, a fixed pressure is used to simulate the bulk vapor phase with the indicator function  $\gamma$  being set to zero.

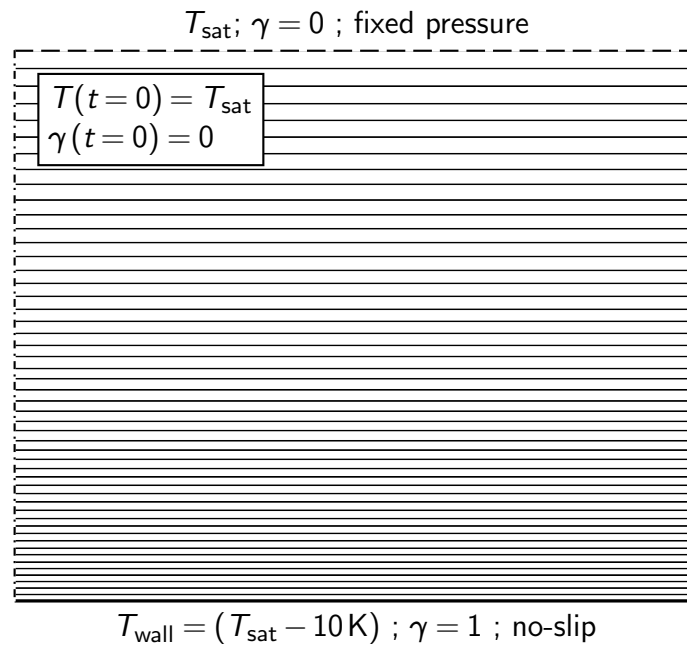


**Figure 4.2:** Stefan problem 1D simulation domain for a mesh resolution of 50 cells.

Simulations were performed at a pressure of 1.013 bar for water and pentane. The simulation properties are given in table 4.1.

**Table 4.1:** Properties of water and pentane for saturation conditions for  $p = 1.013$  bar [LINSTROM & MALLARD n.d., VDI 2013].

		Pentane	Water
Saturation temperature	$T_{\text{sat}}$	309.15 K	373.15 K
Latent heat of evaporation	$\Gamma$	355.26 kJ/kg	2256.5 kJ/kg
Surface tension	$\sigma$	14.117 mN/m	70.000 mN/m
<b>Vapor</b>			
Dynamic viscosity	$\eta_v$	7.3100 $\mu\text{Pa s}$	12.268 $\mu\text{Pa s}$
Density	$\rho_v$	2.9500 kg/m <sup>3</sup>	0.5981 kg/m <sup>3</sup>
Specific heat capacity	$c_{p_v}$	1.7695 kJ/(kg K)	2.0770 kJ/(kg K)
Thermal conductivity	$\lambda_v$	15.679 mW/(m K)	24.570 mW/(m K)
<b>Condensate</b>			
Dynamic viscosity	$\eta_c$	198.20 $\mu\text{Pa s}$	281.67 $\mu\text{Pa s}$
Density	$\rho_c$	609.00 kg/m <sup>3</sup>	958.35 kg/m <sup>3</sup>
Specific heat capacity	$c_{p_c}$	2.3180 kJ/(kg K)	4.2170 kJ/(kg K)
Thermal conductivity	$\lambda_c$	109.69 mW/(m K)	67.720 mW/(m K)

The time step of the simulation is limited to a maximum Courant number of  $Co_{\text{max}} = 0.4$  and a maximum Fourier number of  $Fo_{\text{max}} = 0.25$ .

Mesh convergence simulations were carried out for 50 cells, 100 cells, 200 cells and 300 cells in vertical direction. The necessary mesh resolution for mesh independence is 200 cells, resulting in a minimum cell height at the bottom of the simulation domain of approximately 2.7  $\mu\text{m}$ . The simulation results and the analytic solution to the Stefan problem are given in figure 4.3. The simulated film thickness fits the analytical solutions for both substances perfectly from 1 simulation second onward. The relative deviation of the simulation values to the analytic solutions is about 8 % after 0.02 s of simulated time. According to RATTNER & GARIMELLA 2014, this large initial deviation occurs, as the film is under-resolved during the beginning of the simulation. However, said deviation drops very rapidly below 1 %. After a simulated time of 10 s the relative deviation is 0.18 % for the water simulation and 0.53 % for the pentane simulation.

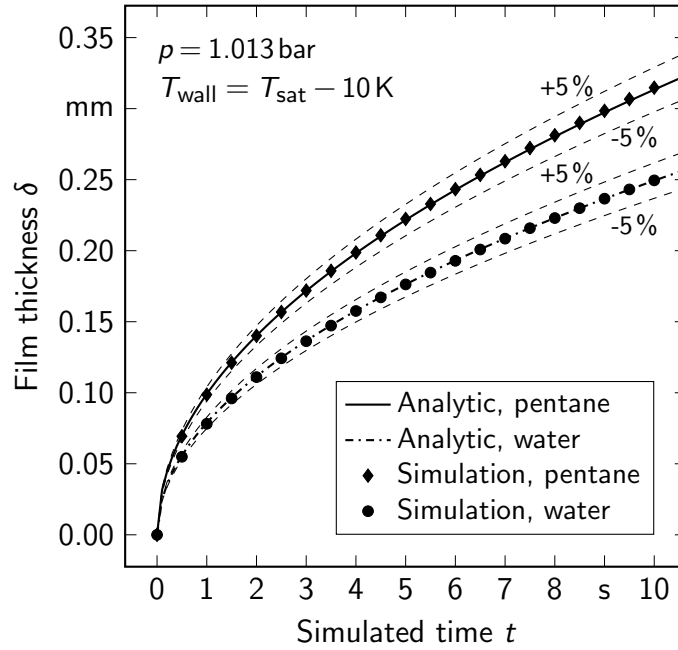


**Figure 4.3:** Simulated results and analytical solution of the Stefan problem.

## 4.4 Simulation of condensation on horizontal tubes

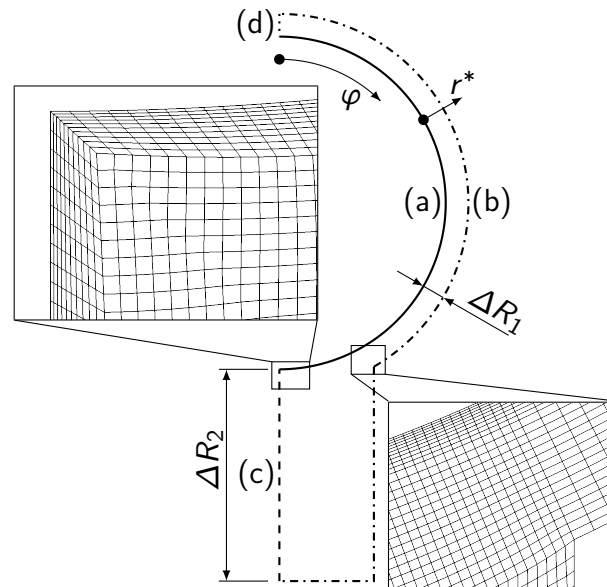
In this section simulations of pure substance condensation on a single horizontal tube are introduced and compare the results with Nusselt’s film theory [NUSSELT 1916a]. The properties of pentane from table 4.1 are used for all further simulations. Nusselt’s film theory stands in very good agreement with the pentane condensation measurements on horizontal smooth tubes from REIF 2016 and will function as a reference solution for the simulation approach.

### 4.4.1 Run-off behavior

A schematic of the 2D simulation domain and boundary conditions for horizontal tube condensation with run-off behavior of the condensate is given in figure 4.4.

The simulation domain covers the fluid phase around a horizontal tube. According to NUSSELT 1916a, a symmetric film will form around the sub-cooled tube. This information is used and only half the tube is considered. The symmetry plane is considered with the dotted boundary d) and the dashed boundary c). Since Nusselt’s film theory considers a run-off behavior of the condensate, a symmetry boundary condition cannot be used for boundary c), as it would set the phase fraction to zero gradient, equaling a contact angle of  $\theta = 90^\circ$  and resulting in the condensate dripping off at the regarded wall temperatures. Thus, boundary c) is set according to a slip wall condition with complete wetting ( $\theta = 0^\circ$ ).

The solid boundary a) represents the outer wall of a tube with a radius of  $r_o = 9.525 \text{ mm}$ . A no-slip boundary with complete wetting of the condensate is considered. A constant



Boundary	Temperature	Flow	Phase indication
(a)	$T = T_o$	No-slip	$\theta = 0^\circ$
(b)	$\nabla T = 0$	$p = 1.013 \text{ bar}$	$\nabla \gamma = 0$
(c)	$\nabla T = 0$	Slip	$\theta = 0^\circ$
(d)	Symmetry	Symmetry	Symmetry

**Figure 4.4:** Simulation domain for 2D horizontal tube condensation cases.

outer tube temperature  $T_o$  is set in order to being able to compare the simulation results with Nusselt's film theory. The dash dotted boundary b) represents the bulk phase with a constant pressure and a pressure dependent inlet/outlet boundary condition. For temperature and phase fraction, a zero gradient boundary condition is applied.

The mesh is kept short around the upper part of the tube ( $\Delta R_1 = 0.975 \text{ mm}$ ), where only a thin film is formed. The length of the simulation domain  $\Delta R_1$  is set accordingly, in order for the simulation results to be independent of  $\Delta R_1$ . At the bottom of the tube, the range of the mesh is increased to include the running off of the condensate ( $\Delta R_2 = 5.475 \text{ mm}$ ). The base mesh consists of hexahedral cells with simple grading in radial direction in mesh regions where the cells spread in radial direction. The grading is set in a way that the aspect ratio of the base mesh cells stays the same when moving away from boundary a). The base mesh cell length in radial direction is  $30 \mu\text{m}$  for the mesh independent solution. Since the interface will nearly be parallel to the tube wall at the upper part of the tube, the cell length in circular direction is set to be twice as large as in radial direction for revolution angles  $\varphi$  up to about  $150^\circ$ , whereas at higher revolution angles an aspect ratio of one is used. The location of the change in aspect ratio can be seen in figure 4.4 in the magnifying window to the right of boundary b). Ten additional refinement layers are added at the boundaries a) and c) resulting in a minimum cell length in radial direction of  $6.1 \mu\text{m}$  for the mesh independent solution.

The simulation starts with a uniform temperature field of  $T = T_{\text{sat}}$  and a thin liquid film around boundary a). Even though the developed solver does not rely on a pre-existing interface as compared to other phase change models [KHARANGATE & MUDAWAR 2017], a thin initial condensate film is used to reduce simulated time.

Simulations are carried out for different tube temperatures with a maximum Courant number of  $Co_{\text{max}} = 0.4$  and a maximum Fourier number of  $Fo_{\text{max}} = 1$ . The simulation progression for a tube temperature difference of  $(T_{\text{sat}} - T_o) = 50$  K is given in figure 4.5. In addition to the simulation results, the cross-section of half a smooth tube is given in gray as a visual aid.

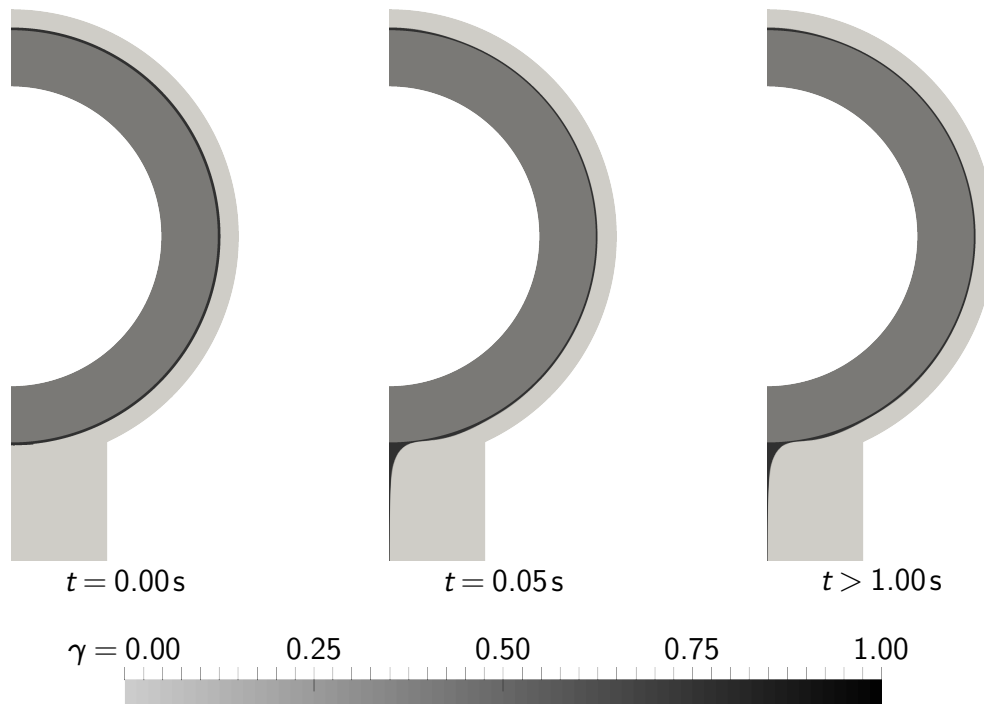


**Figure 4.5:** Simulation progression with condensate run-off behavior for a temperature difference of 50 K.

In the beginning of the simulation, the initial liquid condensate film is running off at the bottom of the tube. A very thin film with a large temperature gradient is gained. This induces numerical instabilities with decreasing wall temperature for steady state solutions. These instabilities, however, can be counteracted by increasing the temperature iterations. Stable simulations are gained with the before mentioned maximum Courant and Fourier numbers for low tube temperature differences. For tube temperature differences of  $(T_{\text{sat}} - T_o) > 30$  K the maximum Fourier number has to be decreased to  $Fo_{\text{max}} = 0.5$  and the temperature iterations have to be increased to 10 iterations per time step. A steady state for  $(T_{\text{sat}} - T_o) = 50$  K is reached after one simulation second.

In order to compare the simulation results with Nusselt's film theory, the outer heat transfer coefficient  $\alpha_o$  of the tube is calculated according to equation (2.11)

for boundary a) of figure 4.4. Even though a steady state with a constant heat flux  $\dot{q}_o$  across the outer tube wall is reached, an average value from the third simulation second to the tenth simulation second is used due to slight numerical noise in the solution. The gained heat flux is given over time in figure 4.11 for a temperature difference of 10 K and will be discussed later in more detail. The heat flux  $\dot{q}_o$  is calculated from the temperature and thermal conductivity fields of the simulation according to Fourier's law.

The outer heat transfer coefficients of the simulations are given in figure 4.6 along with the results from Nusselt's film theory. The film Reynolds number, given in equation (2.28), for the simulation with a temperature difference of 50 K equals  $Re_F = 103$ . According to GREGORIG 1973, Nusselt's film theory is applicable for such film Reynolds numbers on horizontal smooth tubes. Due to the comparison with Nusselt's film theory, laminar flow is considered during the simulation.

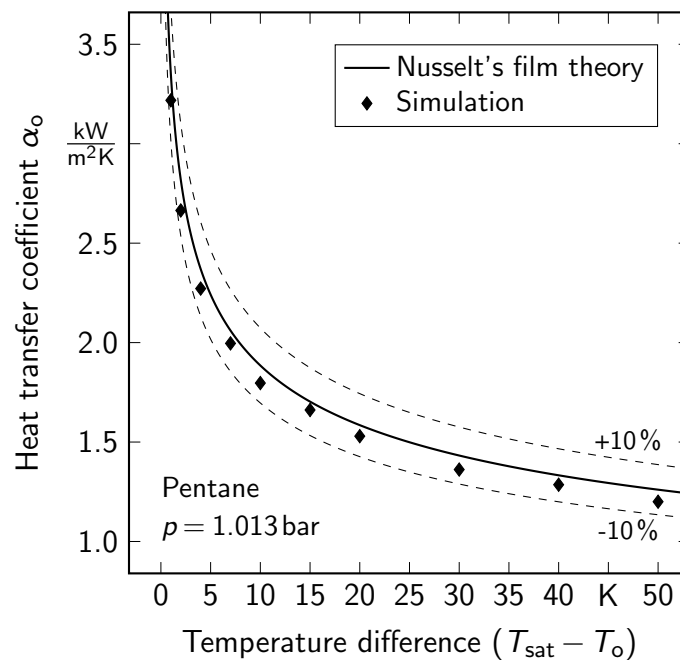


**Figure 4.6:** Simulation results of the 2D run-off simulations.

The simulated outer heat transfer coefficients stand in very good agreement with Nusselt's film theory for a large range of temperature differences. All simulated heat transfer coefficients give slightly smaller values compared to Nusselt's film theory, indicating a systematic deviation. The average relative deviation between the simulation and Nusselt's film theory is 4.1 % with the maximum deviation being 5.5 %.

The simulation with a temperature difference of 50 K is chosen for further investigation of the simulation results, as the simulation stability decreases with increasing temperature difference and deviations between Nusselt's film theory and the simulation should be most prominent. Figures 4.7, 4.8 and 4.9 show the temperature  $T$ , the volumetric phase fraction  $\gamma$  and the specific heat release due to condensation  $\mathcal{S}_q$  across the relative radial position  $r^*$  for revolution angles  $\varphi$  of  $45^\circ$ ,  $90^\circ$  and  $135^\circ$ , respectively. The trend of

Nusselt's film theory is determined by calculating the local film thickness according to equation (2.20) and considering a sharp interface for the phase fraction and a linear temperature profile between the outer tube wall and the interface. The approximation of Nusselt's film theory with a linear temperature profile is acceptable, since the film thickness is two orders of magnitude below the outer tube radius.

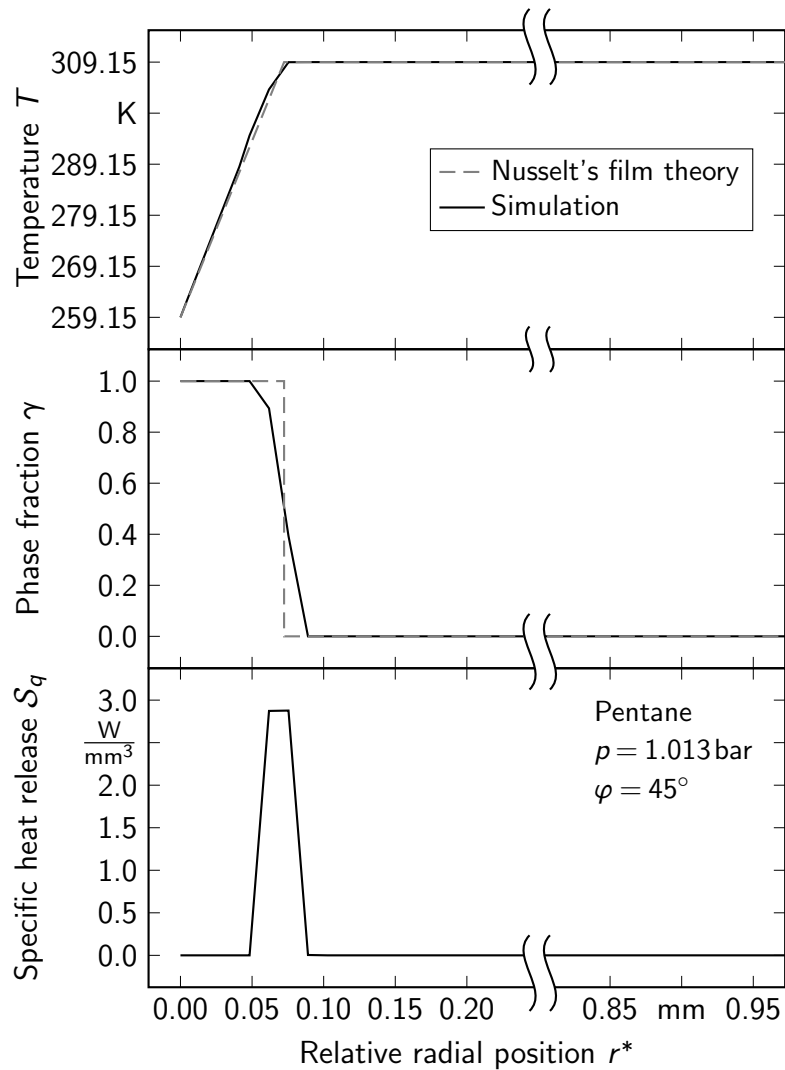


**Figure 4.7:** Temperature, phase fraction and specific heat release profiles at a revolution angle of  $45^\circ$ .

The simulation results for all three revolution angles show excellent agreements with Nusselt's film theory, especially considering that the interface is smeared due to the VOF method and that the phase fraction of the simulation reaches values between 0.4 and 0.5 at the corresponding predicted film thickness of Nusselt. The simulated temperature profile of all three revolution angles follows the linear progression of Nusselt's film theory. The specific heat release  $\mathcal{S}_q$  is present directly at the location of the interface suggested by Nusselt's film theory and in cells with a  $\gamma$  value of 0.5 in the simulation. When considering  $\gamma = 0.5$  as the criteria of the interface, which is assumed in VOF simulations without phase reconstruction, the source term keeps the vapor phase at

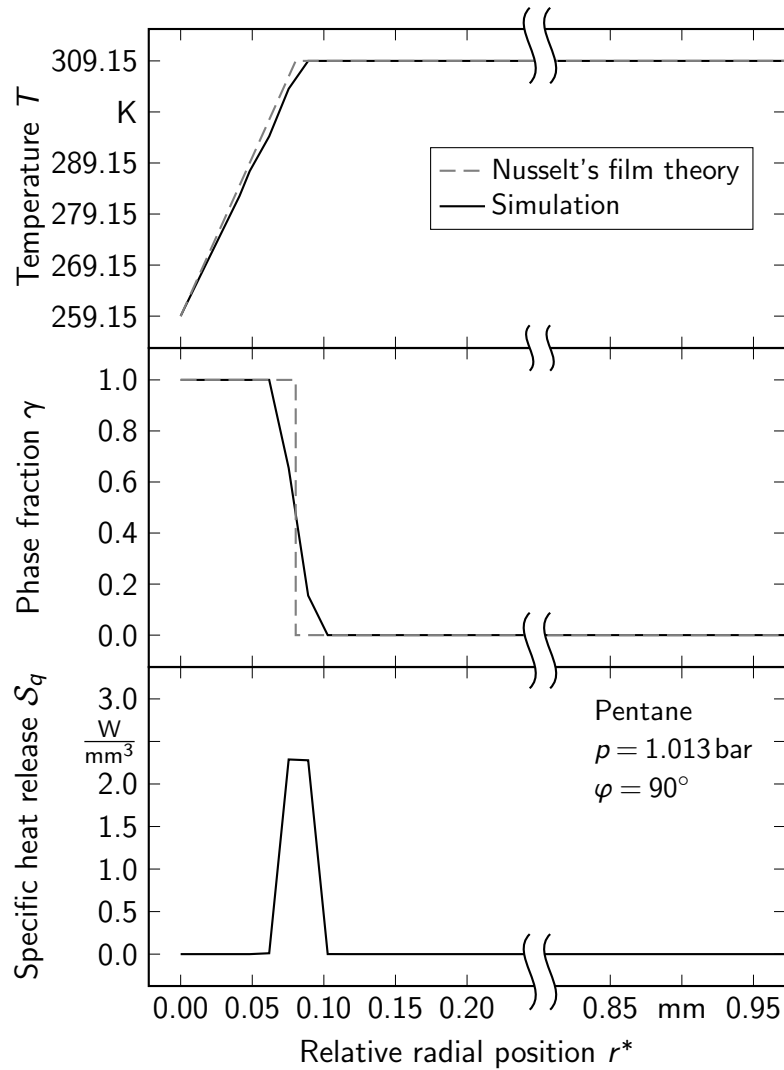


**Figure 4.8:** Temperature, phase fraction and specific heat release profiles at a revolution angle of  $90^\circ$ .

saturation temperature while the temperature decreases in the liquid phase. This is an important aspect, as a slight deviation of the location where saturation temperature is reached in the temperature profile causes noticeable change in the transferred heat flux for thin condensate films.

The accordance between the temperature profiles of the simulations and Nusselt's film theory suggests that mainly diffusive heat transfer in radial direction to the tube is present within the condensate film and thus, the local wall heat flux is merely dependent on the local film thickness. Therefore, the deviation between the simulated heat transfer coefficients and Nusselt's film theory should be explainable with the resulting condensate film.

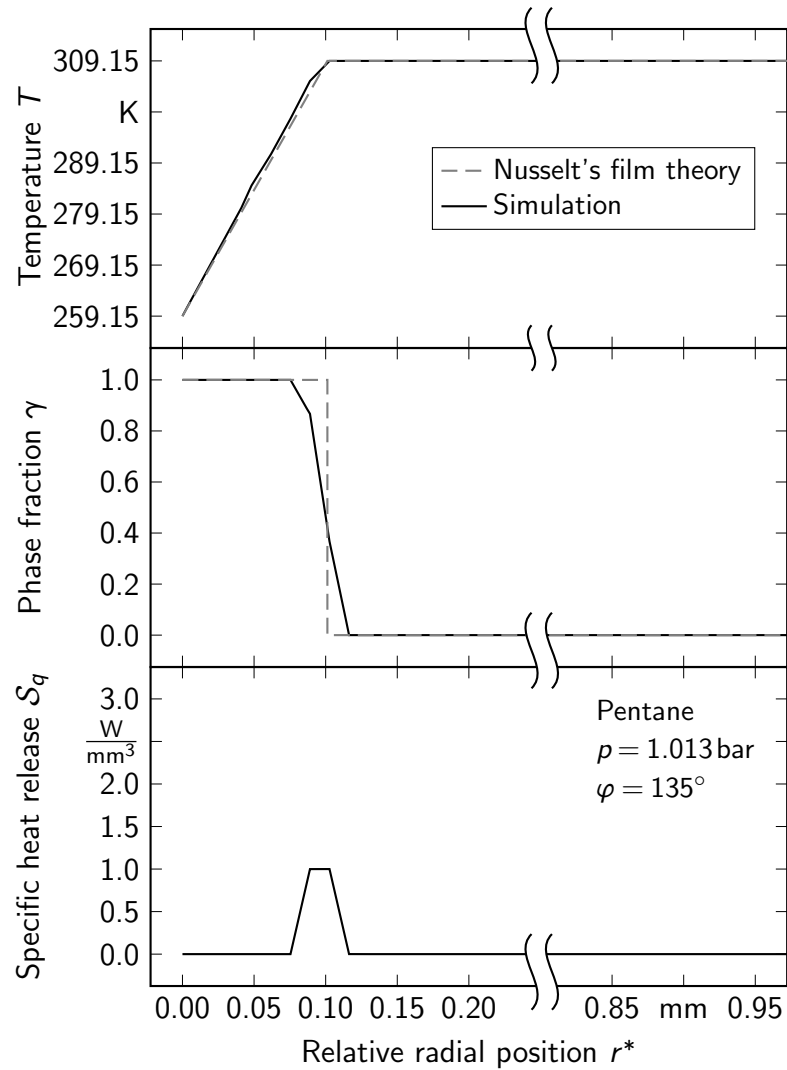


**Figure 4.9:** Temperature, phase fraction and specific heat release profiles at a revolution angle of  $135^\circ$ .

A comparison between the condensate film of Nusselt's film theory and the resulting condensate film of the simulation is given in figure 4.10. The simulation domain is reflected at the symmetry axis. Three magnifying windows 1), 2) and 3) are further given for the condensate film at the upper, mid and lower part of the tube, respectively. The location of the interface according to Nusselt's film theory is given as a dashed line. The location of the interface of the simulation is given as a black line, with a criteria for the interface of  $\gamma = 0.5$ .

The location of the interface of the simulation and Nusselt's film theory are in excellent agreement for the most part around the tube, as can be seen in the magnifying windows 1) and 2). Merely at the bottom part of the tube, magnified by window 3), a deviation is noticeable. This deviation can be traced back to the influence of the surface tension, which is considered in the simulation and neglected by Nusselt's film theory. Surface tension effects lead to a region of decreased pressure, where the condensate runs off the tube due to the concave interface. Therefore, a pressure gradient in the condensate is

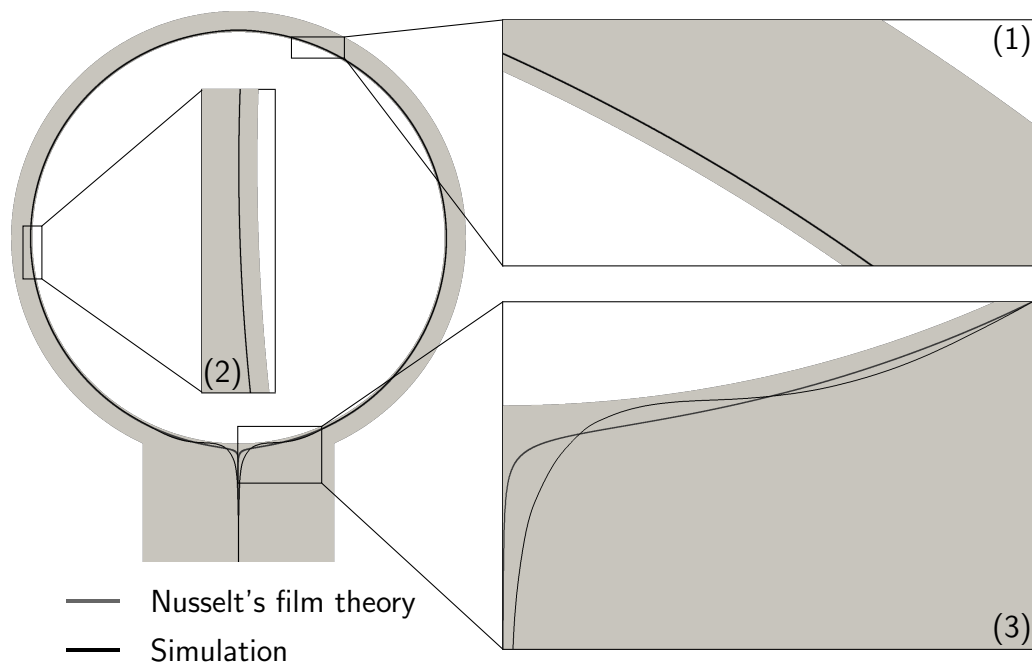


**Figure 4.10:** Interface location of condensate - Comparison between simulation and Nusselt's film theory.

present between the convex and concave parts of the interface, leading to an acceleration of the condensate and resulting in a decreased film thickness at a revolution angle of about  $173^\circ$ . The pressure decrease also explains, why the film thickness at revolution angles above  $175^\circ$  is thicker in the CFD simulations compared to Nusselt's film theory. The mean film thickness of the simulation is about 3% larger than the mean film thickness of Nusselt's film theory, which suggests that the deviation in the heat transfer coefficients of figure 4.6 is mainly attributed to surface tension effects.

#### 4.4.2 Drip-off behavior

Due to the comparison with Nusselt's film theory run-off behavior of the condensate was so far enforced in the simulations by the set boundary condition of boundary c). The highest simulated temperature difference is 50 K, corresponding to a maximum heat flux of  $\dot{q}_o = 60.5 \text{ W/m}^2$ . This heat flux, however, leads to the condensate dripping off the considered tube [HONDA ET AL. 1987]. Further, it is investigated whether the flow-off behavior has an influence on the transferred heat. For drip-off behavior, all boundary conditions of boundary c) given in figure 4.4 are set to symmetry conditions according to boundary d). Furthermore, no additional surface cell layers need to be added to boundary c).

For the drip-off simulations, no initial liquid layer is initially present. The simulation progresses similar to the run-off simulation given in figure 4.5, with the difference that the condensate drips off the tube. In the enlarged region of the simulation domain, the cross-section of a single drop forms and drips off when reaching a critical size. In the thin

region of the simulation domain, a thin film around the tube is formed, which is hardly influenced by the dripping off of the condensate. Due to this simulation progression, a periodic solution results compared to the steady state from section 4.4.1. As no steady state is achieved, the numerical stability of the simulation decreases compared to the run-off simulations because of the additional rapid changes in the temperature and source term field at the bottom of the tube when a droplet is dripping off. However, stable simulations are achieved with multiple temperature field iterations, showing the necessity of a source term iteration technique for transient simulations with rapid changes in the temperature field and large temperature gradients.

The heat flux  $\dot{q}_o$  is again evaluated using Fourier's law and given over time for the run-off and drip-off simulations for a temperature difference of 10 K in figure 4.11. The expected value according to Nusselt's film theory is given additionally as a dashed line.

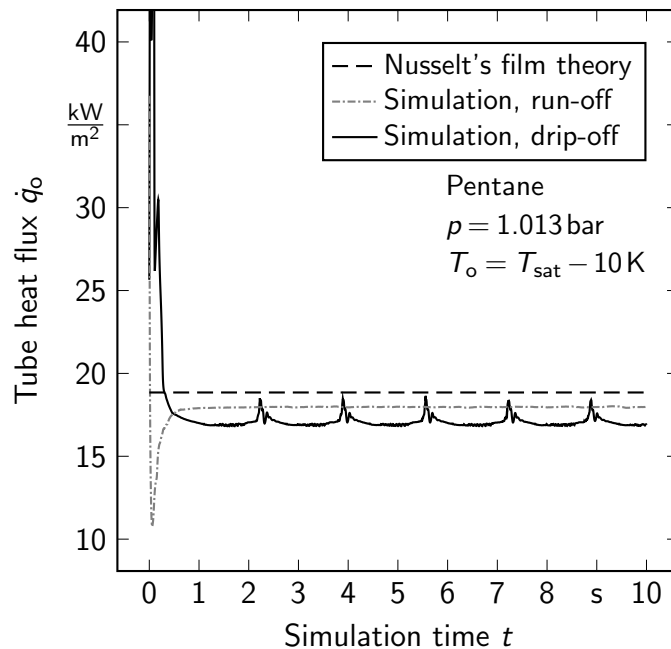


**Figure 4.11:** Outer tube wall heat flux over time for the run-off and drip-off simulations with a temperature difference of 10 K.

Both simulations start out with initial high wall heat fluxes, which decrease very rapidly. This is due to a high initial temperature gradient between the uniform internal temperature field  $T_{\text{sat}}$  and the boundary tube temperature  $T_o$ . The wall heat flux of the run-off simulation levels off to a constant value of about  $\dot{q}_o = 18 \text{ kW/m}^2$  after one simulation second, whereas the heat flux of the drip-off simulations reaches a periodic state after two simulation seconds with sharp peaks at every 1.7 simulation seconds and a mean heat flux of about  $\dot{q}_o = 17 \text{ kW/m}^2$ . The peaks in the periodic solution occur when the condensate droplet is dripping off. At this point, the wall heat flux is very close to the value suggested by Nusselt's film theory, which is plausible, since the film thickness deviation between theory and drip-off simulation is minimized at this point.

Furthermore, it is noticeable that at this point, the heat flux of the drip-off simulation is closer to Nusselt's film theory compared to the heat flux of the run-off simulation. This is caused by the dynamic change of the drip-off simulation counteracting the expansion of the film thickness due to surface tension. The amplitude of the heat flux during the periodic solution of the drip-off simulation is about  $\dot{q}_o = 2 \text{ kW/m}^2$  which corresponds to 12 % of its mean heat flux.

Temporal averaged values over multiple period cycles of the wall heat fluxes are used further on, since a periodic solution is gained for the drip-off simulations. The heat transfer coefficient is again calculated according to equation (2.11). The heat transfer coefficients of the drip-off simulations, the run-off simulations and Nusselt's film theory are given in figure 4.12.

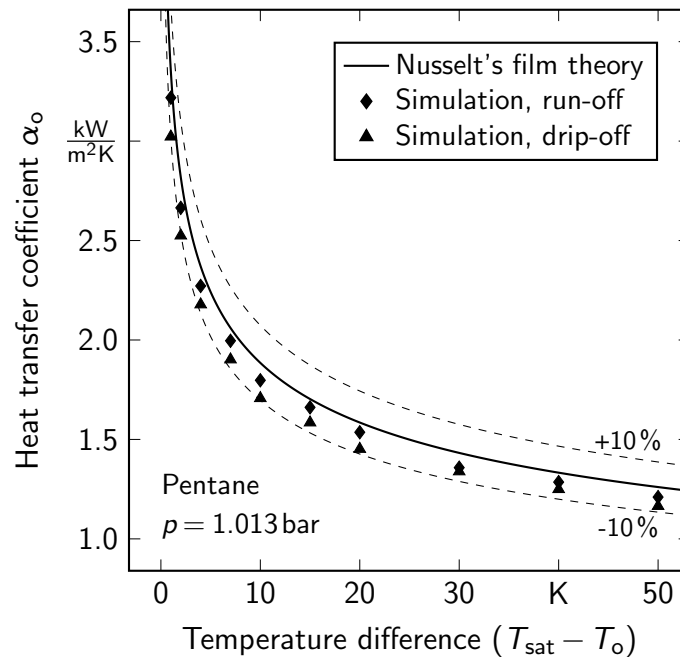
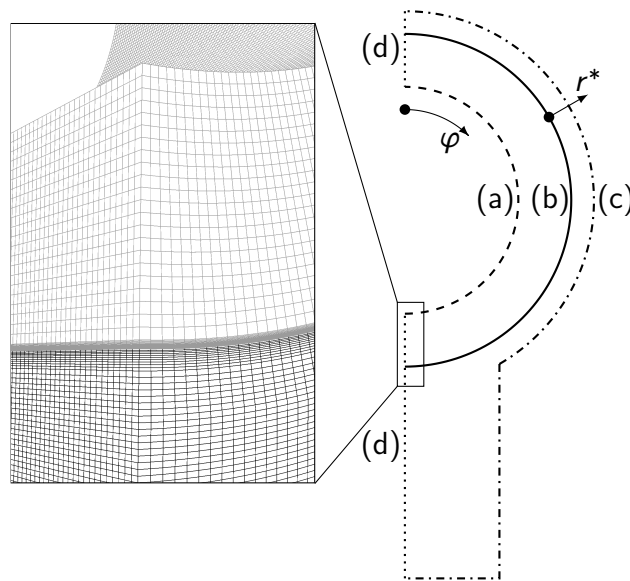


**Figure 4.12:** Simulation results of the 2D drip-off and run-off simulations.

Figure 4.12 shows similar trends for the heat transfer coefficients of the drip-off and run-off simulation results. Both simulation approaches result in lower heat transfer coefficients compared to Nusselt's film theory. The drip-off results are slightly lower as compared to the run-off results, which stands in accordance to the results of figure 4.11. The mean deviation between drip-off simulation results and Nusselt's film theory is 8.1 %. The relative deviation between run-off and drip-off simulation results slightly decreases with increasing temperature difference. This can be explained by an increase in drip-off frequency of the condensate with increasing temperature difference. As mentioned previously, a maximum heat flux is present when the condensate is dripping off, since the mean film thickness is minimized at this instance. Thus, with an increasing drip-off rate, the temporal mean of the heat transfer coefficient should approach the run-off simulation result.

### 4.4.3 3D simulation

The last simulation approach is a 3D simulation. All three approaches to simulate pure substance condensation on a horizontal smooth tube are then compared to the measurements of REIF 2016. In order to reproduce the measured data as closely as possible, the overall heat transfer between the inside of a single horizontal tube and the condensate bulk phase is considered in the 3D simulation. The 3D simulation domain includes the solid region of the tube as well as the fluid region around the tube and is given in figure 4.13 along with its boundary conditions. In order to distinguish between the inner and outer tube wall and stay in accordance with the previous chapters, the index “i” indicates the inner tube wall and the index “o” is kept for properties of the outer tube wall.



Boundary	Temperature	Flow	Phase indication
(a)	$\dot{q} = \text{const.}$	-	-
(b)	$\dot{q}(\text{tube}) = -\dot{q}(\text{fluid})$ $T(\text{tube}) = T(\text{fluid})$	No-slip	$\theta = 0^\circ$
(c)	$\nabla T = 0$	$p = 1.013 \text{ bar}$	$\nabla \gamma = 0$
(d)	Symmetry	Symmetry	Symmetry
front/back	Cyclic	Cyclic	Cyclic

**Figure 4.13:** Simulation domain for 3D horizontal tube condensation cases.

The inner tube radius is set according to the measurements of REIF 2016 to  $r_i = 6.92 \text{ mm}$ . The length of the simulation domain is set to the most dangerous wavelength of the thin film Rayleigh-Taylor instability [YOUNG ET AL. 1980] and equals  $L = 13.7 \text{ mm}$ . For the mesh independent solution, the fluid region mesh is set according to the 2D drip-off mesh with additional cells in the third dimension and the tube mesh has the

same base mesh size as the fluid region mesh and 20 additional boundary layers at boundary b). The magnified view in figure 4.13 shows part of the solid (gray) and fluid (black) mesh. Said view is slightly rotated so that the mesh resolution in axial direction is also shown. The fluid flow boundary and initial conditions of the fluid region of the 3D simulation are the same as the 2D drip-off simulations. The initial temperature of the fluid region is set to the saturation temperature of pentane. An estimated outer tube wall temperature, using the data of REIF 2016, is used as the initial temperature of the tube domain in order to reduce simulated time. The temperature boundary condition of boundary a) of the tube region is set to a fixed gradient condition such that a constant heat flux is withdrawn from the inner tube wall. The solid boundary b) is present in both, the tube and the fluid region, and handles the thermal coupling of the regions, where a boundary temperature, satisfying both temperature criteria given for boundary b) in the table of figure 4.13, is calculated. Said temperature is then applied as the boundary value of boundary b) for both regions at each time step.

3D simulations are carried out for targeted heat fluxes of  $\dot{q}_o = 20 \text{ kW/m}^2$ ,  $\dot{q}_o = 22 \text{ kW/m}^2$  and  $\dot{q}_o = 24 \text{ kW/m}^2$ . These targeted heat fluxes lead to film Reynolds numbers of  $Re_F = 34.0$ ,  $Re_F = 37.4$  and  $Re_F = 40.8$ , respectively. The heat flux of the dashed boundary a) is set accordingly. A carbon steel tube is considered in the simulations, with a density  $\rho_s = 7850 \text{ kg/m}^3$ , a specific heat capacity  $c_{ps} = 0.430 \text{ kJ/(kg K)}$  and a thermal conductivity  $\lambda_s = 55 \text{ W/(m K)}$ , as was used for measurements of REIF 2016. The simulations progress very stable and reach a periodic state at which a single droplet is dripping off at the bottom of the tube. The simulation progression of two sequential drip-off events of the periodic state is given in figure 4.14, where the tube is given in gray and the interface is given in blue. The criteria for the shown interface is  $\gamma = 0.5$ . The simulation domain is given three times in a row within each view of figure 4.14 for a better presentation of the fluid behavior. The interface of the actual simulation domain is given in a darker blue shade.

The fluid dynamic behavior given in figure 4.14 is as expected. The condensate flows to the bottom part of the tube and accumulates. A wave disturbance of the interface is formed. Its wavelength is equal to the most dangerous wavelength of the thin film Rayleigh-Taylor instability due to the set length of the simulation domain. A droplet forms at the peak of this disturbance and drips off. After the droplet breaks off of the condensate film, the condensate film snaps back releasing very small droplets in the progress, as can be seen in figure 4.14 at the simulated times  $t = 5.50 \text{ s}$  and  $t = 6.00 \text{ s}$ .

The drip-off location of the single drop changes throughout the simulation. A droplet forms every 0.40 s to 0.45 s. The duration of the drip-off event stays constant for the considered heat fluxes and takes about 0.10 s, whereas the overall drip-off frequency increases with increasing heat flux. During the simulation, the outer wall temperature of the tube reaches a steady value with negligible fluctuations, whereas the specific heat flux of the outer tube wall has a periodic behavior similar to the 2D drip-off simulation.

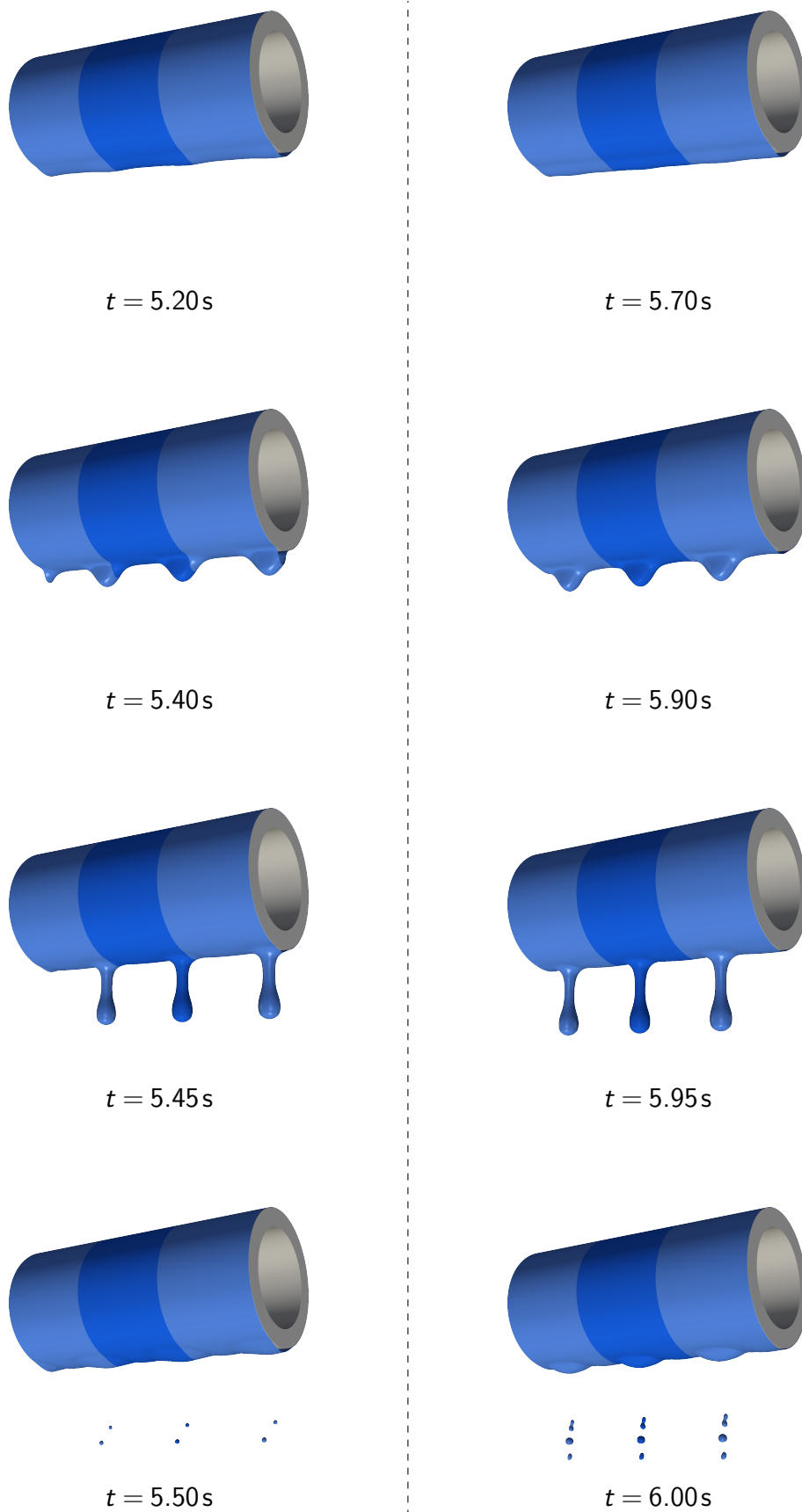


**Figure 4.14:** Drip-off progression of the 3D horizontal tube condensation simulation.

Time averaged values of the outer wall heat transfer coefficient are calculated for the 3D simulations and are given in figure 4.15 along with the measured heat transfer coefficients of REIF 2016 and the heat transfer coefficients of Nusselt's film theory and of both 2D simulation approaches (run-off and drip-off behavior).

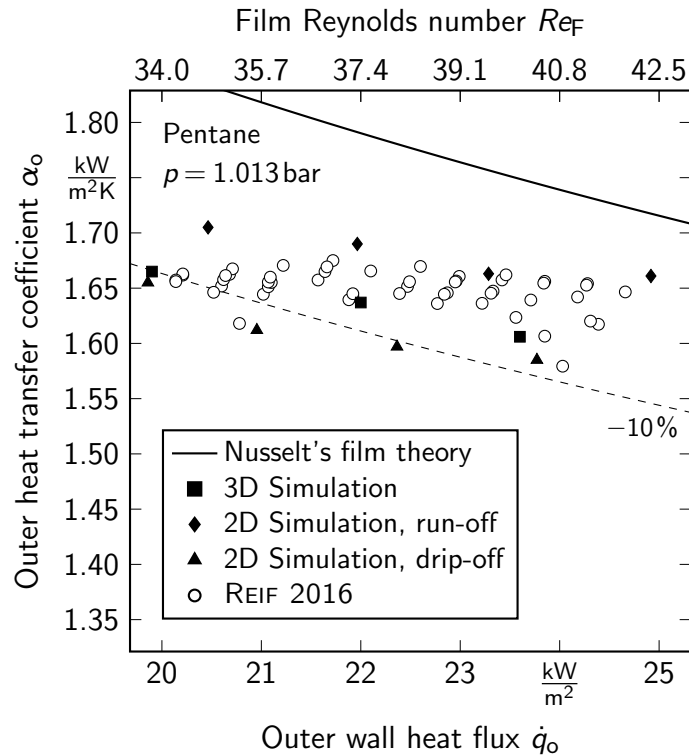


**Figure 4.15:** Comparison of outer heat transfer coefficients between the measurements of REIF 2016, Nusselt's film theory and the different simulation approaches.

As can be seen in figure 4.15, all simulated heat transfer coefficients are in agreement with the measurements of REIF 2016, which show lower heat transfer coefficients compared to Nusselt's film theory. The measured heat transfer coefficients lie between the run-off and drip-off simulation results. The drip-off simulation results align with lower bound and the run-off simulation results the upper bound of the measured heat transfer coefficients. The 3D simulation results fit the measurements best and lie between the two different 2D simulation approaches. The 3D simulation approach results are closer to the 2D drip-off simulation, which is plausible, since the condensate also accumulates at the bottom part of the tube throughout the tube length. The slight increase in heat transfer coefficient compared to the 2D drip-off simulation results should be due to the constriction of the condensate phase in axial direction and an increase in drip-off frequency due to the additional condensate streams in said direction.

Overall, all simulation approaches show very similar results of the heat transfer coefficient, which stand in very good agreement to the measurements of REIF 2016. The deviation to Nusselt's film theory is expected when considering surface tension.

The slight deviations between the simulation approaches are expected, considering their differences in flow-off behavior. This suggests a high simulation accuracy, since otherwise the deviation between the heat transfer coefficients of the different simulation approaches would not be separated this clearly.

## 4.5 Conclusion

A new CFD solver for thermally driven pure substance condensation based on the VOF method was developed and implemented in the OpenFOAM framework. Additionally, the solver structure allows for multiple solid and fluid regions, which can be thermally coupled for the evaluation of the overall heat transfer between a fluid and solid region. The suggested condensation model uses an iteration scheme to calculate phase change at the interface, similar to the melting model of FADEN ET AL. 2018 and, therefore, does not depend on a model calibration.

The 1D Stefan problem is used for validation of the phase change model. The simulation results for the properties of water and pentane stand in excellent agreement with the analytic solution. For a further evaluation of the solver accuracy, pentane condensing on a single horizontal smooth tube is simulated for different simulation approaches and compared to each other, to Nusselt's film theory and to measurements of REIF 2016.

The solver shows great stability for each simulation approach. The 2D simulation with run-off behavior resembles the condensate flow of Nusselt's film theory the best. All simulation approaches stand in very good agreement with Nusselt's film theory and lie within 10% deviation from Nusselt's film theory. Furthermore, the source terms considering phase change are located directly at the interface ( $\gamma = 0.5$ ), ensuring saturation condition at the interface. The film thickness also aligns with Nusselt's film theory [NUSSELT 1916a] for revolution angles  $\varphi < 150^\circ$ . The deviation of the film thickness at the bottom of the tube is expected due to consideration of surface tension in the simulations. The 2D simulation with drip-off behavior gives lower heat transfer coefficients. This is expected, since the accumulation of condensate at the bottom of the tube increases the temporal average of the film thickness. The fact that the deviation between the run-off and drip-off behavior decreases with decreasing wall temperature and that the run-off behavior always gives higher heat transfer coefficients compared to the drip-off behavior is plausible, due to an increase in the drip-off frequency. Since very small deviations between the heat transfer coefficient of the two simulation approaches are considered, a very accurate solver with a very good simulation stability for transient and steady state solutions has to be present in order to see this trend.

The 3D simulations with the overall heat transfer consideration between the inside of the tube and the vapor bulk phase fit the measurements of REIF 2016 best and lie between the simulation results of the 2D run-off and the 2D drip-off simulations, as is expected. However, the deviations between all simulation approaches is about 5% and the simulated time of the 3D simulation is an order of magnitude higher compared to the 2D simulations.

The agreement between the results of the 2D drip-off simulations and the 3D simulations of the presented study shows that when studying condensation/evaporation on surface-structured tubes, it will not be necessary to consider the droplet/bubble constriction along the tube axis. This allows for the length of the simulation domain in axial direction to be oriented at the surface structure rather than the most dangerous wavelength of the thin film Rayleigh-Taylor instability, generally decreasing the required number of cells for the simulation by two orders of magnitude and making it possible to study condensation on surface-structured tubes using the VOF approach.

The developed solver allows for stable simulations of steady state and transient solutions with a very high accuracy of the obtained heat transfer coefficient. The high accuracy of the heat transfer coefficients for thin condensate films is numerically challenging and relies on a very stable simulation. Thus, thermally driven pure substance condensation with complete wetting of the surface can be simulated using the suggested mathematical formulation. The developed solver shall further be used to investigate pure substance condensation on surface-structured tubes.

# 5 Simulation of Finned Tubes

This chapter has been published in a similar way in:

Kleiner, T.; Eder, A.; Rehfeldt, S.; Klein, H.: *Detailed CFD simulations of pure substance condensation on horizontal annular low-finned tubes including a parameter study of the fin slope*. International Journal of Heat and Mass Transfer 163 (2020) 120363. DOI: [10.1016/j.ijheatmasstransfer.2020.120363](https://doi.org/10.1016/j.ijheatmasstransfer.2020.120363).

**Abstract** The use of annular low-finned tubes in tube bundle condensers greatly increases the efficiency. This enables enhanced heat coupling within chemical plants, reducing the overall CO<sub>2</sub> emission and power consumption. Due to the complex geometry of these tubes, no generalized condensation model is present so far. In this study, highly resolved computational fluid dynamics simulations are used to investigate pure substance condensation on said tubes with a condensation model which is independent of empirical parameters. Within these simulations, the condensate film is fully resolved and heat transfer coefficients are calculated providing the complete information about the condensation process on annular low-finned tubes for the first time. Additionally, a parameter study for the incline of the annular fin is provided. Therefore, computational fluid dynamics is used to predictively evaluate the influence of a single fin parameter, the incline of the fin, of annular low-finned tubes, for the first time. The simulations provide information about the film thickness along the fin flank and the flooding behavior of the tubes. An accurate fluid dynamic behavior of the two-phase flow is gained. Furthermore, the resulting heat transfer coefficients stand in excellent agreement to experimental data.

## 5.1 Introduction

Within this section, the developed CFD code is used to investigate pure substance condensation on horizontal annular low-finned tubes, which was previously validated in chapter 4. For the first time, interface resolving CFD simulations using a phase change model without any model parameters will be used for the simulation of pure substance condensation on horizontal annular low-finned tubes. Furthermore, CFD simulations are used for predictive studies on the fin structure during condensation, which was not yet done before. Within this work, the incline of the fin is selected for a parameter study and evaluate its effect on the film thickness along the fin flank, the flooding angle and finally the outer heat transfer coefficient. Due to the simulations, it is possible to provide the complete information about the condensation process on annular low-finned tubes.

## 5.2 Condensation of pentane on a GEWA-K30 tube

The mathematical formulation of the simulations in this chapter is described in section 4.2. In order to evaluate the simulation accuracy and stability for finned tubes, the condensation of pentane on a GEWA-K30 tube from Wieland is first investigated and the resulting heat transfer coefficients are compared to measurements of REIF 2016. The properties of pentane, given in table 4.1 are used. A carbon steel tube is considered in the simulations again and the same properties from section 4.4.3 are used.

### 5.2.1 Simulation setup

The GEWA-K30 geometry is created using an image of the cross-section of the fin structure, provided by Wieland and published by REIF ET AL. 2015. Using the fin pitch (30 fins per inch) and fin height  $y = 0.9$  mm of these tubes, an estimated average fin structure is extracted. A comparison between the actual fins and the resulting CAD geometry is given in figure 5.1.

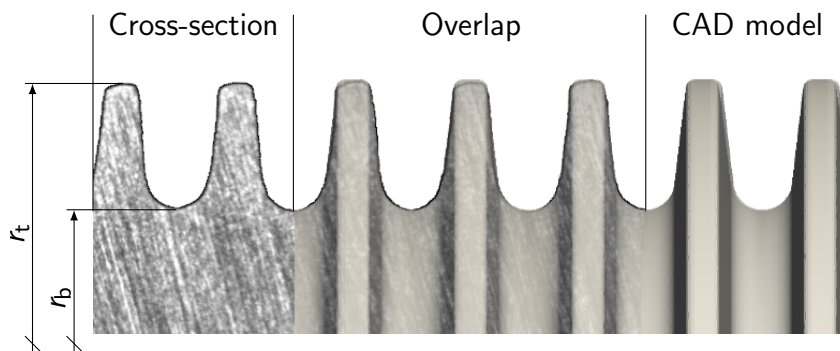
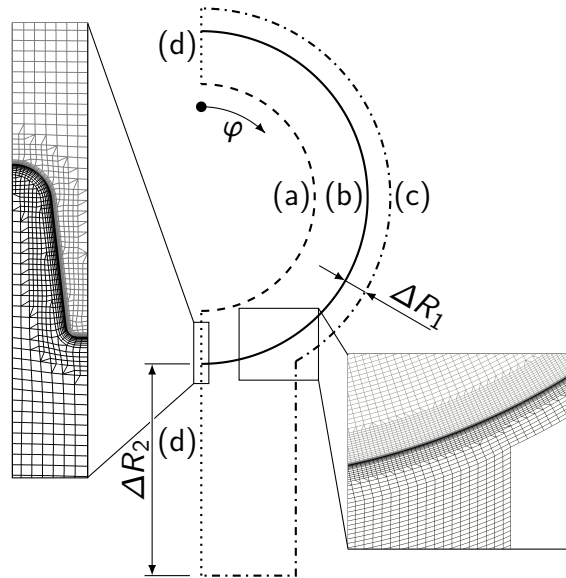


**Figure 5.1:** Comparison between the fin cross-section [REIF ET AL. 2015] of a GEWA-K30 tube and the CAD model

According to the overlap region of figure 5.1, the fin structure of the CAD geometry fits precisely to the cross-section of the actual fins. The provided radius  $r_t = 9.525$  mm of the fin tip of the GEWA-K30 tube is set for the radius of the fin tip of the CAD model.

The simulation setup for pure substance condensation on a GEWA-K30 tube is given in figure 5.2.



Boundary	Thermal	Flow	Phase indication
(a)	$\dot{q} = \text{const.}$	-	-
(b)	$\dot{q}(\text{solid}) = -\dot{q}(\text{fluid})$ $T(\text{solid}) = T(\text{fluid})$	No-slip	$\theta = 0^\circ$
(c)	$\nabla T = 0$	$p = 1.013 \text{ bar}$	$\nabla \gamma = 0$
(d)	Symmetry	Symmetry	Symmetry
Front/back	Symmetry	Symmetry	Symmetry

**Figure 5.2:** Simulation domain for condensation on horizontal low-finned tubes.

The setup is similar to the one used in chapter 4. The symmetry of the system is used and only one half of a tube is considered. Furthermore, two regions are present, one for the solid tube and one for the condensing phase around it. The meshes for the tube and fluid region are given in gray and black, respectively, within the magnifying windows of figure 5.2.

The length  $L = 0.425$  mm of the simulation domain covers half a fin and half a fin spacing in axial direction. A similar domain was also chosen by GEBAUER ET AL. 2013. The narrow simulation domain suppresses droplet inundation in axial direction. As shown in chapter 4 for smooth tubes, it is not necessary to cover a most critical wave length within the simulation domain, since droplet inundation hardly influences the

simulated heat transfer. Furthermore, accurate results are gained when averaging the periodic solution of a 2D drip-off simulation [KLEINER ET AL. 2019]. Consequently, the chosen simulation domain should provide accurate results, as all effects are covered within this domain, except for droplet inundation in axial direction. As shown in figure 5.2, the simulation domain is kept short ( $\Delta R_1 = 0.425$  mm) around the upper part of the tube and is extended ( $\Delta R_2 = 10.475$  mm) at the lower part of the tube at revolution angles  $\varphi > 155^\circ$ . It is ensured that these domain ranges are large enough and therefore do not influence the simulation results.

The set boundary conditions are given in the table within figure 5.2. Due to the symmetry of the fin and fin spacing, symmetry boundary conditions are used for the front and back plane of the simulation domain. The dashed boundary (a) in figure 5.2 is set to a constant heat flux, which is withdrawn from the inside of the tube. Both regions of the simulation domain are coupled thermodynamically on the outside of the tube at the solid boundary (b). In addition, a no-slip condition is used for the condensate flow on the outside of the tube and complete wetting is accounted for with a fix contact angle of  $\theta = 0^\circ$ . According to KLEIN & BÜCHNER 2018 film wise condensation occurs for pentane on steel. Hence, complete wetting is considered. The dash-dotted boundary (c) is defined as a boundary condition for the bulk vapor phase. A constant pressure with a pressure dependent inlet/outlet boundary condition is set as flow condition and a zero gradient condition is used for the temperature and volumetric phase fraction. As previously mentioned, the symmetry of the condensation process is used. Thus, the dotted boundary (d) is set as a symmetry plane. The mesh is generated using the cut-cell application *snappyHexMesh* from OpenFOAM. A structured base mesh is used with a simple grading in radial direction, when the mesh is expanded in this direction, in order to keep the aspect ratio of the cells in the base mesh constant throughout the simulation domain. This was also previously done for smooth tube simulations in chapter 4. For mesh independent solutions, the cell length of the base mesh equals about  $60 \mu\text{m}$ . A cell refinement is added around boundary (b). This causes a cell to be divided into 8 cells, doubling the resolution in all three dimensions. Additionally, boundary layers are added to boundary (b) for both regions. For mesh independent solutions, 7 boundary layers are added in the fluid region, with the lowest cell layer having a cell height of about  $4.7 \mu\text{m}$  normal to boundary (b). For stable simulations, it is important that a smooth transition in cell size is set in the fluid region mesh. This is achieved by setting the height of the boundary layer furthest away from boundary (b) to the size of the refined cells. For a high accuracy of the coupled regions, 5 boundary layers are also added to the tube region. The minimum cell height is set approximately to the minimum cell height in the fluid region.

### 5.2.2 Simulation progression and results

For initial conditions, motionless vapor is present throughout the fluid region and a uniform temperature of  $T = T_{\text{sat}}$  is set in both regions. Simulations are carried out for different heat fluxes  $\dot{q}_i$  at the inside of the tube. These heat fluxes are set in a way that

a targeted heat flux  $\dot{q}_o$ , which is defined in equation (5.1), is reached. This heat flux corresponds to an outer heat flux of a smooth tube with an outer radius equal to  $r_t$ , according to BÜCHNER ET AL. 2015.

$$\dot{q}_o = \frac{\dot{Q}}{2\pi r_t L} = \dot{q}_i \frac{r_i}{r_t} \quad (5.1)$$

In this study, the targeted heat fluxes are  $\dot{q}_o = 20.0 \text{ kW/m}^2$ ,  $\dot{q}_o = 22.5 \text{ kW/m}^2$ ,  $\dot{q}_o = 25.0 \text{ kW/m}^2$ ,  $\dot{q}_o = 27.5 \text{ kW/m}^2$  and  $\dot{q}_o = 30.0 \text{ kW/m}^2$ . They correspond to film Reynolds numbers of  $Re_F = 34.0$ ,  $Re_F = 38.2$ ,  $Re_F = 42.5$ ,  $Re_F = 46.7$  and  $Re_F = 51.0$ , respectively. In accordance to equation (2.28), the film Reynolds number is defined for a targeted heat flux:

$$Re_F = 4 \frac{\dot{q}_o r_o \pi}{\eta \Gamma}. \quad (5.2)$$

The simulation time step size is limited by a maximum Fourier number  $Fo_{\max} = 0.50$  and a maximum Courant number  $Co_{\max} = 0.25$  within the fluid region.

The simulation progression is given in figure 5.3, where the focus is laid on the formed condensate inside the fin spacing.

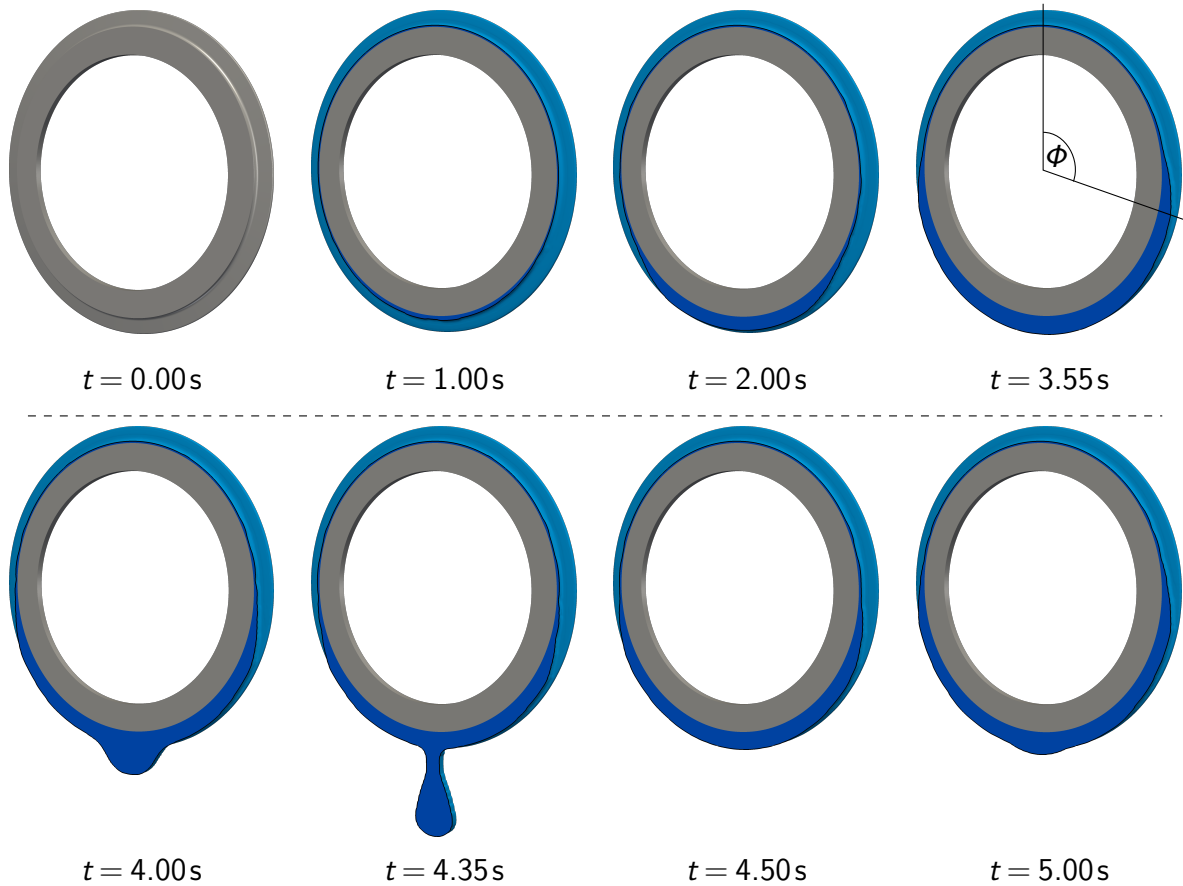


**Figure 5.3:** Simulation progression of pure substance condensation on a horizontal GEWA-K30 tube.

The simulation domain is mirrored along its symmetry boundary (d) for better visualization of the results. The tube region is depicted in gray, the condensate bulk phase in dark blue and the condensate interface in a lighter blue shade around the fin flank.

No condensate is present at the beginning of the simulation. After a simulated time of  $t = 1.00$  s, a condensate film is formed along the fins and a slight accumulation of condensate is visible at the lower part of the tube. This accumulation of condensate increases as the simulation progresses until  $t = 3.55$  s. At this time, the maximum accumulation of condensate is reached and the flooding angle  $\Phi$ , which is defined according to HONDA ET AL. 1983, reaches its minimum. As more condensate accumulates at the bottom of the tube, forces due to gravity outweigh surface tension forces and a droplet is formed. From this point onward, the simulation progresses in a periodic manner with a frequency of about 1 droplet per second. This periodic behavior is shown in figure 5.3 from  $t = 4$  s to  $t = 5$  s. The flooding angle  $\Phi$  increases as a droplet is formed and jumps back to its minimum value after the condensate drips off.

Since a constant heat flux is set as the boundary condition for boundary (a) (cf. figure 5.2) at the inside of the tube, the averaged inner wall temperature  $T_i$  of the tube changes during the simulation. Figure 5.4 shows this change in average temperature for different targeted heat fluxes.

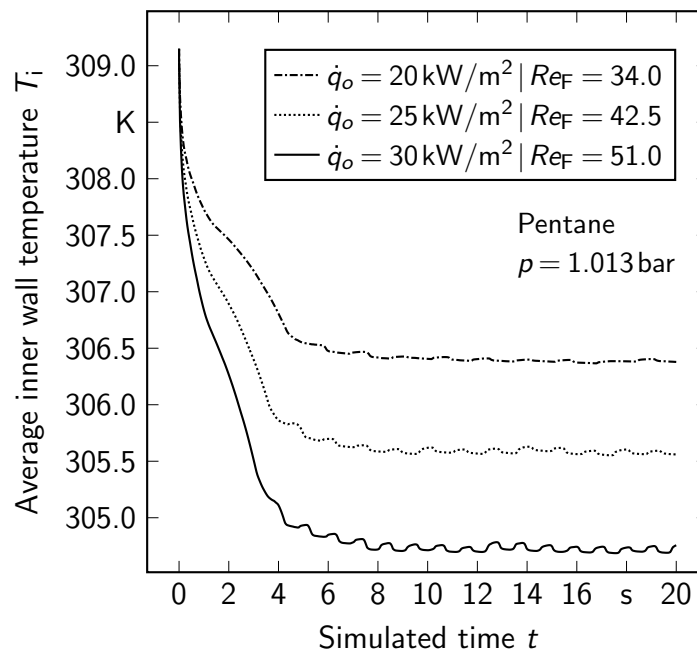


**Figure 5.4:** Change in average inner wall temperature of the tube over the simulated time for pure substance condensation on a horizontal GEWA-K30 tube.

The average inner wall temperature of all simulations progress in a similar way. Following, the change in inner wall temperature is discussed for a targeted heat flux of  $\dot{q}_o = 25 \text{ kW/m}^2$ . This temperature decreases rapidly at the beginning of the simulation,

during which period hardly any condensate is present at the outside of the tube. Consequently, the outer heat transfer resistance is negligible and the temperature decrease follows a hyperbolic function up to about 1.5 s of the simulated time.

After about 1.5 s, the average inner wall temperature decreases further, which is attributed to the condensate accumulation up to 3.55 s. This leads to an increase in thermal resistance, causing a steeper decrease of the average inner wall temperature of the tube. As mentioned above, at about 3.55 s, the minimum flooding angle is reached for a withdrawn heat flux of  $\dot{q}_o = 25 \text{ kW/m}^2$  and a droplet begins to form. This results in an increase in flooding angle and therefore, in a decrease of the outer thermal resistance, resulting in a decreasing change in the average inner wall temperature.

The periodic behavior is also visible in figure 5.4 for larger simulated times. During this period, the average inner wall temperature of the tube increases whenever a droplet is formed due to an increasing flooding angle and decreases due to the condensate dripping off.

The average wall temperature decreases stronger with a larger targeted heat flux. This is due to a higher thermal resistance of the formed condensate film according to the Nusselt film theory. Moreover, the amplitude of the temperature increases with increasing targeted heat flux during the periodic behavior of the simulation. This is plausible and shows the high accuracy of the simulations, since such a small change between the temperature profiles is resolved by the simulations.

For a comparison between the simulations and measurements, the outer heat transfer coefficient  $\alpha_o$  is determined by the use of the overall heat transfer coefficient  $k_o$  from section 2.1, which is given for this case in equation (5.3). This approach ensures conservative results for the outer heat transfer coefficient  $\alpha_o$ .

$$k_o = \frac{\dot{q}_o}{T_{\text{sat}} - T_i} \quad (5.3)$$

For the evaluation of the overall heat transfer coefficient, a temporal average over multiple drip-off periods is used for the average inner wall temperature  $T_i$  of the tube.

The outer heat transfer coefficient  $\alpha_o$  is calculated using equation (5.4), according to the definition of BÜCHNER ET AL. 2015:

$$\alpha_o = \left[ \frac{1}{k_o} - \frac{r_t \ln(r_b/r_i)}{\lambda_s} \right]^{-1}. \quad (5.4)$$

The outer heat transfer coefficient is given in figure 5.5 for different withdrawn heat fluxes. Measurements of REIF 2016, the model of BRIGGS & ROSE 1995 and the model of REIF ET AL. 2019, with a deviation of  $\pm 20\%$ , are additionally shown in figure 5.5.

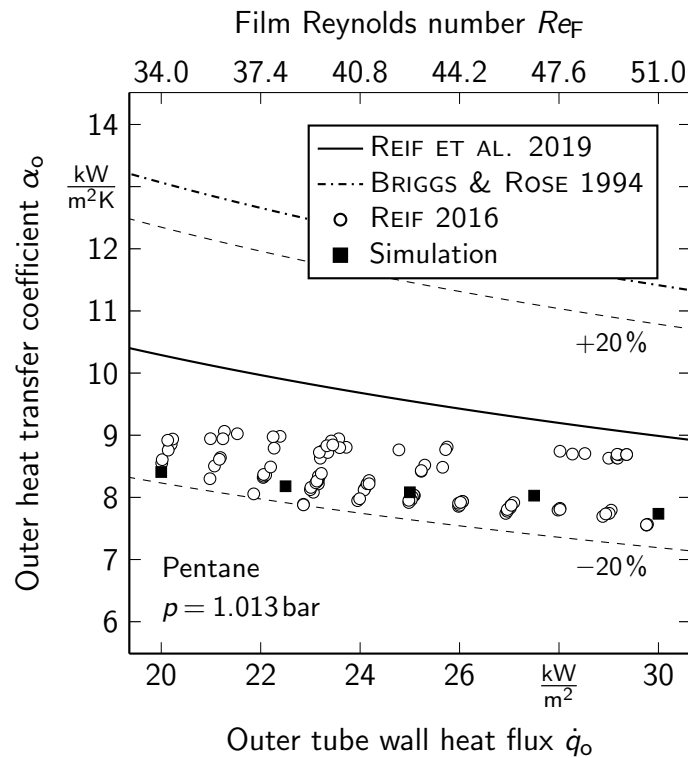


**Figure 5.5:** Change of the outer heat transfer coefficient for different targeted withdrawn heat fluxes for the condensation of pentane on a GEWA-K30 tube.

The model of BRIGGS & ROSE 1994 was used as an example for available models developed for the condensation of refrigerants. As can be seen in figure 5.5, it suggests much higher heat transfer coefficients for condensation of pentane on a GEWA-K30 tube and shows a high deviation to the measurements of REIF 2016. This deviation is due to the model of BRIGGS & ROSE 1994 being developed for condensation of refrigerants on copper tubes. The model of REIF ET AL. 2019 stands in good agreement to the experimental data. As the experimental data [REIF 2016] is used for the model fit along with other hydrocarbon measurements, all measurements lie within the provided model accuracy of  $\pm 20\%$ .

The resulting heat transfer coefficients of the simulations stand in excellent agreement with the experimental data [REIF 2016]. Since the phase change model does not rely on any input parameters, we also expect similar agreement for other materials. Excellent agreement was already observed for the Stefan problem with condensing water in chapter 4.

It is also possible to evaluate the heat transfer coefficient for the flooded and non-flooded region separately. The simulation results are averaged over its periodic behavior for this evaluation. The heat transfer coefficient  $\alpha_{\text{non-flooded}}$  of the non-flooded region and  $\alpha_{\text{flooded}}$  of the flooded region are evaluated from  $\varphi = 0^\circ$  to  $\varphi = 45^\circ$  and  $\varphi = 135^\circ$  to  $\varphi = 180^\circ$ , respectively. The relation between the heat transfer coefficient  $\alpha_{\text{flooded}}$  and  $\alpha_{\text{non-flooded}}$  equals  $\alpha_{\text{non-flooded}} = 2.98 \alpha_{\text{flooded}}$  for a targeted heat flux of  $\dot{q}_0 = 20 \text{ kW/m}^2$ . The relation

between the heat transfer coefficients slightly decreases with increasing withdrawn heat flux, due to an increasing film thickness along the fin flank in the non-flooded region to  $\alpha_{\text{non-flooded}} = 2.89 \alpha_{\text{flooded}}$  for a targeted heat flux of  $\dot{q}_o = 30 \text{ kW/m}^2$ . This increase however seems negligible considering that the targeted heat flux increases by 50 %.

In general, the high stability and accuracy of the simulations allows to carry out a parameter study on annular low-finned tubes with reliable results.

### 5.3 Variation of the incline of the fin

CFD simulations make it possible to easily study the effect of a single geometric parameter of the fins on the condensation process. The incline of the fin is further varied and its influence on fluid dynamics and heat transfer is determined, especially the film thickness of the condensate  $\delta$ , the flooding angle  $\Phi$  and the heat transfer coefficient  $\alpha$ . For all further simulations a targeted heat flux of  $\dot{q}_o = 25 \text{ kW/m}^2$  is used. This corresponds to a film Reynolds number of  $Re_F = 42.5$ .

#### 5.3.1 Geometric parameters and meshes

Schematic representations of the considered fin geometries are given in figure 5.6.

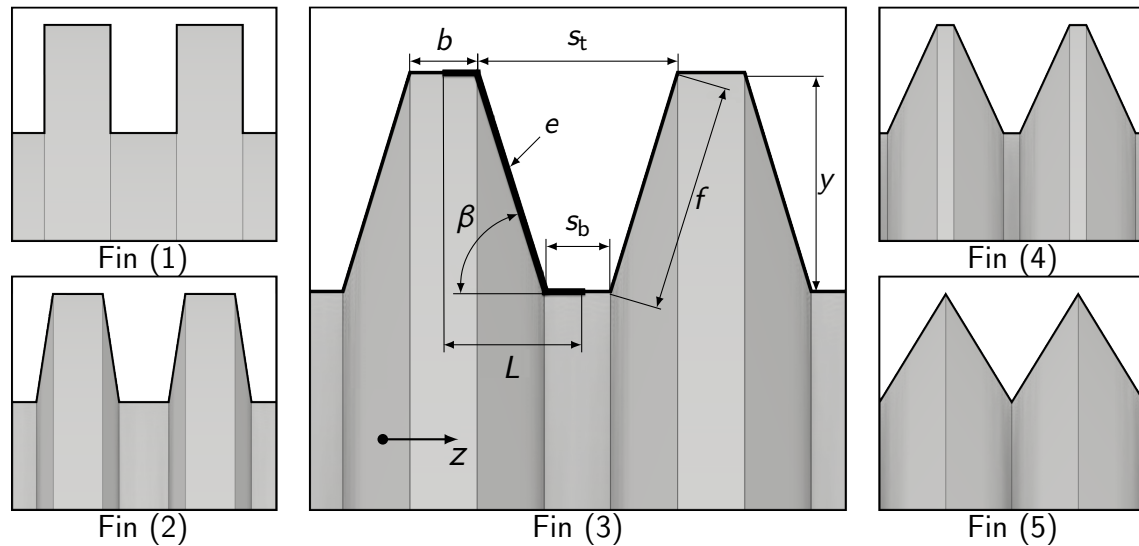


**Figure 5.6:** Examined fin geometries with different fin angles  $\beta$ .

The design parameter is called fin angle  $\beta$  and describes the incline of the fin flank, as can be seen in figure 5.6 together with other relevant geometric fin parameters.

The basic dimensions (fin height  $y = 0.9 \text{ mm}$ , inner tube radius  $r_i = 6.92 \text{ mm}$ , fin base radius  $r_b = 8.625 \text{ mm}$  and fin tip radius  $r_t = 9.525 \text{ mm}$ ) are based on the GEWA-K30 tube from section 5.2. The condition  $b = s_b$  is set further on, where  $b$  is the fin thickness

at the fin tip and  $s_b$  is the fin spacing at the fin base. Both, the length  $L = 0.55$  mm of the simulation domain and the fin height  $y$  are the same for all fins. Based on these specifications, the fin angle  $\beta$  is varied in a way that two extreme cases of a rectangular fin (1), and a triangular fin (5), are created. In between, fin (2) to (4) are created with an equidistant change in fin thickness at the fin tip for all fins. The midpoints of all fin flanks meet at a point which is located at half the fin height and half the domain length. The length of the fin flank  $f = y / \sin(\beta)$  is also introduced, which is determined by  $e = b/2 + s_b/2 + f$ . The resulting dimensions for the different fins are summarized in table 5.1.

**Table 5.1:** Varying dimensions of fins (1) to (5).

Fin	(1)	(2)	(3)	(4)	(5)
$\beta$	90.00°	81.31°	73.01°	65.38°	58.57°
$s_t$ in mm	0.275	0.481	0.688	0.894	1.100
$s_b$ in mm	0.275	0.206	0.138	0.069	0.000
$b$ in mm	0.275	0.206	0.138	0.069	0.000
$f$ in mm	0.900	0.910	0.941	0.990	1.055

The simulation setup is set as described in figure 5.2. The mesh resolutions of the fins are given in figure 5.7. The symmetries of the fins are used again and only half a fin is covered in the simulation domains. For each simulation and fin, two meshes are required, one for the fluid region (black) and one for the solid region (gray), as given in figure 5.7.

Seven additional refinement layers are added in the fluid region along the fin edge with a minimum cell height of  $5.2 \mu\text{m}$  for the mesh independent solution. Structured meshes are used for fins (1) to (4). The difficulty in mesh generation increases with decreasing fin angles  $\beta$  to the extent that it was impossible to create a satisfactory structured mesh for two-phase simulations for fin (5). Therefore, a hexadominant mesh for fin (5) was created with the cut-cell method using *snappyHexMesh*. The base mesh cell length in radial direction is  $60 \mu\text{m}$ . A cell refinement level and 7 additional boundary layers were added along the fin edge. The minimum cell height of the structured meshes of fins (1) to (4) were used as a target for the smallest cell boundary layer. The average cell height of the smallest cell boundary layer for the mesh independent solution of fin (5) is  $7.4 \mu\text{m}$ . The deviation in minimum cell height to fins (1) to (4) is due to limitations of the cut-cell method.

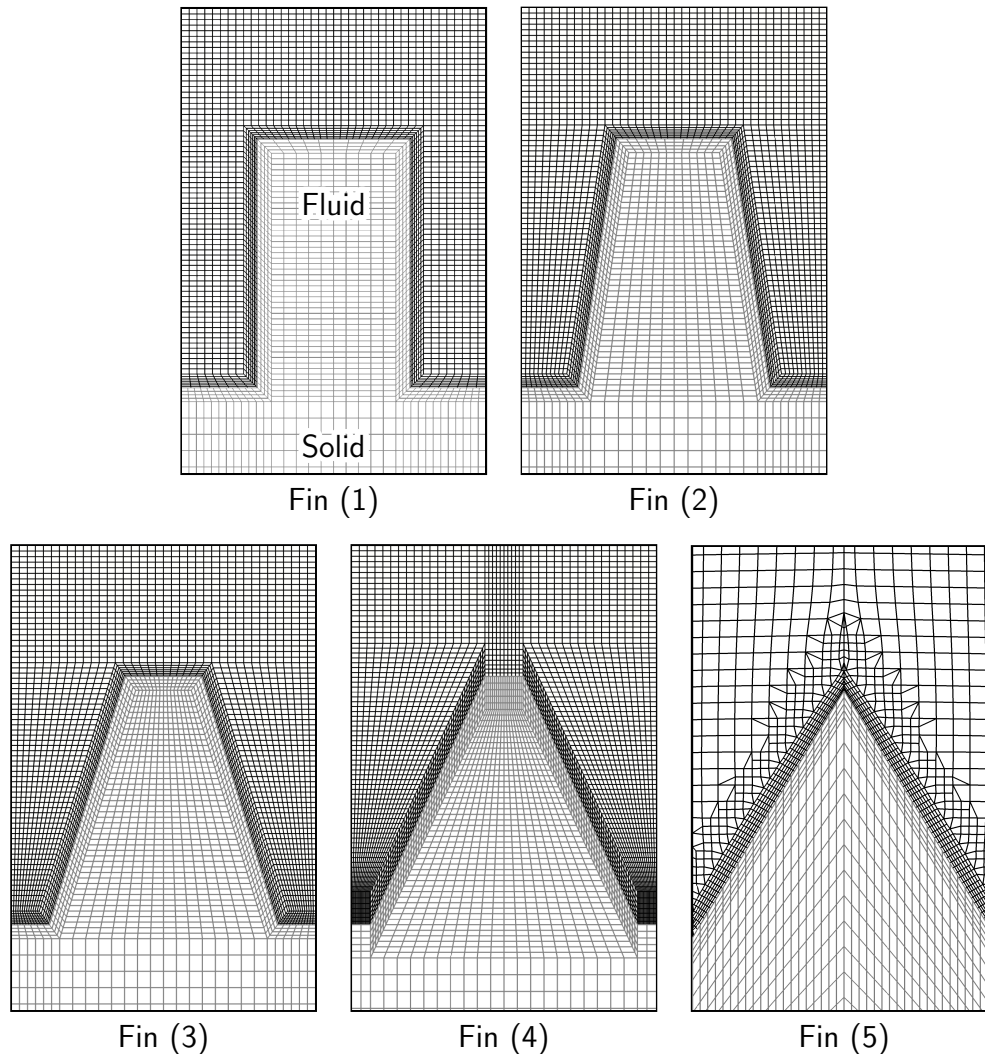


**Figure 5.7:** Part of the mesh of the solid and fluid region for fins (1) to (5).

### 5.3.2 Condensate film along the fin flank

The fluid dynamic behavior of the simulations of all fins are plausible. The simulation results regarding the film thickness  $\delta$  in the non-flooded region are regarded more closely. The following results are averaged over the periodic behavior, where condensate is dripping off.

For the first time, the film thickness on a finned tube is evaluated in the non-flooded region by the use of CFD. An evaluation method for the film thickness was developed, where the simulation domain is divided into three areas: the fin tip, the fin flank and the fin base. The thickness of the condensate film is evaluated about every  $19 \mu\text{m}$  along the fin edge using the  $\gamma$ -field. For the local determination of the film thickness, arrays perpendicular to the surface of the fin are defined with a length larger than the film thickness and an integral of the  $\gamma$ -field is solved for each array.

Figure 5.8 shows the film thicknesses along the edge length of fin (1) for five revolution angles  $0^\circ < \varphi < 90^\circ$ .

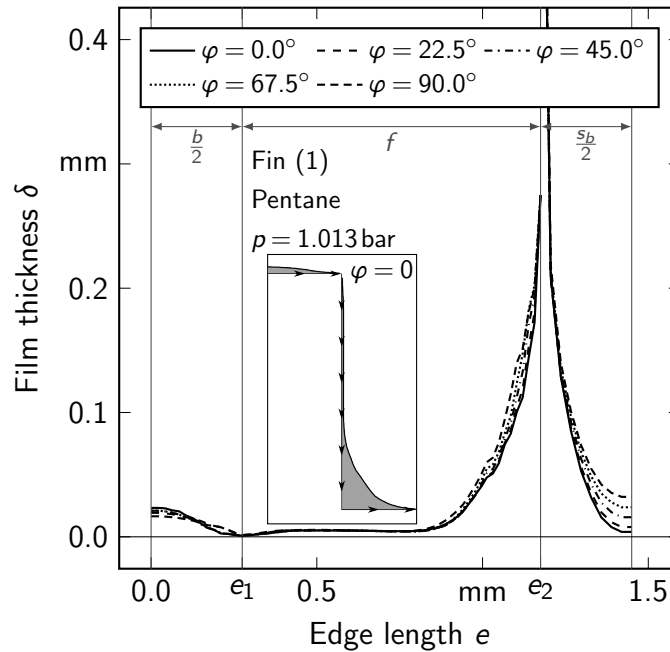


**Figure 5.8:** Film thickness along fin (1) at revolution angles  $\varphi \in [0^\circ, 90^\circ]$ .

Additionally, a schematic view of the condensate film at a revolution angle  $\varphi = 0^\circ$  is given in figure 5.8, where the direction of the fin edge is also illustrated. For  $0 < e < e_1$ , a convex condensate film is formed at the fin tip. The condensate film along the fin flank,  $e_1 < e < e_2$ , has a constant thickness for all revolution angles and only starts deviating, when the concave meniscus at the fin base starts to form due to capillary forces. Therefore, the film thickness along the fin flank is independent from  $\varphi$  for a rectangular fin. The concave meniscus at the fin base leads to an increase in film thickness at an edge length of about  $e \approx 0.8 \text{ mm}$ .

The discontinuity in film thickness at  $e = e_2$  can be attributed to the presence of a sharp edge at the fin base. The maximum film thickness along the fin flank directly at the fin base equals  $\delta = 0.255 \text{ mm} = s_b$ . At  $e = e_2$ , the evaluation array for the film thickness switches from being perpendicular to the fin flank to being perpendicular to the fin base. Thus, the evaluated film thickness gives the length of the condensate film along the fin flank, which equals  $\delta \approx 0.9 \text{ mm} = y$ . This value however is not relevant for further discussions and is therefore cut off in figure 5.8. The condensate level of the fin spacing is retrieved from the film thickness at the maximum edge length. According to figure 5.8, the condensate level of the fin spacing increases with increasing revolution angle.

The combination of a constant film thickness along the fin flank and an increasing condensate level in the fin spacing suggests that the condensate predominantly flows in radial direction from the fin tip to the fin base, where it flows in annular direction to the bottom part of the tube. This means that surface tension forces  $\mathbf{f}_\sigma$  have to be much larger than gravitational forces, as is expected for annular low-finned tubes.

The film thicknesses of all fins along the fin flank in the non-flooded region at different revolution angles  $\varphi$  are shown in figure 5.9.

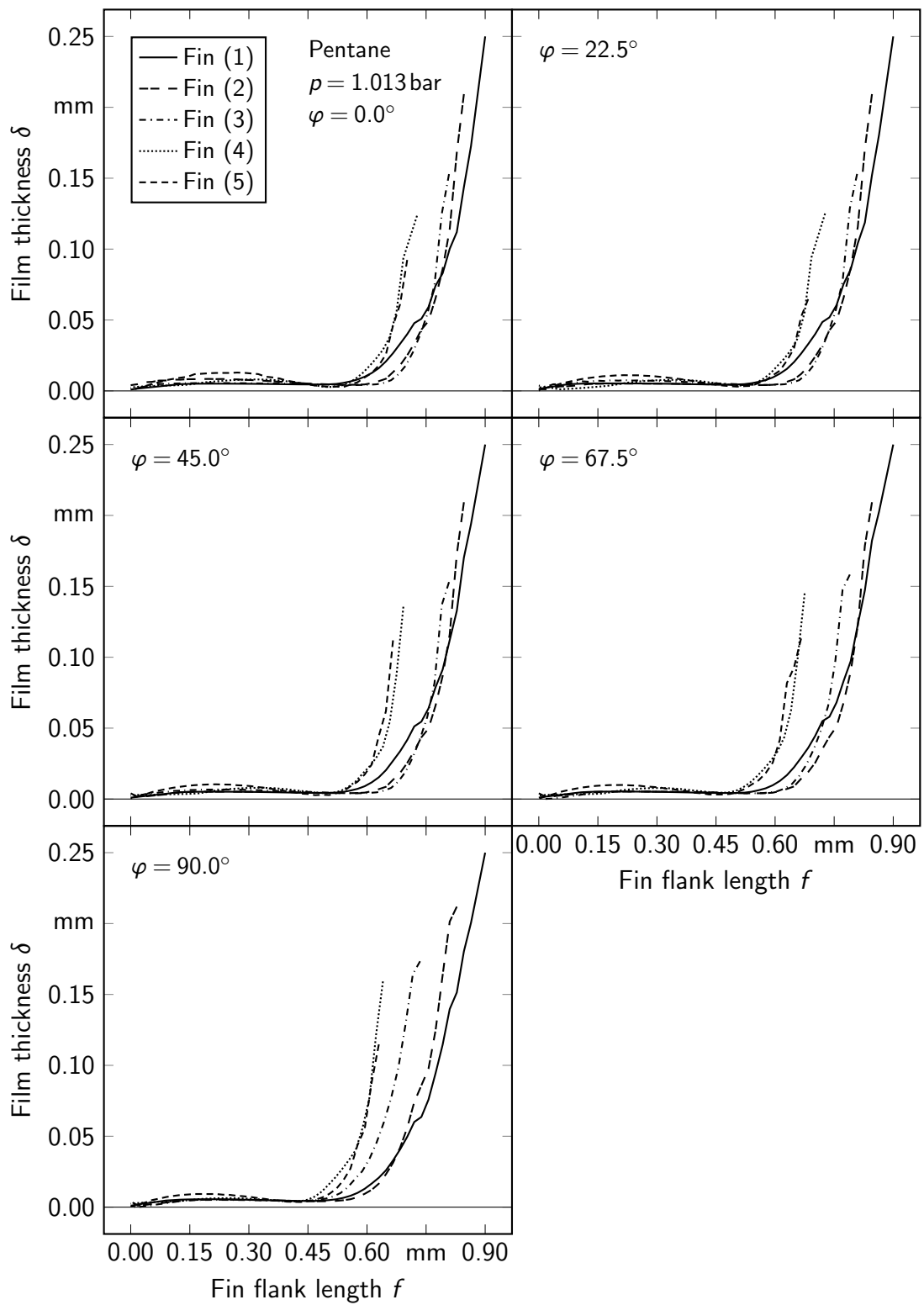


**Figure 5.9:** Film thickness of the non-flooded region of all fins at different revolution angles.

The presented trends of the film thickness end when the condensate level is reached.

The average and maximum film thicknesses  $\bar{\delta}$  and  $\delta_{\max}$ , respectively, along the fin flank above the formed menisci are given in table 5.2.

**Table 5.2:** Averaged and maximum film thicknesses along the fin flank at a revolution angle of  $\varphi = 45^\circ$ .

Fin	(1)	(2)	(3)	(4)	(5)
$\bar{\delta}$ in $\mu\text{m}$	4.29	4.31	5.29	5.22	6.84
$\delta_{\max}$ in $\mu\text{m}$	5.16	5.21	6.76	7.94	10.4

The film thickness increases with decreasing fin angle  $\beta$ . This is caused by a decrease in pressure gradient between the fin tip and the fin base with decreasing fin angle, as surface tension forces are the predominant factor.

As can be seen in figure 5.9, for low revolution angles  $\varphi < 67.5^\circ$ , the film thickness  $\delta$  is hardly influenced by the revolution angle. When comparing the different fins at a constant revolution angle, the increase in film thickness due to the formed meniscus occurs at different fin flank lengths  $f$  for each fin. This means that the different fins show different lengths of a thin condensate film which is considered the active region of the fin. For revolution angles  $\varphi < 67.5^\circ$ , this active region increases from fin (1) to fin (3) and decreases from fin (3) to fin (5). Hence, fin (3) shows the longest thin film along the fin flank in the non-flooded region and therefore has the largest active fin area in the non-flooded region. This maximum is caused on the one hand by an overall increasing maximum fin flank length from fin (1) to fin (5) and on the other hand by a combination of a change in radius of the formed menisci of the condensate and an increasing condensate level in the non-flooded region from fin (1) to fin (5). For revolution angles  $\varphi > 67.5^\circ$  a shift of the length of the active region is noticeable, which is caused by the different transition behavior of each fin from the non-flooded to the flooded region. The flooding behavior will be discussed in detail in the next section.

### 5.3.3 Flooding behavior

The flooding behavior is commonly described using the flooding angle  $\Phi$ . HONDA ET AL. 1983 developed an analytical solution for the flooding angle, which is given in equation (2.25). The flooding behavior of annular low-finned tubes changes during the periodic behavior of the condensation process, as already discussed in section 5.2. When comparing the flooding angle of the simulations with the model of HONDA ET AL. 1983, this dynamic behavior has to be considered. A meniscus at the bottom of the tube is assumed for the force equilibrium used by HONDA ET AL. 1983 for the derivation of equation (2.25). Therefore, no deformation of the interface at the bottom of the tube due to droplet formation is present. This state is present after a drip-off instance of the

periodic solution of the simulation and a minimum flooding angle during the drip-off period is reached.

The flooding angle is defined as the angle between the top of the tube and the point, where the fin space is filled with condensate [HONDA ET AL. 1983], meaning that the meniscus of the condensate reaches the fin tip. Hence, the revolution angle  $\varphi$  needs to be found, where the condensate level in the center of the fin space equals the fin height minus the inundation of the meniscus. According to HONDA ET AL. 1983, the form of the meniscus can be approximated with a constant radius. The condensate level  $l_\phi$  along the center of the fin space, at the position where the revolution angle equals the flooding angle, is thus calculated by:

$$l_\phi = y - \frac{s_t [1 - \cos(\beta)]}{2 \sin(\beta)}. \quad (5.5)$$

The flooding angle can now be evaluated for each fin at the position, where the condensate level along the center of the fin space equals  $l_\phi$ .

The comparison between the simulated flooding angles during the periodic behavior and the model of HONDA ET AL. 1983 is given in figure 5.10 for fins (1) to (5). As already mentioned, the minimum flooding angle during the periodic solution of the simulation has to be used for the comparison. Additionally, a temporal average of the simulated flooding angle across the periodic solution is given in figure 5.10.

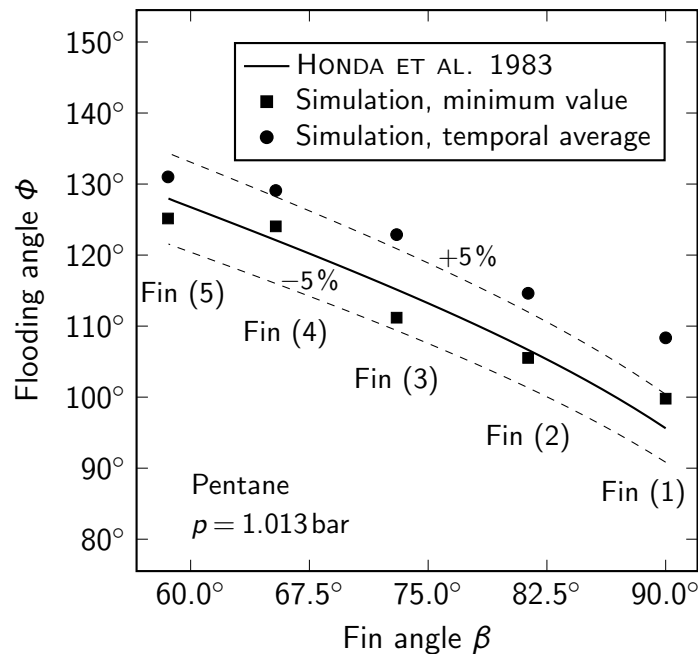


**Figure 5.10:** Change of the flooding behavior of annular low-finned tubes for the different fins.

According to figure 5.10, the flooding angle  $\Phi$  increases with decreasing fin angle  $\beta$ . Such a relation was also found by REHMAN ET AL. 2020 for the condensation on pin-fin

tubes. The deviations between the minimum flooding angles of the simulations and the model of HONDA ET AL. 1983 are below 5%. Measurements of the flooding angle from ALI 2017 on pin-fin tubes and from RUDY & WEBB 1981 on annular low-finned tubes report deviations from the analytical solution to up to 15% and 10%, respectively. Therefore, the simulation results show a fine agreement with the model of HONDA ET AL. 1983 for all fins.

The temporal average of the flooding angles of the simulations are all larger compared to the flooding angle suggested by HONDA ET AL. 1983. This can be explained by the additional gravitational force of the condensate due to the formed droplet. Therefore, using the flooding angle suggested by HONDA ET AL. 1983 for the modulation of heat transfer on annular low-finned tubes should lead to conservative results.

In the following, a single moment after a droplet dripped off is examined, when the flooding angle is at its minimum value. Figure 5.11 shows the flooding behavior along the symmetry plane of the fin spacing of fins (1) to (5) for a revolution angle of  $45^\circ < \varphi < 135^\circ$ .

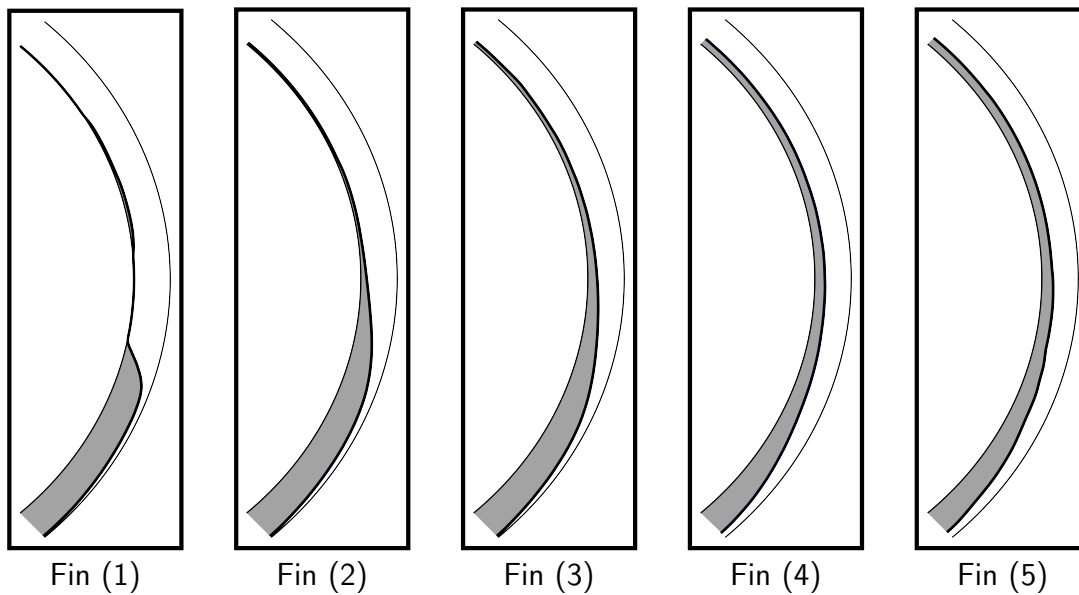


**Figure 5.11:** Change of the flooding behavior of annular low-finned tubes for the different fins.

According to figure 5.11, the condensate level in the non-flooded upper part of the tube increases with decreasing fin angle. This is caused by a decrease in cross-section of the fin spacing at the base of the fin with decreasing fin angle. Therefore, a higher condensate level is required for the condensate to flow in annular direction to the bottom of the tube.

For the rectangular fin (1), a step change in condensate level is present at the transition from the non-flooded to the flooded region. As a consequence of this, the flooding behavior can be described using a flooding angle  $\Phi$ . However, as the fin angle decreases,

the change in condensate level becomes smeared to the extent that a flooding angle  $\Phi$  does not seem to be a feasible quantity for a description of the flooding behavior.

The smearing of the transition from the non-flooded to the flooded region is due to surface tension forces. Cross sections of fin (1) and fin (3) are given in figure 5.12 along with the film thickness at revolution angles of  $\varphi = 0^\circ$  and  $\varphi = 90^\circ$ . Furthermore, a transformed film thickness labeled  $f(\varphi = 0^\circ)$  is added, which uses the results of the film thickness at  $\varphi = 0^\circ$  and shifts them in radial direction, such that its condensate level equals the condensate level at  $\varphi = 90^\circ$ .

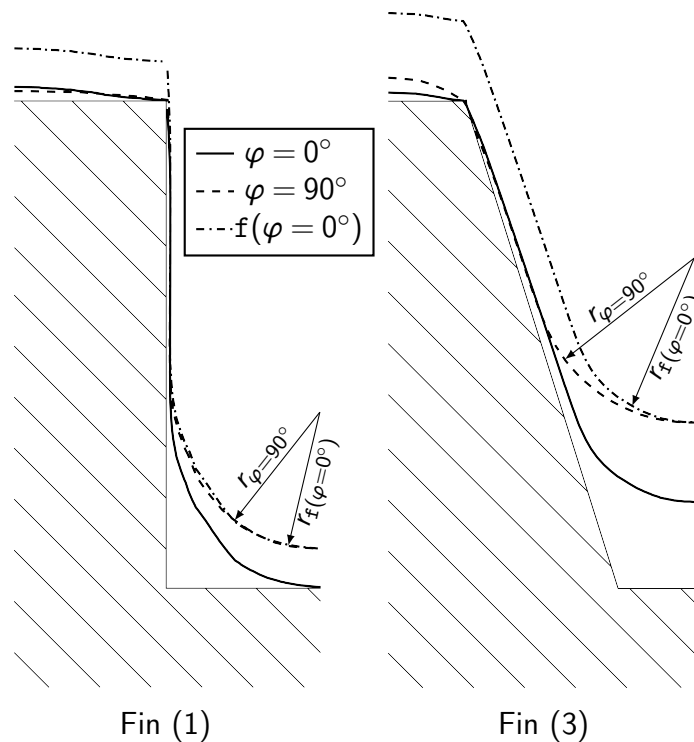


**Figure 5.12:** Change in surface tension forces with revolution angle in dependence of the fin structure.

For fin (1), the meniscus radius at a revolution angle of  $\varphi = 90^\circ$  equals the meniscus radius of the  $f(\varphi = 0^\circ)$  function. Hence, it stays the same for all revolution angles.

For fin (3), the meniscus radius increases with increasing condensate level. This leads to a decrease in surface tension forces, resulting in a decrease in pressure drop due to the concave interface. Since the condensate level rises with increasing revolution angle, a pressure gradient results in the opposite direction of the annular flow. This leads to a condensate retention, which results in a smearing of the transition from the non-flooded to the flooded region, as shown in figure 5.11.

The flooding behavior of annular low-finned tubes strongly influences heat transfer during condensation, which will be discussed in the following section.

### 5.3.4 Heat transfer

The simulations of all fins show the same progression as the GEWA-K30 tube from section 5.2. During the periodic behavior, the temperature fluctuation decreases with decreasing fin angle. This is plausible, considering the smeared transition from the non-flooded to the flooded region.

For the evaluation of heat transfer, the outer heat transfer coefficient is calculated for each fin according to section 5.2. Figure 5.13 shows the dependence of the outer heat transfer coefficient  $\alpha_o$  on the fin angle  $\beta$ .

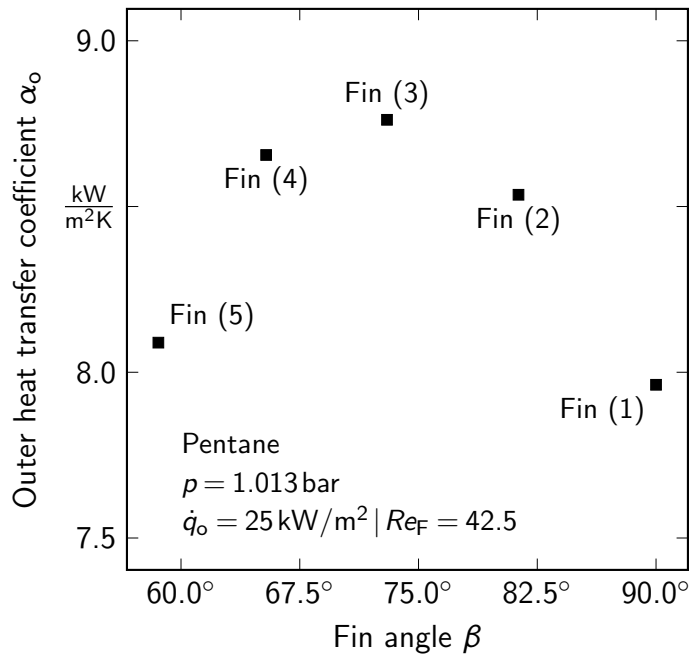


**Figure 5.13:** Dependence of the outer heat transfer coefficient on the fin angle.

The outer heat transfer coefficient initially increases with increasing fin angle from fin (1) to fin (3), which shows the highest heat transfer coefficient. Afterwards, the heat transfer coefficient decreases from fin (3) to fin (5).

A maximum heat transfer coefficient is plausible, considering the effect of the fin angle on the condensate film. As discussed in sections 5.3.2 and 5.3.3, capillary forces decrease with a decreasing fin angle. On the one hand, this decreases the overall flooding of the fin spacing, as a lower gravitational force is needed to overcome surface tension forces and form a droplet, which leads to an increase in flooding angle  $\Phi$ , which was shown in figure 5.10. On the other hand, according to table 5.2, the film thickness along the fin flank increases with decreasing fin angle. This is due to a decrease in pressure gradient from the fin base to the fin tip with increasing fin angle. Due to these opposite influences on heat transfer, an optimum fin angle should be present.

Furthermore, when comparing figure 5.13 to figure 5.9, a proportional relation between the length of the thin condensate film along the fin flank in the non-flooded region and

the heat transfer coefficient is present. A longer condensate film means that a larger active area of the fin, with a thin condensate layer, is present. This results in more efficient heat transfer.

The heat transfer coefficients  $\alpha_{\text{non-flooded}}$  and  $\alpha_{\text{flooded}}$  are evaluated according to section 5.2 for each fin. The relation between these heat transfer coefficients is  $\alpha_{\text{non-flooded}} = 3.34 \alpha_{\text{flooded}}$  for fin (1). This relation decreases with decreasing fin angle to  $\alpha_{\text{non-flooded}} = 2.15 \alpha_{\text{flooded}}$  for fin (5). The change in relation can be explained considering the change in condensate film with decreasing fin angle. On the one hand, the film thickness in the non-flooded region increases with decreasing fin angle, leading to a decrease in  $\alpha_{\text{non-flooded}}$ . On the other hand, the transition between the flooded and non-flooded region becomes smeared with increasing fin angle, which provides areas of active fin flanks at the bottom part of the tube and increases  $\alpha_{\text{flooded}}$ . Therefore, the aforementioned relation between these heat transfer coefficients decreases.

## 5.4 Conclusion

Highly resolved CFD simulations were carried out for pure substance condensation on annular low-finned tubes. Initially, the condensation of pentane outside a horizontal GEWA-K30 tube of Wieland was simulated. The resulting heat transfer coefficients lie within the accuracy of the model of REIF ET AL. 2019 and stand in excellent agreement with measurements of REIF 2016. According to the simulations, the heat transfer coefficient in the non-flooded region is about three times larger compared to the heat transfer coefficient in the flooded region.

CFD simulations were used predictively for fin geometry optimization, where the variation of the incline of the fin was focused. The simulated flooding angles for all fins stand in excellent agreement to the model of HONDA ET AL. 1983.

The influence of the incline of the fin on the resulting condensate film and heat transfer were examined. The condensate film along the fin flank increases with decreasing incline of the fin, which is attributed to a decreasing pressure gradient from the fin base to the fin tip with decreasing incline.

For a rectangular fin, a sharp transition from the non-flooded region to the flooded region was observed. This transition becomes smeared with decreasing incline of the fin. These findings suggest that the use of a flooding angle for modeling annular low-finned tubes is only applicable for rectangular fins and approaches similar to the Nusselt film theory [NUSSELT 1916a] seem more promising for a generalized modulation approach.

In the non-flooded region, the condensate level between the fins rises with a decreasing incline. This along with a change in meniscus radius with a change in fin incline leads to fin (3) having the longest thin condensate film along its fin flank. Overall, fin (3) also shows the highest heat transfer coefficient, which may be attributed to it having the largest active fin area due to it having the longest condensate film.

Overall, CFD simulations become more relevant for condensation processes, as precise predictive results can be achieved by now. Since parameter studies are not limited to manufacturing capabilities, fin geometries can be investigated, which might become accessible in the future due to innovative manufacturing techniques, as for example additive manufacturing.

## 6 Summary and Outlook

**Summary** This work focuses on the Computational Fluid Dynamics (CFD) simulation of pure substance condensation on horizontal low-finned tubes. Highly resolved CFD simulations using the Volume-of-Fluid (VOF) method are used to investigate the influence of the fin angle of annular fins upon the condensate film and heat transfer.

First, a phase change model for condensation, similar to the enthalpy method of VOLLER ET AL. 1987, was developed. This mathematical model was implemented in OpenFOAM into the multi-region framework of the *chtMultiRegionFoam* solver, which makes it possible to simulate conjugate heat transfer across solid and fluid mesh regions. The Laplace equation is solved for enthalpy transport in the solid region, while a two-phase flow with phase change is considered for the fluid region. The VOF method is used to simulate two-phase flow. This method is an interface capturing method, where the interface between vapor and condensate is resolved. Single continuity and momentum equations are solved for a mixture phase. Volume averaged properties within a control volume are calculated for this mixture phase. An additional transport equation for the phase fraction is solved and no interface reconstruction is used. A sharp phase-boundary is achieved by using the Multidimensional Universal Limiter for Explicit Solution (MULES) algorithm of OpenFOAM for the translation of the phase fraction. An enthalpy equation is solved for heat transfer. Phase change is considered by source terms in the transport equations of the fluid region. The phase change model determines a volumetric phase change rate, which is evaluated iteratively from the temperature field. The iteration is needed, since the volumetric phase change rate leads to a source term in the temperature field, due to heat release or withdrawal during condensation or boiling, respectively. Thus, the enthalpy equation and the volumetric phase change rate are solved within this iteration cycle, as they are co-dependent of each other. The source terms of the other transport equations are evaluated after the volumetric phase change rate is determined.

The implemented CFD solver in OpenFOAM is initially validated using the Stefan problem [KLEINER ET AL. 2019]. The Stefan problem is a 1D validation case, where, for condensation, a vapor phase at saturation conditions rests above a sub-cooled wall. Heat is then withdrawn from the vapor to the wall. This leads to the formation of a condensate film. Due to the continuous withdrawal of heat, the condensate film becomes sub-cooled and additional condensate is formed at the condensate-vapor interface. The condensate film also rests on the sub-cooled wall. Hence, heat is transferred via conduction. With the assumption of a constant wall temperature, an analytical solution for the film thickness in dependence of time and temperature difference between the wall

and vapor is available. The simulation results of the Stefan problem stand in excellent agreement with the analytical solution for pentane and water as condensing media.

Afterwards, simulations of pentane condensing on the outside of horizontal tubes are carried out [KLEINER ET AL. 2019]. NUSSELT 1916a describes the condensation on horizontal smooth tubes in his film theory, where he considers a horizontal tube with a constant temperature at the outer surface. The tube is surrounded by a static vapor phase at saturation conditions. He determines the film thickness in annular direction of the tube and derives a relation for the average outer heat transfer coefficient. NUSSELT 1916a neglects surface tension and ends up with a continuous falling film for a 2D case. In order to compare the simulation accuracy with Nusselt's film theory, 2D simulations are carried out for smooth tubes, where the run-off behavior of the condensate is initially enforced for film Reynolds numbers  $Re_F \leq 103$ . The resulting condensate film thicknesses stand in excellent agreement with Nusselt's film theory. Slight deviations are gained at the bottom of the tube, which are attributed to the simulations considering surface tension. These slight deviations lead to slightly smaller heat transfer coefficients in the simulation compared to the theory. Afterwards, run-off behavior is not enforced in further 2D simulations. This leads to a periodic solution where condensate is dripping off at the bottom of the tube (drip-off behavior). Due to the droplet accumulation, a slight decrease in heat transfer coefficients is observed compared to the results of the run-off simulations. 3D simulations of condensation on smooth tubes are also carried out for a most critical wave length of the thin film Rayleigh-Taylor instability for film Reynolds numbers between  $33.5 \leq Re_F \leq 40.8$ . A constant heat flux is withdrawn from the inside of the tubes. The fluid dynamic behavior of the two-phase flow is physically correct and the outer heat transfer coefficients of the simulations lie between the outer heat transfer coefficients of the 2D run-off and drip-off simulations. This shows that it is not necessary to cover an entire Rayleigh-Taylor instability within the simulation domain as the droplet inundation does not need to be considered during simulations for accurate results. This is considered to hold true for low-finned tubes as well, making the investigation using highly resolved two-phase CFD simulations possible, as the simulation domain length only needs to cover a single fin.

Initially, CFD simulations are carried out for a GEWA-K30 tube from Wieland for film Reynolds numbers between  $34.0 \leq Re_F \leq 51.0$  [KLEINER ET AL. 2020]. The simulation domain covers half a fin and half a fin spacing. A constant heat flux is withdrawn from the inside of the tube. The fluid dynamic behavior of the formed condensate film is physically plausible and the resulting heat transfer coefficients stand in excellent agreement with measurements of REIF 2016. The resulting heat transfer coefficient in the non-flooded region is about three times larger as compared to the flooded region of the tube. The influence of the fin angle upon the condensate film and the resulting heat transfer coefficient is investigated for a film Reynolds number  $Re_F = 42.5$  [KLEINER ET AL. 2020]. Five fin geometries with differing fin angles were examined, which transition from a rectangular fin to a triangular fin. The film thickness along the fin flank in the non-flooded region were evaluated for different revolution angles. The film thickness increases with decreasing fin angle. It was also deduced from these results

that condensate flows in radial direction from the fin tip to the fin base and runs off in annular direction inside the fin spacing at the bottom of the fin in the non-flooded region. Flooding angles were evaluated from the simulation results according to the definition of HONDA ET AL. 1983. These flooding angles stand in excellent agreement to the model of HONDA ET AL. 1983. Furthermore, the flooding behavior changes with changing fin angle. For a rectangular fin, a clear transition between the non-flooded and flooded region is visible and a flooding angle may be defined. With decreasing fin angle, this transition becomes smeared to the point that no clear transition is visible. As the fill height of the fin spacing changes with the revolution angle for slanted fins, the smeared transition is attributed to a change in meniscus radius with changing revolution angle. A combination of the meniscus radius and the fill height of the fin spacing for the different fins leads to fins with a mediocre fin angle having the longest thin condensate film along the fin flank in the non-flooded region. This also leads to these fins having the highest heat transfer coefficient.

**Outlook** Highly resolved CFD simulations allow for detailed investigations of pure substance condensation on custom geometries. The insights gained from such simulations make a structured approach for geometry optimization possible. While a combination of different models may be used to predict property influences upon the condensation process on surface structured tubes, they are not able to predict the efficiency of new geometries of the surface structure. This is considered the key advantage of the developed CFD algorithm. Since it does not rely on calibration and provides very accurate results, it is well suited for predictive use, especially when screening for new geometries of the surface structure. This advantage is especially promising, when considering the advances in innovative additive manufacturing techniques, e. g. 3D printing. Overall, CFD has proven to be a very useful tool for the investigation of phase change phenomena and will play an important role for future developments.

From this point forward, it is possible to branch out in different directions, with the developed CFD code. The presented solver shows outstanding results within this work. However, the phase change algorithm still relies on small time steps, as the simulations are mostly bound by the Fourier number. One possibility to increase the time step size, therefore, would be to further increase the stability of the coupled behavior between the phase fraction and enthalpy. This could be achieved by adapting the presented iteration loop with an explicit phase fraction update to an implicit implementation of the change in phase fraction, similar to the melting model of FADEN ET AL. 2018. In addition, the presented phase change model would also work with phase reconstruction approaches. A very promising phase reconstruction approach solver called isoAdvector is released in the new OpenFOAM version. A combination of the developed phase change algorithm and the VOF implementation of the isoAdvector solver could further improve the simulation quality, i. e. simulation speed and stability.

A detailed description of pure substance condensation is very useful to understand the fluid dynamic behavior during condensation. Since a multi-component mixture is often present during condensation, further development of the algorithm towards

phase change of mixtures is suggested. According to BÜCHNER 2016, slight impurities in an otherwise pure substance may lead to a drastic decrease in heat transfer during condensation. Especially, if the impurity is an inert component. This decrease occurs due to an additional resistance caused by mass transfer in the vapor phase. This leads to a complex interplay between heat and mass transfer, which is very difficult to include in modeling approaches. CFD may very well prove itself to be the method of choice for this task. RIEKS & KENIG 2018 developed a rigorous simulation approach for condensation of binary mixtures, where the highly coupled behavior of heat and mass transfer is solved iteratively. Their simulation approach shows promising results for a simple 1D test case. An extension of the developed solver of this thesis towards condensation of mixtures similar to the approach of RIEKS & KENIG 2018 is considered a possible and promising approach.

# List of Tables

3.1	General modeling approaches for two-phase flows [ACHER 2015]. . . . .	43
4.1	Properties of water and pentane for saturation conditions for $p = 1.013$ bar [LINSTROM & MALLARD n.d., VDI 2013]. . . . .	68
5.1	Varying dimensions of fins (1) to (5). . . . .	94
5.2	Averaged and maximum film thicknesses along the fin flank at a revolution angle of $\varphi = 45^\circ$ . . . . .	98

# List of Figures

2.1	Example setup for heat transfer across a single tube [REIF 2016]. . . . .	6
2.2	Temperature profile during heat transfer through a tube in radial direction for steady state [KLEINER 2014]. . . . .	6
2.3	Specific enthalpy in dependence of temperature. . . . .	10
2.4	Formed condensate on a subcooled wall during film and droplet condensation [BERGMAN ET AL. 2011]. . . . .	11
2.5	Surface tension forces acting on the phase boundaries. . . . .	12
2.6	Interface deformation of the Rayleigh–Taylor instability [PALACIO MONTES 2018]. . . . .	13
2.7	Different condensate flow patterns during condensate strip-off. . . . .	15
2.8	Condensate film according to Nusselt’s film theory [NUSSELT 1916a]. . . . .	16
2.9	Temperature profile in radial direction during condensation on the outside of a tube for steady state [KLEINER 2014]. . . . .	18
2.10	Isometric view of an annular low-finned tube [REIF 2016]. . . . .	19
2.11	Cross section of the fin structure of annular low-finned tubes. . . . .	19
2.12	Formed condensate film during condensation on the outside of annular low-finned tubes [KLEINER 2014]. . . . .	20
3.1	Arbitrary control volume [MARSCHALL 2011]. . . . .	25
3.2	Transition from a continuous to a discretized flow domain. . . . .	29
3.3	Depiction of a considered control volume. . . . .	30
3.4	Non-Orthogonality correction [JASAK 1996]. . . . .	33
3.5	Definitions for boundary CV treatment. . . . .	35
3.6	Algorithms for pressure-velocity coupling. . . . .	42
3.7	Phase indication of the VOF method. . . . .	46
3.8	Phase indication of the VOF method with and without phase reconstruction. . . . .	49
3.9	Considered 1D case for the description of the MULES algorithm. . . . .	51
3.10	Schematic for the determination of the weighing factors in the MULES algorithm. . . . .	53
4.1	Iteration scheme for the evaluation of the energy balance source term $S_q$ . . . . .	66
4.2	Stefan problem 1D simulation domain for a mesh resolution of 50 cells. . . . .	67
4.3	Simulated results and analytical solution of the Stefan problem. . . . .	69
4.4	Simulation domain for 2D horizontal tube condensation cases. . . . .	70
4.5	Simulation progression with condensate run-off behavior for a temperature difference of 50 K. . . . .	71
4.6	Simulation results of the 2D run-off simulations. . . . .	72

---

4.7	Temperature, phase fraction and specific heat release profiles at a revolution angle of $45^\circ$ . . . . .	73
4.8	Temperature, phase fraction and specific heat release profiles at a revolution angle of $90^\circ$ . . . . .	74
4.9	Temperature, phase fraction and specific heat release profiles at a revolution angle of $135^\circ$ . . . . .	75
4.10	Interface location of condensate - Comparison between simulation and Nusselt's film theory. . . . .	76
4.11	Outer tube wall heat flux over time for the run-off and drip-off simulations with a temperature difference of 10 K. . . . .	77
4.12	Simulation results of the 2D drip-off and run-off simulations. . . . .	78
4.13	Simulation domain for 3D horizontal tube condensation cases. . . . .	79
4.14	Drip-off progression of the 3D horizontal tube condensation simulation. . . . .	81
4.15	Comparison of outer heat transfer coefficients between the measurements of REIF 2016, Nusselt's film theory and the different simulation approaches. . . . .	82
5.1	Comparison between the fin cross-section [REIF ET AL. 2015] of a GEWA-K30 tube and the CAD model . . . . .	86
5.2	Simulation domain for condensation on horizontal low-finned tubes. . . . .	87
5.3	Simulation progression of pure substance condensation on a horizontal GEWA-K30 tube. . . . .	89
5.4	Change in average inner wall temperature of the tube over the simulated time for pure substance condensation on a horizontal GEWA-K30 tube. . . . .	90
5.5	Change of the outer heat transfer coefficient for different targeted withdrawn heat fluxes for the condensation of pentane on a GEWA-K30 tube. . . . .	92
5.6	Examined fin geometries with different fin angles $\beta$ . . . . .	93
5.7	Part of the mesh of the solid and fluid region for fins (1) to (5). . . . .	95
5.8	Film thickness along fin (1) at revolution angles $\varphi \in [0^\circ, 90^\circ]$ . . . . .	96
5.9	Film thickness of the non-flooded region of all fins at different revolution angles. . . . .	97
5.10	Change of the flooding behavior of annular low-finned tubes for the different fins. . . . .	99
5.11	Change of the flooding behavior of annular low-finned tubes for the different fins. . . . .	100
5.12	Change in surface tension forces with revolution angle in dependence of the fin structure. . . . .	101
5.13	Dependence of the outer heat transfer coefficient on the fin angle. . . . .	102

# List of Publications

Kleiner, T.; Rehfeldt, S.; Klein, H.: *CFD model and simulation of pure substance condensation on horizontal tubes using the volume of fluid method*. International Journal of Heat and Mass Transfer 138 (2019) 420-431. DOI: [10.1016/j.ijheatmasstransfer.2019.04.054](https://doi.org/10.1016/j.ijheatmasstransfer.2019.04.054).

Kleiner, T.; Gottanka, M.; Stary, A.; Rehfeldt, S.; Bertakis, E.; Klein, H.: *CFD-Simulation einer generischen Reaktion in einem gerührten Behälter*. Chemie Ingenieur Technik 92.8 (2020) 1065-1073. DOI: [10.1002/cite.201900188](https://doi.org/10.1002/cite.201900188).

Kleiner, T.; Eder, A.; Rehfeldt, S.; Klein, H.: *Detailed CFD simulations of pure substance condensation on horizontal annular low finned tubes including a parameter study of the fin slope*. International Journal of Heat and Mass Transfer 163 (2020) 120363. DOI: [10.1016/j.ijheatmasstransfer.2020.120363](https://doi.org/10.1016/j.ijheatmasstransfer.2020.120363).

Losher, T.; Kleiner, T.; Hill, S.; Sarajlic, N.; Rehfeldt, S.; Klein, H.: *Comparison of the Generalized Species Transfer Model with a Two-Field Approach for Interfacial Mass Transfer*. Chemical Engineering & Technology 43.12 (2020) 2576-2582. DOI: [10.1002/ceat.202000259](https://doi.org/10.1002/ceat.202000259).

# Bibliography

ACHER 2015

ACHER, T.: *A Moments Model for the Numerical Simulation of Bubble Column Flows*. PhD thesis. Technical University of Munich, 2015.

ADHIKARI & RATTNER 2018

ADHIKARI, S. ; RATTNER, A. S.: *Heat transfer during condensing droplet coalescence*. International Journal of Heat and Mass Transfer 127 (2018) 1159–1169. DOI: [10.1016/j.ijheatmasstransfer.2018.07.005](https://doi.org/10.1016/j.ijheatmasstransfer.2018.07.005).

ALI 2017

ALI, H. M.: *An analytical model for prediction of condensate flooding on horizontal pin-fin tubes*. International Journal of Heat and Mass Transfer 106 (2017) 1120–1124. DOI: [10.1016/j.ijheatmasstransfer.2016.10.088](https://doi.org/10.1016/j.ijheatmasstransfer.2016.10.088).

BADILLO 2012

BADILLO, A.: *Quantitative phase-field modeling for boiling phenomena*. Physical Review E 86.4 (2012). DOI: [10.1103/PhysRevE.86.041603](https://doi.org/10.1103/PhysRevE.86.041603).

BAER & STEPHAN 2011

BAER, H. D. ; STEPHAN, K.: *Heat and Mass Transfer*. Springer, 2011. ISBN: 978-3-642-20021-2. DOI: [10.1007/978-3-642-20021-2](https://doi.org/10.1007/978-3-642-20021-2).

BEATTY & KATZ 1948

BEATTY, K. ; KATZ, D. L.: *Condensation of vapors on outside of finned tubes*. Chemical Engineering Progress 44 (1948) 55–70.

BERBEROVIĆ 2009

BERBEROVIĆ, E.: *Drop impact onto a liquid layer of finite thickness: Dynamics of the cavity evolution*. Physical Review E 79 (2009). DOI: [10.1103/PhysRevE.79.036306](https://doi.org/10.1103/PhysRevE.79.036306).

BERGMAN ET AL. 2011

BERGMAN, T. ; LAVINE, A. ; INCROPERA, F. ; DEWITT, D.: *Fundamentals of Heat and Mass Transfer*. Ed. by L. RATTS. John Wiley and Sons, 2011. ISBN: 978-0470-50197-9.

BIRD ET AL. 2007

BIRD, R. B. ; STEWART, W. E. ; LIGHTFOOT, E. N.: *Transport Phenomena*. Ed. by W. ANDERSON. rev. 2. ed. John Wiley & Sons, Inc., 2007. ISBN: 0470115394.

BORIS & BOOK 1973

BORIS, J. P. ; BOOK, D. L.: *Flux-corrected transport. I. SHASTA, a fluid transport algorithm that works*. Journal of Computational Physics (1973). DOI: [10.1016/0021-9991\(73\)90147-2](https://doi.org/10.1016/0021-9991(73)90147-2).

BRACKBILL ET AL. 1992

BRACKBILL, J. ; KOTHE, D. B. ; ZEMACH, C.: *A continuum method for modeling surface tension*. Journal of Computational Physics 100.2 (1992) 335–354. DOI: [10.1016/0021-9991\(92\)90240-Y](https://doi.org/10.1016/0021-9991(92)90240-Y).

BRIGGS & ROSE 1995

BRIGGS, A. ; ROSE, J. W.: *Condensation performance of some commercial integral fin tubes with steam and CFC113*. Experimental Heat Transfer 8 (1995) 131–143. DOI: [10.1080/08916159508946496](https://doi.org/10.1080/08916159508946496).

BRIGGS & ROSE 1994

BRIGGS, A. ; ROSE, J.: *Effect of fin efficiency on a model for condensation heat transfer on a horizontal, integral-fin tube*. International Journal of Heat and Mass Transfer 37 (1994) 457–463. DOI: [10.1016/0017-9310\(94\)90045-0](https://doi.org/10.1016/0017-9310(94)90045-0).

BÜCHNER 2016

BÜCHNER, A.: *Kondensation binärer Gemische an horizontalen Rohren*. PhD thesis. Technical University of Munich, 2016.

BÜCHNER ET AL. 2015

BÜCHNER, A. ; REIF, A. ; REHFELDT, S. ; KLEIN, H.: *Problematik einheitlicher Betrachtungen des Wärmedurchgangs bei der Kondensation an strukturierten Rohren*. Chemie Ingenieur Technik 87.3 (2015) 301–305. DOI: [10.1002/cite.201400050](https://doi.org/10.1002/cite.201400050).

CZESLIK ET AL. 2010

CZESLIK, C. ; SEEMANN, H. ; WINTER, R.: *Basiswissen Physikalische Chemie*. Springer, 2010. ISBN: 978-3-8348-0937-7.

DE SCHEPPER ET AL. 2009

DE SCHEPPER, S. ; HEYNDERICKX, G. J. ; MARIN, G. B.: *Modeling the evaporation of a hydrocarbon feedstock in the convection section of a steam cracker*. Computers & Chemical Engineering 33.1 (2009) 122–132. DOI: [10.1016/j.compchemeng.2008.07.013](https://doi.org/10.1016/j.compchemeng.2008.07.013).

EUROPEAN COMMISSION 2020

EUROPEAN COMMISSION: *State of the Union: Commission raises climate ambition and proposes 55% cut in emissions by 2030*. 2020. URL: [https://ec.europa.eu/commission/presscorner/detail/en/IP\\_20\\_1599](https://ec.europa.eu/commission/presscorner/detail/en/IP_20_1599).

FADEN ET AL. 2018

FADEN, M.; KÖNIG-HAAGEN, A.; HÖHLEIN, S.; BRÜGGEMANN, D.: *An implicit algorithm for melting and settling of phase change material inside macrocapsules*. International Journal of Heat and Mass Transfer 117 (2018) 757–767. DOI: [10.1016/j.ijheatmasstransfer.2017.10.033](https://doi.org/10.1016/j.ijheatmasstransfer.2017.10.033).

FANG ET AL. 2010

FANG, C.; DAVID, M.; ROGACS, A.; GOODSON, K.: *Volume of fluid simulation of boiling two-phase flow in a vapor-venting microchannel*. Frontiers in Heat and Mass Transfer 1 (2010) 013002. DOI: [10.5098/hmt.v1.1.3002](https://doi.org/10.5098/hmt.v1.1.3002).

FERZIGER & PERIĆ 2002

FERZIGER, J. H.; PERIĆ, M.: *Computational Methods for Fluid Dynamics*. 3rd. Springer, 2002. ISBN: 3-540-42074-6.

GANAPATHY ET AL. 2013

GANAPATHY, H.; SHOOSHTARI, A.; CHOO, K.; DESSIATOUN, S.; ALSHEHHI, M.; OHADI, M.: *Volume of fluid-based numerical modeling of condensation heat transfer and fluid flow characteristics in microchannels*. International Journal of Heat and Mass Transfer 65 (2013) 62–72. DOI: [10.1016/j.ijheatmasstransfer.2013.05.044](https://doi.org/10.1016/j.ijheatmasstransfer.2013.05.044).

GEBAUER ET AL. 2013

GEBAUER, T.; AL-BADRI, A. R.; GOTTERBARM, A.; HAJAL, J. E.; LEIPERTZ, A.; FRÖBA, A. P.: *Condensation heat transfer on single horizontal smooth and finned tubes and tube bundles for R134a and propane*. International Journal of Heat and Mass Transfer 56.1 (2013) 516–524. DOI: [10.1016/j.ijheatmasstransfer.2012.09.049](https://doi.org/10.1016/j.ijheatmasstransfer.2012.09.049).

GINZBURG & WITTUM 2001

GINZBURG, I.; WITTUM, G.: *Two-Phase Flows on Interface Refined Grids Modeled with VOF, Staggered Finite Volumes, and Spline Interpolants*. Journal of Computational Physics 166.2 (2001) 302–335. DOI: <https://doi.org/10.1006/jcph.2000.6655>.

GISTEMP TEAM 2021

GISTEMP TEAM: *GISS Surface Temperature Analysis (GISTEMP), version 4*. NASA Goddard Institute for Space Studies. Jan. 2021. URL: [data.giss.nasa.gov/gistemp/](https://data.giss.nasa.gov/gistemp/).

GREGORIG 1973

GREGORIG, R.: *Wärmetausch und Wärmeaustauscher: Konstruktionssystematik, Serienproduktion, Rohrschwingungen, fertigungsgerechte wirtschaftliche Optimierung aufgrund von Exergieverlusten*. Sauerländer AG, Aarau, 1973.

HABLA 2014

HABLA, F.: *Modeling and CFD simulation of viscoelastic single and multiphase flows*. PhD thesis. Technische Universität München, 2014.

HARDT & WONDRA 2008

HARDT, S.; WONDRA, F.: *Evaporation model for interfacial flows based on a continuum-field representation of the source terms*. Journal of Computational Physics 227.11 (2008) 5871–5895. DOI: [10.1016/j.jcp.2008.02.020](https://doi.org/10.1016/j.jcp.2008.02.020).

HIRT & NICHOLS 1981

HIRT, C.; NICHOLS, B.: *Volume of fluid (VOF) method for the dynamics of free boundaries*. Journal of Computational Physics 39.1 (1981) 201–225. DOI: [10.1016/0021-9991\(81\)90145-5](https://doi.org/10.1016/0021-9991(81)90145-5).

HOLZMANN 2017

HOLZMANN, T.: *Mathematics, Numerics, Derivations and OpenFOAM®*. Ed. by T. HOLZMANN. 7th ed. Tobias Holzmann, 2017. URL: [https://www.researchgate.net/publication/307546712\\_Mathematics\\_Numerics\\_Derivations\\_and\\_OpenFOAMR](https://www.researchgate.net/publication/307546712_Mathematics_Numerics_Derivations_and_OpenFOAMR).

HONDA & NOZU 1987

HONDA, H.; NOZU, S.: *A Prediction Method for Heat Transfer During Film Condensation on Horizontal Low Integral-Fin Tubes*. Journal of Heat Transfer 2.1 (1987) 218–225. DOI: [10.1115/1.3248046](https://doi.org/10.1115/1.3248046).

HONDA ET AL. 1983

HONDA, H.; NOZU, S.; MITSUMORI, K.: *Augmentation of condensation on horizontal finned tubes by attaching a porous drainage plate*. Transactions of the Japan Society of Mechanical Engineers Series B 49.445 (1983) 1937–1945. DOI: [10.1299/kikaib.49.1937](https://doi.org/10.1299/kikaib.49.1937).

HONDA ET AL. 1987

HONDA, H.; NOZU, S.; TAKEDA, Y.: *Flow characteristics of condensate on a vertical column of horizontal low finned tubes*. ASME-JSME Thermal Engineering Joint Conference 1 (1987) 517–524.

HONDA ET AL. 1991

HONDA, H.; UCHIMA, B.; NOZU, S.; NAKATA, H.; TORIGOE, E.: *Film Condensation of R-113 on In-Line Bundles of Horizontal Finned Tubes*. Journal of Heat Transfer 5.1 (1991) 479–486. DOI: [10.1115/1.2910586](https://doi.org/10.1115/1.2910586).

IPCC 2013

IPCC: Annex III: Glossary. *Climate Change 2013: The Physical Science Basis. Contribution of Working Group I to the Fifth Assessment Report of the Intergovernmental Panel on Climate Change*. Ed. by S. PLANTON. Cambridge University Press, 2013.

## IPCC 2018

IPCC: *Summary for Policymakers. In: Global Warming of 1.5 °C. An IPCC Special Report on the impacts of global warming of 1.5 °C above pre-industrial levels and related global greenhouse gas emission pathways, in the context of strengthening the global response to the threat of climate change, sustainable development, and efforts to eradicate poverty.* World Meteorological Organization, Geneva, Switzerland. 2018.

## ISSA 1986

ISSA, R.: *Solution of the Implicit Discretized Fluid Flow Equations by Operator Splitting.* Journal of Computational Physics 62 (1986) 40–65. DOI: [10.1016/0021-9991\(86\)90099-9](https://doi.org/10.1016/0021-9991(86)90099-9).

## JASAK 1996

JASAK, H.: *Error Analysis and Estimation for the Finite Volume Method with Applications to Fluid Flows.* PhD thesis. Imperial College, 1996.

## JI ET AL. 2019

JI, W.-T.; MAO, S.-F.; CHONG, G.-H.; ZHAO, C.-Y.; ZHANG, H.; TAO, W.-Q.: *Numerical and experimental investigation on the condensing heat transfer of R134a outside plain and integral-fin tubes.* Applied Thermal Engineering 159 (2019) 113878.

## KATZ ET AL. 1974

KATZ, D. L.; HOPE, R. E.; DATSKO, S. C.: *Liquid retention on finned tubes.* Department of Engineering Research, University of Michigan (1974).

## KHARANGATE ET AL. 2015

KHARANGATE, C. R.; LEE, H.; MUDAWAR, I.: *Computational modeling of turbulent evaporating falling films.* International Journal of Heat and Mass Transfer 81 (2015) 52–62. DOI: [10.1016/j.ijheatmasstransfer.2014.09.068](https://doi.org/10.1016/j.ijheatmasstransfer.2014.09.068).

## KHARANGATE &amp; MUDAWAR 2017

KHARANGATE, C. R.; MUDAWAR, I.: *Review of computational studies on boiling and condensation.* International Journal of Heat and Mass Transfer 108 (2017) 1164–1196. DOI: [10.1016/j.ijheatmasstransfer.2016.12.065](https://doi.org/10.1016/j.ijheatmasstransfer.2016.12.065).

## KLEIN &amp; BÜCHNER 2018

KLEIN, H.; BÜCHNER, A.: *Low-Finned Tubes for Condensation. Innovative Heat Exchangers.* Ed. by H.-J. BART; S. SCHOLL. Springer, 2018. Chap. Low-Finned Tubes for Condensation 189–231. ISBN: 978-3-319-71639-8.

## KLEINER 2014

KLEINER, T.: *Bestimmung des äußeren Wärmeübergangskoeffizienten bei der Kondensation von Gemischen an einem Rippenrohrbündel.* Master's Thesis. Technical University of Munich, 2014.

KLEINER 2019

KLEINER, T.: *tpcMultiRegionFOAM*. 2019. URL: <https://github.com/ThomasKleiner/tpcMultiRegionFoam>.

KLEINER ET AL. 2020

KLEINER, T.; EDER, A.; REHFELDT, S.; KLEIN, H.: *Detailed CFD simulations of pure substance condensation on horizontal annular low finned tubes including a parameter study of the fin slope*. International Journal of Heat and Mass Transfer 163 (2020) 120363. DOI: [10.1016/j.ijheatmasstransfer.2020.120363](https://doi.org/10.1016/j.ijheatmasstransfer.2020.120363).

KLEINER ET AL. 2019

KLEINER, T.; REHFELDT, S.; KLEIN, H.: *CFD model and simulation of pure substance condensation on horizontal tubes using the volume of fluid method*. International Journal of Heat and Mass Transfer 138 (2019) 420–431. DOI: [10.1016/j.ijheatmasstransfer.2019.04.054](https://doi.org/10.1016/j.ijheatmasstransfer.2019.04.054).

KUMAR ET AL. 1998

KUMAR, R.; VARMA, H.; MOHANTY, B.; AGRAWAL, K.: *Augmentation of outside tube heat transfer coefficient during condensation of steam over horizontal copper tubes*. International Communications in Heat and Mass Transfer 25.1 (1998) 81–91. DOI: [10.1016/S0735-1933\(97\)00139-5](https://doi.org/10.1016/S0735-1933(97)00139-5).

KUMAR ET AL. 2002

KUMAR, R.; VARMA, H.; MOHANTY, B.; AGRAWAL, K.: *Prediction of heat transfer coefficient during condensation of water and R-134a on single horizontal integral-fin tubes*. International Journal of Refrigeration 25.1 (2002) 111–126. DOI: [10.1016/S0140-7007\(00\)00094-3](https://doi.org/10.1016/S0140-7007(00)00094-3).

KUNKELMANN & STEPHAN 2009

KUNKELMANN, C.; STEPHAN, P.: *CFD Simulation of Boiling Flows Using the Volume-of-Fluid Method within OpenFOAM*. Numerical Heat Transfer, Part A: Applications 56.8 (2009) 631–646.

LAFaurIE ET AL. 1994

LAFaurIE, B.; NARDONE, C.; SCARDOVELLI, R.; ZALESKI, S.; ZANETTI, G.: *Modelling Merging and Fragmentation in Multiphase Flows with SURFER*, Journal of Computational Physics, 113.1 (1994) 134–147. DOI: [10.1006/jcph.1994.1123](https://doi.org/10.1006/jcph.1994.1123).

LAPLACE 1805

LAPLACE, P. S.: *Traité de Mécanique Céleste. 4*. De l'Imprimerie De Crapelet, 1805.

LEE 1980

LEE, W.: *A Pressure Iteration Scheme for Two-Phase Flow Modeling*. Multiphase Transport Fundamentals, Reactor Safety, Applications 1 (1980) 407–431.

LENSEN ET AL. 2019

LENSEN, N. ; SCHMIDT, G. ; HANSEN, J. ; MENNE, M. ; PERSIN, A. ; RUEDY, R. ; ZYSS, D.: *Improvements in the GISTEMP uncertainty model*. J. Geophys. Res. Atmos. 124.12 (2019) 6307–6326. DOI: [10.1029/2018JD029522](https://doi.org/10.1029/2018JD029522).

LEWIS 1950

LEWIS: *The instability of liquid surfaces when accelerated in a direction perpendicular to their plane, II*. Proceedings, Royal Society of London 202 (1950) 81.

LINSTROM & MALLARD n.d.

LINSTROM, P. ; MALLARD, W.: *NIST Chemistry WebBook, NIST Standard Reference Database Number 69*. National Institute of Standards and Technology. DOI: [10.18434/T4D303](https://doi.org/10.18434/T4D303).

MARIĆ ET AL. 2014

MARIĆ, T. ; HÖPKEN, J. ; MOONEY, K.: *The OpenFOAM® Technology Primer*. sourceflux UG, 2014. ISBN: 978-3-00-046757-8.

MÁRQUEZ 2013

MÁRQUEZ, S.: *An Extended Mixture Model for the Simultaneous Treatment of Short and Long Scale Interfaces*. PhD thesis. Universidad Nacional Del Litoral, 2013.

MARSCHALL 2011

MARSCHALL, H.: *Towards the Numerical Simulation of Multi-Scale Two-Phase Flows*. PhD thesis. Technische Universität München, 2011.

MILNE-THOMSON 1960

MILNE-THOMSON: *Theoretical Hydrodynamics*. The macmillan company of canada limited, 1960. ISBN: 978-0486689708.

MITROVIĆ 1986

MITROVIĆ, J.: *Influence of Tube Spacing and Flow Rate on Heat Transfer from a Horizontal Tube to a Falling Liquid Film*. Proceedings of International Journal of Heat and Mass Transfer. 1986 1949–1956. DOI: [10.1615/IHTC8.1700](https://doi.org/10.1615/IHTC8.1700).

MUZAFERIJA ET AL. 1998

MUZAFERIJA, S. ; PERIC, M. ; SAMES, P. ; SCHELLIN, T.: *A Two-Fluid Navier-Stokes Solver to Simulate Water Entry*. Naval hydrodynamics. 1998 638–651.

NICHITA & THOME 2010

NICHITA, B. ; THOME, J.: *A level set method and a heat transfer model implemented into FLUENT for modeling of microscale two phase flows*. AVT-178 Specialists' Meeting on System Level Thermal Management for Enhanced Platform Efficiency. 2010.

NOH & WOODWARD 1976

NOH, W. F. ; WOODWARD, P.: *SLIC (Simple Line Interface Calculation)*. Proceedings of the Fifth International Conference on Numerical Methods in Fluid Dynamics. Ed. by A. I. van de VOOREN ; P. J. ZANDBERGEN. Berlin, Heidelberg: Springer Berlin Heidelberg, 1976 330–340. ISBN: 978-3-540-37548-7.

NUSSELT 1916a

NUSSELT, W.: *Die Oberflächenkondensation des Wasserdampfes*. Zeitschrift des Vereines Deutscher Ingenieure 60.27 (1916) 569–575.

NUSSELT 1916b

NUSSELT, W.: *Die Oberflächenkondensation des Wasserdampfes*. Zeitschrift des Vereines Deutscher Ingenieure 60.27 (1916) 541–546.

OPENFOAM 2021

OPENFOAM. The OpenFOAM Foundation. The OpenFOAM Foundation, 2021. URL: <https://openfoam.org/version/4-1/>.

PALACIO MONTES 2018

PALACIO MONTES, A.: *Development of a CFD-Solver for Film Boiling of Pure Substances*. Master's Thesis. Technical University of Munich, 2018.

PATANKAR 1980

PATANKAR, S. V.: *Numerical Heat Transfer and Fluid Flow*. Hemisphere Publishing Corporation, 1980. ISBN: 978-981-13-1903-7.

POLIFKE & KOPITZ 2009

POLIFKE, W. ; KOPITZ, J.: *Wärmeübertragung: Grundlagen, analytische und numerische Methoden*. 2nd ed. Pearson Studium, 2009. ISBN: 9783827371041.

PRICE 2000

PRICE, G. R.: *A Piecewise Parabolic Volume Tracking Method for the Numerical Simulation of Interfacial Flows*. PhD thesis. The University of Calgary, 2000.

RATTNER & GARIMELLA 2014

RATTNER, A. S. ; GARIMELLA, S.: *Simple Mechanistically Consistent Formulation for Volume-of-Fluid Based Computations of Condensing Flows*. Journal of Heat Transfer 136.7 (2014). DOI: [10.1115/1.4026808](https://doi.org/10.1115/1.4026808).

RATTNER & GARIMELLA 2018

RATTNER, A. S. ; GARIMELLA, S.: *Simulation of Taylor flow evaporation for bubble-pump applications*. International Journal of Heat and Mass Transfer 116 (2018) 231–247. DOI: [10.1016/j.ijheatmasstransfer.2017.08.110](https://doi.org/10.1016/j.ijheatmasstransfer.2017.08.110).

RAYLEIGH 1883

RAYLEIGH, J. W. S.: *Investigation of the character of the equilibrium of an incompressible heavy fluid of variable density*. Proceedings of the London Mathematical Society 14 (1883) 170–177. DOI: [10.1112/plms/s1-14.1.170](https://doi.org/10.1112/plms/s1-14.1.170).

REHMAN ET AL. 2020

REHMAN, H. U. ; ALI, H. M. ; AHMAD, S. ; BALUCH, M. A.: *Experimental investigation of condensate retention on horizontal pin fin tube with varying pin angle*. Case Studies in Thermal Engineering 17 (2020) 100549. DOI: [10.1016/j.csite.2019.100549](https://doi.org/10.1016/j.csite.2019.100549).

REIF 2016

REIF, A.: *Kondensation von Reinstoffen an horizontalen Rohren*. PhD thesis. Technische Universität München, 2016.

REIF ET AL. 2015

REIF, A. ; BÜCHNER, A. ; REHFELDT, S. ; KLEIN, H.: *Äußerer Wärmeübergangskoeffizient bei der Kondensation von Reinstoffen an einem horizontalen Rippenrohr*. Chemie Ingenieur Technik 87.3 (2015) 260–269. DOI: [10.1002/cite.201400044](https://doi.org/10.1002/cite.201400044).

REIF ET AL. 2019

REIF, A. ; BÜCHNER, A. ; REHFELDT, S. ; KLEIN, H.: *Outer heat transfer coefficient for condensation of pure components on single horizontal low-finned tubes*. Heat and Mass Transfer 55 (Nov. 2019) 3–16. DOI: [10.1007/s00231-017-2184-3](https://doi.org/10.1007/s00231-017-2184-3).

RIEKS & KENIG 2018

RIEKS, S. ; KENIG, E. Y.: *Modelling and numerical simulation of coupled transport phenomena with phase change: Layer evaporation of a binary mixture*. Chemical Engineering Science 176 (2018) 367–376. DOI: [10.1016/j.ces.2017.10.040](https://doi.org/10.1016/j.ces.2017.10.040).

ROENBY ET AL. 2016

ROENBY, J. ; BREDMOSE, H. ; JASAK, H.: *A computational method for sharp interface advection*. Royal Society Open Science 3.11 (2016) 160405. DOI: [10.1098/rsos.160405](https://doi.org/10.1098/rsos.160405).

ROSE 1994

ROSE, J.: *An approximate equation for the vapour-side heat-transfer coefficient for condensation on low-finned tubes*. International Journal of Heat and Mass Transfer 37.5 (1994) 865–875. DOI: [10.1016/0017-9310\(94\)90122-8](https://doi.org/10.1016/0017-9310(94)90122-8).

RUDY & WEBB 1983a

RUDY, T. ; WEBB, R.: *Theoretical model for condensation on horizontal, integral-fin tubes*. Heat Transfer Conference AIChE Symp. Ser. 79, New York, 1983.

RUDY & WEBB 1981

RUDY, T. M. ; WEBB, R. L.: *Condensate retention on horizontal integral-fin tubing, advances in Enhanced Heat Transfer*. 20th National Heat Transfer Conference ASME HTD-18. 1981 35–41.

RUDY & WEBB 1983b

RUDY, T. ; WEBB, R.: *Theoretical model for condensation of horizontal integral-fin tubes*. AIChE symposium series 225 79 (1983) 11–18.

SAMKHANIANI & ANSARI 2016

SAMKHANIANI, N. ; ANSARI, M.: *Numerical simulation of bubble condensation using CF-VOF*. Progress in Nuclear Energy 89 (2016) 120–131. DOI: [10.1016/j.pnucene.2016.02.004](https://doi.org/10.1016/j.pnucene.2016.02.004).

SCHRAGE 1953

SCHRAGE, R.: *A Theoretical Study of Interphase Mass Transfer*. Columbia University Press, New York, 1953. ISBN: 978-0-231-90162-8.

SHEN ET AL. 2017

SHEN, Q. ; SUN, D. ; SU, S. ; ZHANG, N. ; JIN, T.: *Development of heat and mass transfer model for condensation*. International Communications in Heat and Mass Transfer 84 (2017) 35–40. DOI: [10.1016/j.icheatmasstransfer.2017.03.009](https://doi.org/10.1016/j.icheatmasstransfer.2017.03.009).

SON & DHIR 1998

SON, G. ; DHIR, V. K.: *Numerical Simulation of Film Boiling Near Critical Pressures With a Level Set Method*. Journal of Heat Transfer 120.1 (1998) 183–192. DOI: [10.1115/1.2830042](https://doi.org/10.1115/1.2830042).

SUSSMAN ET AL. 1994

SUSSMAN, M. ; SMEREKA, P. ; OSHER, S.: *A Level Set Approach for Computing Solutions to Incompressible Two-Phase Flow*. Journal of Computational Physics 114.1 (1994) 146–159. DOI: [10.1006/jcph.1994.1155](https://doi.org/10.1006/jcph.1994.1155).

SZIJÁRTÓ 2015

SZIJÁRTÓ, R.: *Condensation of steam in horizontal pipes - model development and validation*. PhD thesis. ETH-Zürich, 2015.

SZIJÁRTÓ ET AL. 2017

SZIJÁRTÓ, R. ; BADILLO, A. ; NIČENO, B. ; PRASSER, H.-M.: *Condensation models for the water-steam interface and the volume of fluid method*. International Journal of Multiphase Flow 93 (2017) 63–70. DOI: [10.1016/j.ijmultiphaseflow.2017.04.002](https://doi.org/10.1016/j.ijmultiphaseflow.2017.04.002).

TABOREK 1974

TABOREK, J.: Design methods for heat transfer equipment: a critical survey of the state of the art. *Heat Exchangers: Design and Theory Source Book*. McGraw-Hill, 1974.

TANASAWA 1991

TANASAWA, I.: Advances in condensation heat transfer. *Advances in Heat Transfer*. 21. Academic Press, San Diego, 1991 55–139.

TANNEHILL ET AL. 1997

TANNEHILL, J. ; ANGERSON, D. ; PLETCHER, R.: *Computational Fluid Mechanics and Heat Transfer*. Ed. by W. J. MINKOWYCZ ; E. M. SPARROW. Hemisphere Publishing Corporation, 1997.

TAYLOR 1950

TAYLOR, G.: *The instability of liquid surfaces when accelerated in a direction perpendicular to their planes*. Proceedings of the Royal Society of London. Series A, Mathematical and Physical Sciences 201.1065 (1950) 192–196.

TORNBERG 2000

TORNBERG, A.-K.: *Interface Tracking Methods with Application to Multiphase Flows*. PhD thesis. Royal Institute of Technology, 2000.

UBBINK & ISSA 1999

UBBINK, O. ; ISSA, R.: *A Method for Capturing Sharp Fluid Interfaces on Arbitrary Meshes*. Journal of Computational Physics 153.1 (1999) 26–50. DOI: [10.1006/jcph.1999.6276](https://doi.org/10.1006/jcph.1999.6276).

UNVERDI & TRYGGVASON 1992

UNVERDI, S. ; TRYGGVASON, G.: *A front-tracking method for viscous, incompressible, multi-fluid flows*. Journal of Computational Physics 100.1 (1992) 25–37. DOI: [10.1016/0021-9991\(92\)90307-K](https://doi.org/10.1016/0021-9991(92)90307-K).

VDI 2013

VDI: *VDI-Wärmeatlas*. Ed. by 11. Springer Berlin Heidelberg, 2013. ISBN: 978-3-540-25503-1.

VOLLER ET AL. 1987

VOLLER, V. R. ; CROSS, M. ; MARKATOS, N. C.: *An enthalpy method for convection/diffusion phase change*. International Journal for Numerical Methods in Engineering 24.1 (1987) 271–284. DOI: [10.1002/nme.1620240119](https://doi.org/10.1002/nme.1620240119).

WANG ET AL. 2007

WANG, H. ; GARIMELLA, S. V. ; MURTHY, J. Y.: *Characteristics of an evaporating thin film in a microchannel*. International Journal of Heat and Mass Transfer 50.19 (2007) 3933–3942. DOI: [10.1016/j.ijheatmasstransfer.2007.01.052](https://doi.org/10.1016/j.ijheatmasstransfer.2007.01.052).

WEBB ET AL. 1985

WEBB, R. L. ; RUDY, T. M. ; KEDZIERSKI, M. A.: *Prediction of the Condensation Coefficient on Horizontal Integral-Fin Tubes*. Journal of Heat Transfer 107.2 (1985) 369–376. DOI: [10.1115/1.3247424](https://doi.org/10.1115/1.3247424).

WELCH & WILSON 2000

WELCH, S. W. ; WILSON, J.: *A Volume of Fluid Based Method for Fluid Flows with Phase Change*. Journal of Computational Physics 160 (2000) 662–682. DOI: [10.1006/jcph.2000.6481](https://doi.org/10.1006/jcph.2000.6481).

WELLER 2002

WELLER, H.: *Derivation modelling and solution of the conditionally averaged two-phase flow equations*. Nabla Ltd. Technical Report TR/HGW/02, United Kingdom (2002).

YOUNG ET AL. 1980

YOUNG, D. ; LORENZ, J. ; GANIC, E.: *Vapor/Liquid Interaction and Entrainment in Falling Film Evaporators*. Transactions of the ASME 102 (1980) 20–25.

YOUNG 1982

YOUNG, D.: Time-Dependent Multi-material Flow with Large Fluid Distortion. *Numerical Methods in Fluid Dynamics*. Ed. by K. W. MORTON ; M. J. BAINES. Academic Press, 1982. Chap. Time-Dependent Multi-material Flow with Large Fluid Distortion 273–285.

YOUNG 1805

YOUNG, T.: *III. An essay on the cohesion of fluids*. Philosophical Transactions of the Royal Society of London 95 (1805) 65–87. DOI: [10.1098/rstl.1805.0005](https://doi.org/10.1098/rstl.1805.0005).

ZALESAK 1979

ZALESAK, S. T.: *Fully multidimensional flux-corrected transport algorithms for fluids*. Journal of Computational Physics 31.3 (1979) 335–362. DOI: [10.1016/0021-9991\(79\)90051-2](https://doi.org/10.1016/0021-9991(79)90051-2).